In presenting this thesis in partial fulfillment of the requirements for an advanced degree at Idaho State University, I agree that the Library shall make it freely available for inspection. I further state that permission to download and/or print my thesis for scholarly purposes may be granted by the Dean of the Graduate School, Dean of my academic division, or by the University Librarian. It is understood that any copying or publication of this thesis for financial gain shall not be allowed without my written permission.

Signature ______________________________

Date __________________________________

Resistance and Resistivity Measurements of Exploding Aluminum Wires

A Thesis presented

by

Andrew Hoffman

to

The Department of Physics

in partial fulfillment of the requirements

for the degree of

Masters of Science

in the subject of

Physics

Idaho State University

May 2016

To the Graduate Faculty:

The members of the committee appointed to examine the thesis of Andrew Hoffman find it satisfactory and recommend that it be accepted.

Dr. Khalid Chouffani,
Major Advisor

Dr. George Imel,
Committee Member

Dr. Chad Pope,
Graduate Faculty Representative

To Tony Wayne who inspired me to pursue a career in physics through his inspiring and fun methods of teaching. To Carla Hunt who taught me what it meant to truly care about her students, and who showed me I could excel in mathematically difficult fields. To Dr. Lawrence Reese who patiently advised and taught me what I needed to know to survive in graduate school. To Dr. Bart Czirr and John Ellsworth for their help in teaching me critical research skills. Most especially to my parents who have always supported my love and curiosity of the world around me.

Acknowledgments

Very special thanks to Dr. Khalid Chouffani for his support, patience, advice, and help on this project. Without him I would truly not have accomplished my Master's work. Special thanks to Dr. George Imel and Dr. Chad Pope for their work and support as members of this committee. Thanks to Dr. Rick Spielman for his involvement, support, and input on this project. Thanks to my fellow graduate students (you know who you are) who have helped me in my classes and my research. Thanks to all my professors who have helped me gain the knowledge required to succeed in the field.

Contents

List of Figures

Thesis advisor
Dr. Khalid Chouffani

Author
Andrew Hoffman

Resistance and Resistivity Measurements of Exploding Aluminum Wires

Abstract

We have conducted a series of experiments to measure the resistance and resistivity of 125 micron exploding aluminum wires 2.3 cm in length. The wires were insulated using glass capillaries 0.1 mm thick with an outer diameter of 1 mm. Two series of wires were exploded, one with a charging voltage of 2.3 kV and the other at 7 kV. Additionally we used an ICCD camera with a 50 ns gate to take images and measure the radius of the wire as it exploded. Our results found that at 2.3 kV the wire does not have a significant expansion and no current pause is observed. Additionally the resistance of the wires discharged at 2.3 kV peak at around 1 Ω. At 7 kV a current pause was observed, and the wire expands significantly at the beginning of the current pause. At 7 kV the resistance peaks at around 20 Ω. Resistivity measurements are included.

Chapter 1

Introduction

1.1 History of Exploding Wires Research

The exploding wire phenomenon (EWP) or exploding wire method (EWM) has been an area of research since the late 1700s. The first documented case of inciting the EWP was by an English mathematician and scientist Edward Nairne in 1773. Nairne used 64 Leyden jars for his machine and was able to observe the EWP using a thin iron wire. He described the wire as it exploded saying, "it flew about the room in innumerable red hot balls." [1] It is also interesting to note that Nairne attempted this same experiment on various forms of plant and animal life as well. In 1784 Martin van Marum melted 70 feet of metal wire using 64 Leyden jars. This did not, however, actual produce the EWP though it did contribute to further work in the field [2, 3]. In the 1850s Michael Faraday experimented with thin film deposition using exploding gold films [4]. While these and a few other experiments generated interest in the phenomenon, development of exploding wires research did not occur until the early to mid 20th century.

The 1920s saw mostly spectrographic work due to new photographic techniques including rotating mirror cameras. Work included the postulation of transmutation into helium from tungsten wires [5] which was later disproved [6]. Throughout the 1920s and the 1930s theories developed as to the actual mechanism of the exploding wire. Kleen suggested that sausage instabilities caused the striations of the vapor in the wire [7], which is still an accepted mechanism in the field for the causation of current pause.

The mid 1900s saw the advancement in the field of high speed photography in large part due to WWII. High speed shutters and high speed framing cameras were developed, as well as Kerr-Cell photography which has been widely used in the field. Several investigations suggested current flow disruption due to shockwaves and the metal melting into ellipsoid particles which expand and vaporize. Lochte-Holtgreven attempted in the early 1950s to more precisely classify the mechanism into phases that are typically accepted today: ohmic heating and change of phase, current pause or "dwell time", restrike, and final oscillating discharge. In the early 1960s, the work of Bennett saw two distinct explosions, one with and one without the current pause depending on the variables [8]. Continued work using streak cameras and Kerr-Cell photography helped to gain a better understanding on the actual mechanisms, and the variables which affect the mechanism including charging voltage, current rise time, wire material, and wire dimensions. For a more in depth history of exploding wire research up until the early 1960s, one can read "Exploding Wire Research 1774-1963" published by the Naval Research Lab [9].

More recent developments in the 90s till the present have focused primarily on achieving higher densities for the use of confinement fusion [10]. The research focus has shifted towards larger z-pinch arrays or x-pinch arrays at much higher voltages with newer advances in gas switches and capacitor arrays allowing for much faster and higher current rise times. This includes some work being done at Idaho State University on a smaller more modular X-pinch [11].

Continued work in the field of lower voltage, single wire exploding wire research is still being conducted with the advantages of newer technologies. These include the use of x-ray backlighters [12], laser interferometery [13], high speed spectrometry, and (included in this work) the development of high speed photography through Intensified CCD arrays.

1.2 Applications

1.2.1 Warm Dense Matter

Warm dense matter consists of a regime of high enough temperature/density for matter to be partially ionized and have strongly coupled ions. While warm dense matter does have strong coupling effects, they do not behave collectively, and cannot be stringently classified as a plasma. They are encountered in nature most typically in planetary cores (such as Jupiter [14]) or cool stars such as brown dwarfs [15]. Experimentally they can be created through inertial confinement or laser heating [16–18]. Because it does not exhibit the behavior of either a dense gas or a plasma, it is difficult to theoretically predict the behavior of matter in such a state solely relying on one model. This has caused warm dense matter to become an area of interest especially with expanding laser, x-ray, and solid state technologies which enable us to study this state of matter.

1.2.2 Inertial Confinement Fusion

Inertial confinement fusion is of great interest to many due to its potential of energy production. There are three primary approaches being researched which are laser confinement [19], Tokamak magnetic confinement [20], and z-pinch confinement [21]. While pinches are the only exploding wire confinement process, the information gained from lower energy exploding wire experiments adds information about material properties that is useful for the development and benchmarking of codes developed for all experiments in this regime of matter.

1.2.3 Thin Films and Nanomaterials

Nanoparticles have become of interest due to their wide variety of applications. Thin films are especially useful for their unique behavior in semiconducting applications as well as optical coatings. The production of such materials (especially in high purity) is difficult to achieve and expensive. Exploding wires produce extremely pure samples of nanoparticles due to the condensation of the plasma-vapor which can be done on a material or in water [22–24].

1.2.4 Detonators

Exploding Bridgewater Detonators were first developed for the application of nuclear weapons due to their ability to detonate simultaneously. Because of the high temperature produced, exploding wires can be used to detonate secondary charges such as PETN (plastic explosives) [25]. Beyond military applications, exploding wire detonators have found a variety of uses in the civilian world.

1.3 Theory

1.3.1 Exploding Wire Mechanism

The exploding wire mechanism in most literature is described as having three phases: ohmic heating of the wire, a current pause or "dwell time", and finally a "restrike" which causes current to flow again. The mechanism is highly dependent on the wire material, length, diameter, and applied voltage. At lower applied voltages the wire is usually allowed to ionize before the rapid vaporization causes the wire to form an insulator. This allows the system to fully discharge without a current pause, and therefore lacking the need for a restrike mechanism. While most studies have been conducted for higher charging voltages, the research conducted by this study focuses primarily on lower charging voltages.

Ohmic Heating

When the voltage is initially applied across the wire, the resistance in the wire causes heating and eventually a phase change into a liquid, and then a vapor/gas state. Towards the end of the ohmic heating stage is when ionization occurs and a plasma begins to develop, but because it is in a warm dense matter state it is difficult to determine exactly when the transition occurs between a vapor and a plasma state.

A number of studies have been conducted in order to determine where the phase transitions start in the wire, and consequently how they occur. Because of the inconsistencies of the conclusions found in earlier papers, Antonios Vlastos conducted a series of experiments in the late 1960s and early 1970s to study the initial phase transitions, the current pause, and the restrike mechanisms of exploding wires and how the applied voltage, wire material, and wire diameter affects each. In his studies he found that an increase in diameter corresponds to slower rise times and smaller current peaks. Similarly a decrease in applied voltage also corresponded to slower rise times and smaller current peaks [26]. It should be noted that with almost all exploding wires, the initial ohmic heating mechanism is the same, but the end of the ohmic heating stage affects the rest of the mechanism.

Current Pause

The current pause or "dwell time" is caused by a rapid vaporization of the wire. As the wire vapor expands, it forms an insulator and prevents current from flowing. This current pause only occurs when the expansion of the wire is fast enough to cause an insulating effect before any ion channels can develop. Therefore below a certain critical voltage or energy deposition rate the current pause does not occur as observed by Bennett [8]. This critical voltage is dependent on wire length, material, diameter, and system inductance.

In the work done by Vlastos in atmospheric conditions, two primary types of explosions occurred: one in which ion channels developed on the surface of the wire, and another in which the ion channels developed in the interior of the wire during the dwell time. His observations were that these dwell times were a function of the field gradient along the wire, but suggested that newer insights might be gained through changing the pressure by adding a material or medium surrounding the wire [27]. Experiments conducted in both water and plastic insulator have shown to have different dwell time effects even at higher voltages [28] [29]. This suggests that the dwell time is very much affected by pressure which keeps the plasma intact and prevents the rapid expansion which causes the current pause.

Without containment, most of the wire expansion occurs during this dwell time due to the loss of magnetic pressure in the system.

Restrike

The restrike mechanism, like the dwell time, largely depends on the initial voltage applied. At lower voltages, an ionization is allowed to occur on the outside surface of the wire. This ionization increases as energy is deposited into the system, and forms the current channel for the restrike in the system.

At higher voltages the wire vaporization occurs rapidly, and prevents the surface of the wire from creating an ionization channel due to the violent expansion. It is also of note that the channels typically form a helical shape, which is most likely caused by the ion channels being developed across the E cross B field lines [30].

1.3.2 Instabilities

The instabilities which occur in the exploding wire are one the primary causes of any inconsistencies between discharges. The primary instabilities that are found in exploding wires are the screw, kink, and sausage or flute instabilities.

The two instabilities which form first within the wire are the sausage and kink instabilities. The kink instability forms when there is a kink or bend in the wire causing the magnetic pressure on the concave side of the bend to increase, and on the convex side to decrease. While the internal electric field will attempt to fix the instability back to equilibrium, at lower voltages this may cause a faster disintegration of the wire. This is likely to occur in exploding wires due to the imperfection and difficulty of creating a perfectly straight wire.

The sausage of flute instability arises from an imperfection in the radius of the wire or plasma column where the radius is smaller in some areas. Because of the smaller radius, the radial magnetic field gradient is much larger in this region causing a much higher magnetic pressure. In the wire this leads to hot spots developing, and it has been theorized that this is what leads to the actual current pause [31]. While the current pause mechanism is much more complex depending on many parameters, the sausage instability could lead in some experiments to a current pause. It does affect the reproducibility of each experiment as wires without imperfections are impossible to create, and these instabilities play a role in the unsymmetrical disintegration of the wire. When using some sort of containment such as a capillary, surrounding liquid, or insulator the effects of these instabilities can be minimized.

The screw instability is a helical instability which forms only at certain voltages. Vlastos observed that this helical instability occurs during the dwell time. He concludes that this instability may have two causes. One may be a force-free field existing during the dwell time which would force the charged ions and electrons along the helical path due to the E cross B fields created, as the current and voltage do not reach a complete zero during this dwell time. It may also be due to the twisting effect while placing the wire. Vlastos observed that he was able to reverse the helicity by winding the wire in the opposite direction [32].

1.3.3 ICCD

An ICCD (intensified CCD) intensifier is composed of four primary components: a photocathode, a microchannel plate (MCP) in an applied voltage field, a phosphor, and the optics which guide the light into the CCD. Each ICCD can have a variety of parameters depending on the phosphor used, and the voltage applied across the microchannel plate.

Intensifier Mechanism

An external lens is usually attached to the camera nose, or an array of lenses is used to focus the light onto the intensifier tube. An input window captures the image and directs the photons towards the photocathode. As the photons hit the photocathode they excite electrons which are then accelerated through the applied electric field. After leaving the photocathode the accelerated electrons then hit the MCP which is an array of channels made of glass tubes on the order of a few microns in diameter, and about a millimeter long.The channel walls are coated with a resistive material. When the primary electrons are accelerated through the MCP, they interact with the channel walls and excite secondary electrons creating a cascade in the same manner as a photomultiplier tube. When higher voltages are applied, the electron multiplication increases through the MCP. After being accelerated and multiplied, the electrons travel towards a phosphor. The phosphor is either attached to a fiber optic window to output the light directly onto the CCD, or in the case of a lens coupled ICCD a lens is used on the back side of the intensifier. The lens configuration allows the CCD to be used as a standalone if desired.

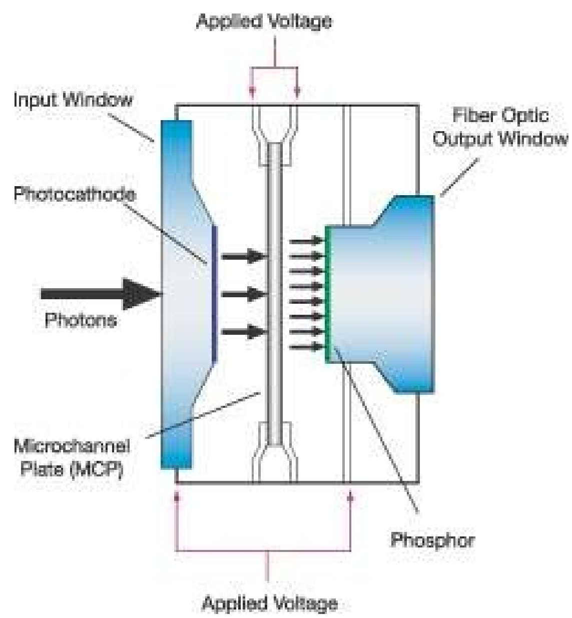

Figure 1.1: Diagram of ICCD intensifier mechanism. *Andor Learning.* [33]

Gating and Voltage

The gating for the camera is not controlled by a physical shutter like a traditional camera, but rather is controlled by the voltage applied across the intensifier. While gated off the voltage applied is a negative bias which does not allow for any electrons to pass through. When gated on the voltage applied becomes a positive bias which allows for the electrons to flow through the field and microchannel plate. This means that for fast gating applications a special power supply must be used in order to increase the voltage across the intensifier in a short amount of time. The amount of voltage applied is adjustable to change the gain, increasing the light sensitivity of the camera. ICCDs are designed to be sensitive to single photons when high voltage is applied.

Phosphor and Photocathode

The quantum efficiency, and minimum gate width of the ICCD are determined by the phosphor and photocathode properties. Gen II and Gen III intensifiers are both in use currently, and provide unique advantages for specific applications. Gen I intensifiers used multi-alkali coatings, and were initially developed to be used as night vision optics for the military. They have since been mostly abandoned due to their risk of burnout, higher noise levels, and limited wavelength performance range.

Gen II intensifiers used the same alkali coatings as the Gen I intensifiers, but were significantly thicker as well as introduced the use of a MCP. The military was able to use coatings that reduced the sensitivity in the blue and increase sensitivity in the red/NIR region for low light optics uses. For scientific applications, photocathodes have been developed for the high blue/green spectrum. The two most common photocathodes used are the S20 and the S25, although the S20 can be designed for high blue or low red spectra.

The phosphor used in the camera plays an important role in determining the frame rate possible for the intensifier (the CCD will also have it's own determined frame rate). This is because the phosphor must have time to decay onto the CCD before the next frame can be recorded, otherwise the phosphor will still have leftover excitation from the previous image. The common standard phosphor of ICCDs is the P43 due to its high quantum efficiency. The P43, however, suffers from a long decay time. Two popular fast decay phosphors used in ICCDs are the P46 and P47. While both have considerably short %90-%10 decay times the P47 phosphor has been shown in some studies to have a faster initial decay which gives it the advantage of having the capability of higher frame rates. Both phosphors have an initial decay to %10 in the range of 200 ns or less for short exposure times [34]. Because of their high cost most studies on phosphor decay times have been conducted by primarily ICCD manufacturers, and more studies should be conducted.

Chapter 2

Experiment

2.1 Capacitive Discharge System

Figure 2.1: Control Console and trigger models (left) and pneumatic switch to discharge capacitor after explosion (right)

The wire explosion is driven by a 2.6 μF, 40 kV maximum charging voltage capacitor. Two sets of data were taken charging the capacitor to 2.3 kV and 7 kV using a commercial high-voltage power supply through a 250 kΩ high power resistor. The discharge mechanism is initiated by sending a TTL trigger from a pulse generator into a pulse/delay generator which delivers a 300 V fast short pulse to a custom high voltage trigger generator designed and built by Dr. Chouffani. The custom high voltage trigger generator (figures 2.2 and 2.3) consists of a PT55 spiral line micro-pulser and a trigger isolated spark gap. The custom high voltage trigger delivers a trigger pulse of about 14 kV to the knife edge center plane of the main field-distortion triggered spark gap switch and initiates the capacitor's fast discharge into the wire. The custom high voltage trigger was used in order to deliver a sharp front edge and clean high voltage pulse in order to minimize system jitter.

Once the capacitor is fully charged and prior to initiating the high voltage discharge into the load, a pre-trigger of a few microseconds ahead of the PT55 trigger automatically disables the power supply high voltage. After the discharge, the PT55 DC power supply is turned off at a push button and a pneumatic switch (see figure 2.1) allows us to discharge of any remaining charge in the capacitor into a 1.5 MΩ resistor connected to the ground. The PT55 was wrapped in aluminum sheets connected to a ground mesh in order to to record clean signals and more importantly prevented the PT55 from accidentally triggering the ICCD camera.

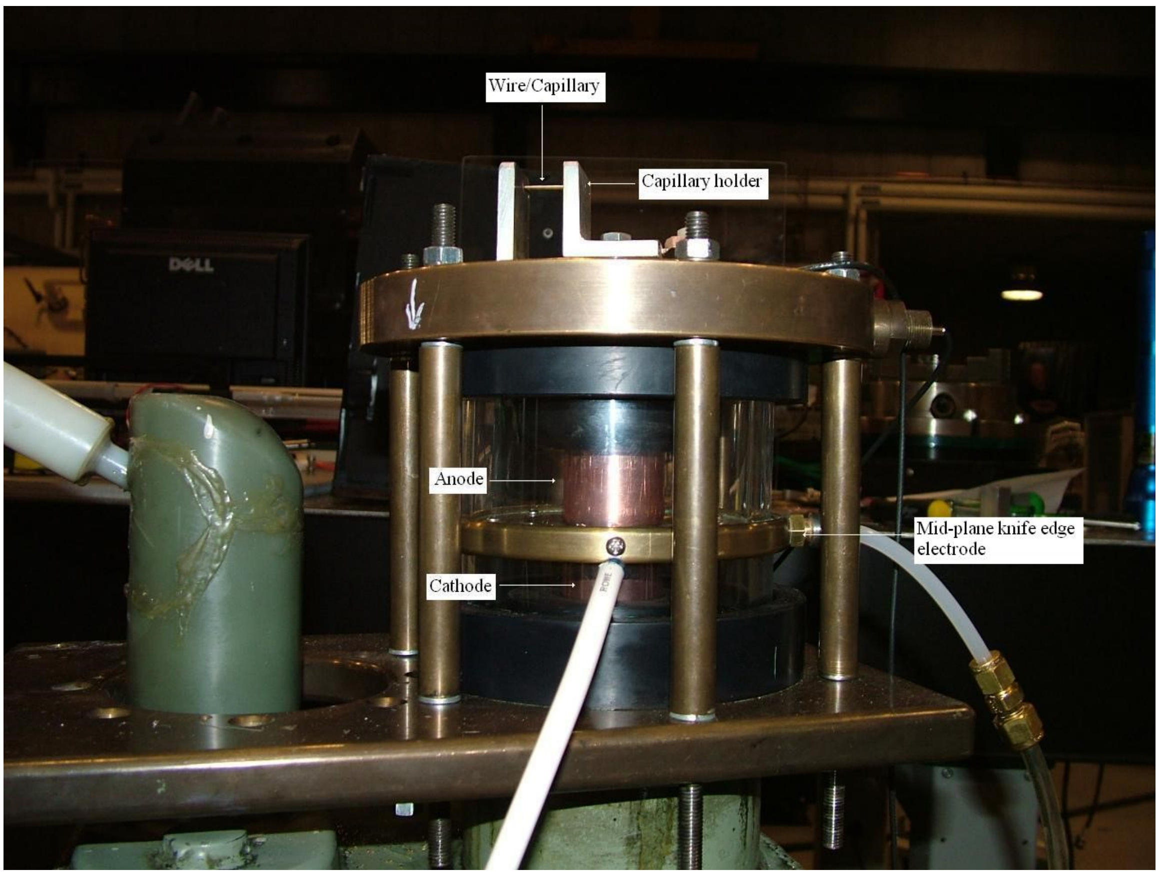

Figure 2.2: Capacitive discharge setup.

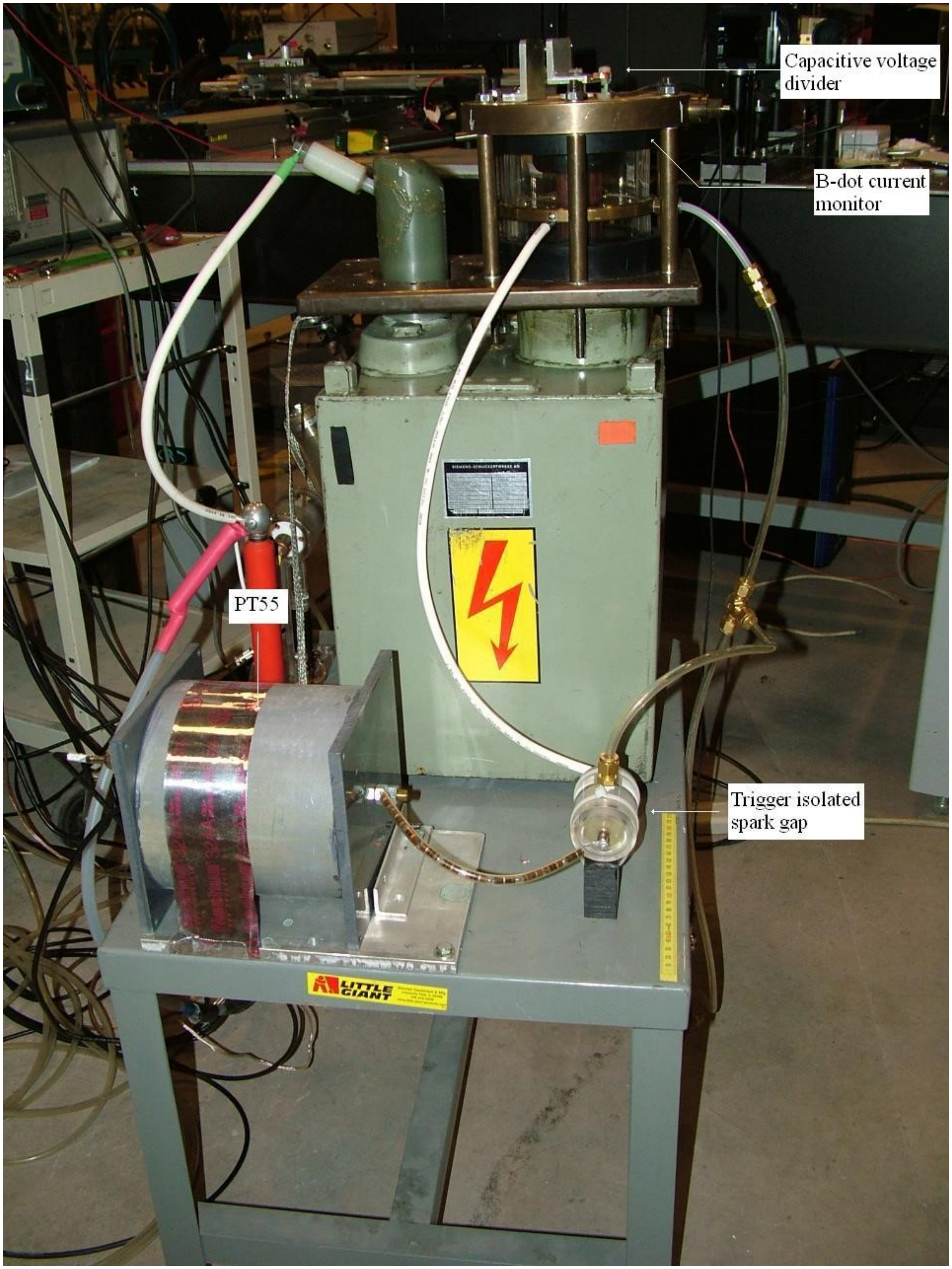

Figure 2.3: High voltage trigger generator.

2.2 Wires and Capillaries

The wires used were aluminum with a thickness of 125 microns. The wire and capillary are held in place by two L-shaped aluminum electrodes. Each L-shaped aluminum electrode has a 0.5 mm diameter through opening for the wire to pass through and a 1.2 mm diameter opening along half its face thickness to hold the capillary. Before inserting the wire, a glass capillary with an outer diameter of 1 mm, an inner diameter of 0.9mm, and a length of 2.8 cm is inserted into the electrodes, and the electrodes are secured. After the capillary is inserted, the wire is inserted through both electrodes. Because the capillaries were not ordered to length (due to the high cost), they were cut to an approximate consistent length.

Initially the wires were cut to a length of 3.81 cm (1.5"), and inserted such that a small amount of wire would hang out of each hole in the electrode in order to ensure contact between the wire and the electrodes. After several experiments were performed it was decided that tension needed to be added to the aluminum wires in order to ensure contact between the electrodes as well as keep the wire as straight as possible. Two plastic insulators were machined to a height slightly lower than the holes for the wire inserts. These insulators were placed on the sides of the electrodes in order to prevent contact between the wire and the electrode outside of the holes. The wires were cut to a length of 3 inches (7.62 cm), and then inserted with an equal amount of excess protruding from each electrode. A split shot fishing weight was then clamped on the each side of the wire, thus creating tension to ensure contact with the wire at the ends of each electrode hole (see figure 2.4).

The length in between each electrode was measured before each discharge. These lengths were averaged in order to account for measurement errors and the mean was taken. A separate mean was taken for the 2.3 kV series and the 7 kV series due to the length of capillaries varying slightly. For the 2.3 kV series the measured length was 2.31 $\pm$ 0.029 cm. For the 7kV series the measured length was 2.30 $\pm$ 0.024 cm.

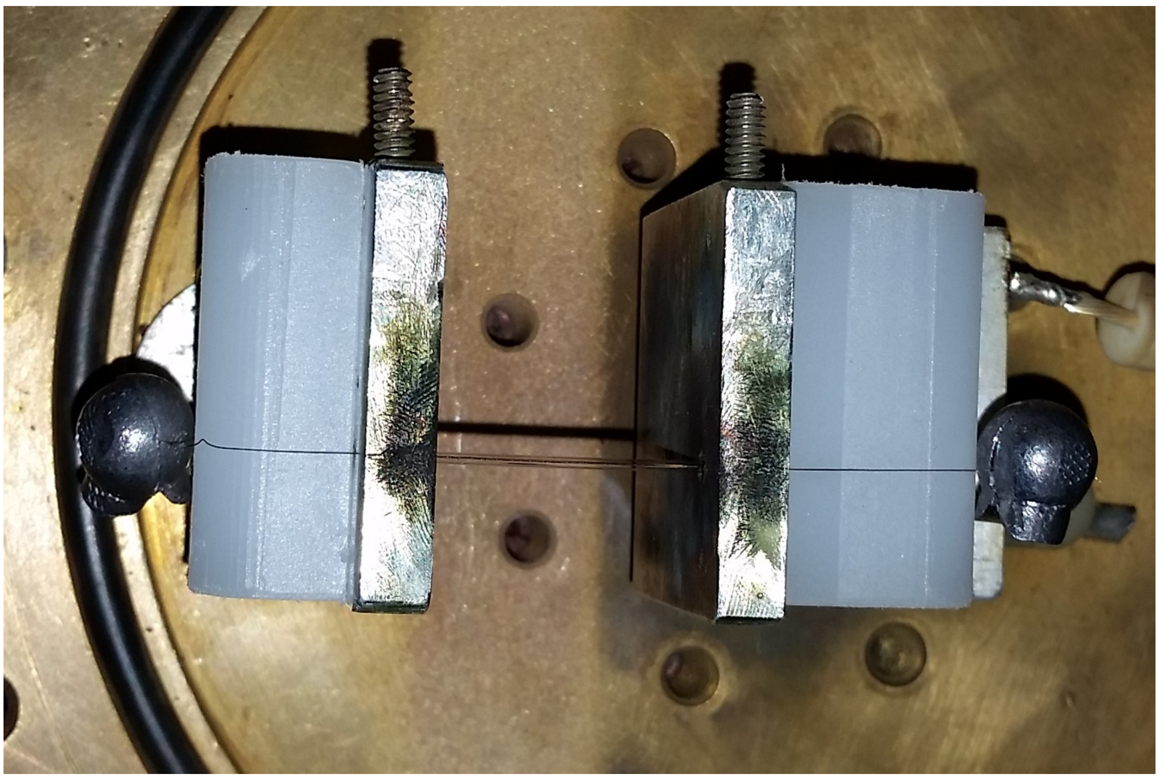

Figure 2.4: Al wire with tension weights attached.

2.3 Rogowski Coil

The derivative of the current from the discharge was measured by means of a Rogowski Coil place around the anode before the electrode. Prior to insertion into the system, the Rogowski coil was first calibrated by Dr. Chouffani using a current viewing resistor (CVR). The calibration resistor used has a resistance value of 0.1038 Ω with an uncertainty of 0.2%. Figure 2.5 shows the Rogowski calibration setup. Three capacitors with identical capacitance and inductance (35 nF and 20 nH respectively) were charged in parallel to 5 kV through a 50 kΩ resistor. A mechanical switch with its contact point submerged in oil allowed the simultaneous discharge of the capacitors into the CVR. The CVR was connected between a conducting aluminum plate and a ground plate as shown in figure 2.5. The plates were isolated from each other through a 4.5 mill thick Teflon sheet. Upon discharge, current flows from the capacitors, through the Rogowski coil air core, and into the CVR.

Figure 2.5: Rogowski coil calibration setup (left) and CVR signal output (right)

The signals from the CVR and Rogowski coil were recorded in an oscilloscope and analyzed. During the calibration measurements, we recorded a series of 10 voltage traces from the CVR and Rogowski coil respectively. The signals were averaged for better statistics and time integration of the average Rogowski signal was performed. The calibration factor was obtained by performing a least square fit to the CVR recorded voltage. The calibration factor obtain from the least square fit was equal to $4.7622 \times 10^{11} \frac{A}{V}$. The Rogowski signal was therefore multiplied by a factor of $4.7622 \times 10^{11} \frac{A}{Vs}$.

2.4 Voltage Divider

Voltage through the system was monitored through the use of a fast capacitive voltage divider constructed by Dr. Chouffani. The voltage divider is shown in figure 2.6. The capacitor C2 with a capacitance of 10pF was rated for a maximum voltage equal to 10 kV. The voltage divider was tested using an 82V maximum voltage pulsed power supply with pulse widths ranging from 1 to 20 s. The RC integrator with a time constant of 24 ns between the RG 223 cable and oscilloscope was used to remove high frequency noise.

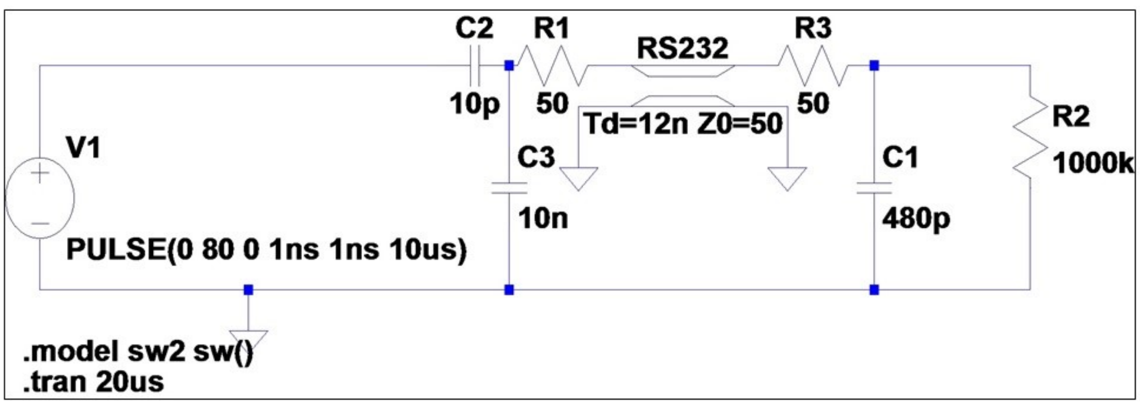

Figure 2.6: Wiring diagram of the voltage divider used to measure voltage across the wire.

2.5 System Inductance

The system inductance (including the wire) was found by diving the voltage data by the Rogowski data for the first few hundred nanoseconds following the methods of DeSilva and Kunz [35]. This can only be done in the very beginning of the discharge as it is only then that the IR and $I\frac{dL}{dt}$ terms are negligible due to the fact that very little ohmic heating has taken place, and the wire radius has not expanded. Making this assumption measured voltage U can be written as $U = L\frac{dI}{dt}$, and the inductance term can be found by calculating $L = \frac{U}{\frac{dI}{dt}}$. Additionally, the inductance was calculated using the IR term when $R = 0.6\Omega$ making $L = \frac{U-IR}{\frac{dI}{dt}}$, and it was shown that the value of inductance is in the same range. When looking at the value of L calculated using this method for the 125 micron Al wire at 2.3 kV and 7 kV the inductance of the entire system is estimated to be 67.5 nH as seen in figures 2.7 and 2.8. In order to confirm this value, the data collected from another set of experiments using a 5 mill Cu wire at 8 kV was used. The value of the inductance estimated from the 127 micron Cu wire experiments verified the range of the system inductance to be between 60 and 80 nF as seen in figure 2.9. The smaller inductance of the Cu wire is due mostly to a difference in length.

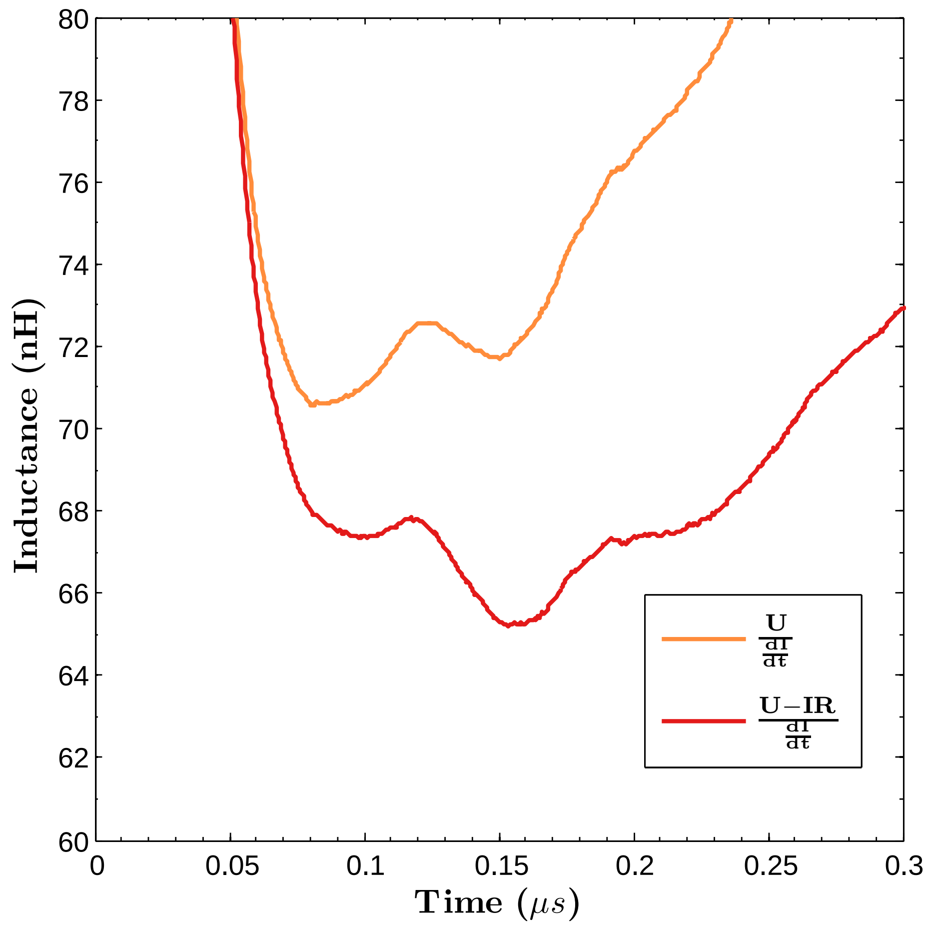

Figure 2.7: $\frac{U}{\frac{dI}{dt}}$ and $\frac{U-IR}{\frac{dI}{dt}}$ for the first 300 ns of the Al wire discharge at 2.3 kV

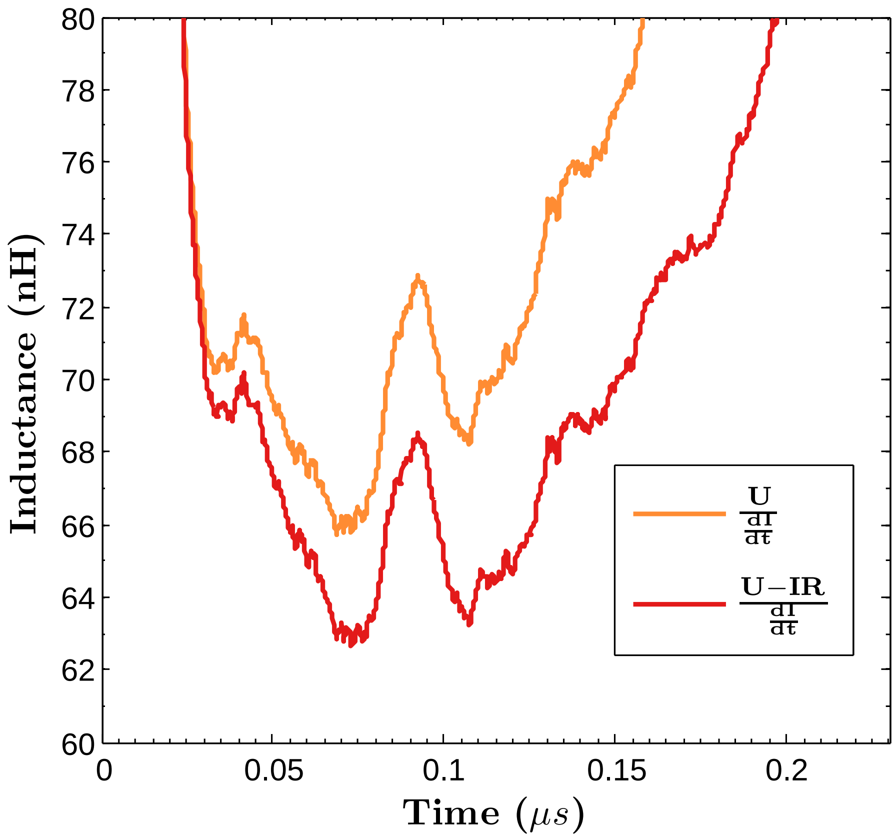

Figure 2.8: $\frac{U}{\frac{dI}{dt}}$ and $\frac{U-IR}{\frac{dI}{dt}}$ for the first 230 ns of the Al wire discharge at 7 kV

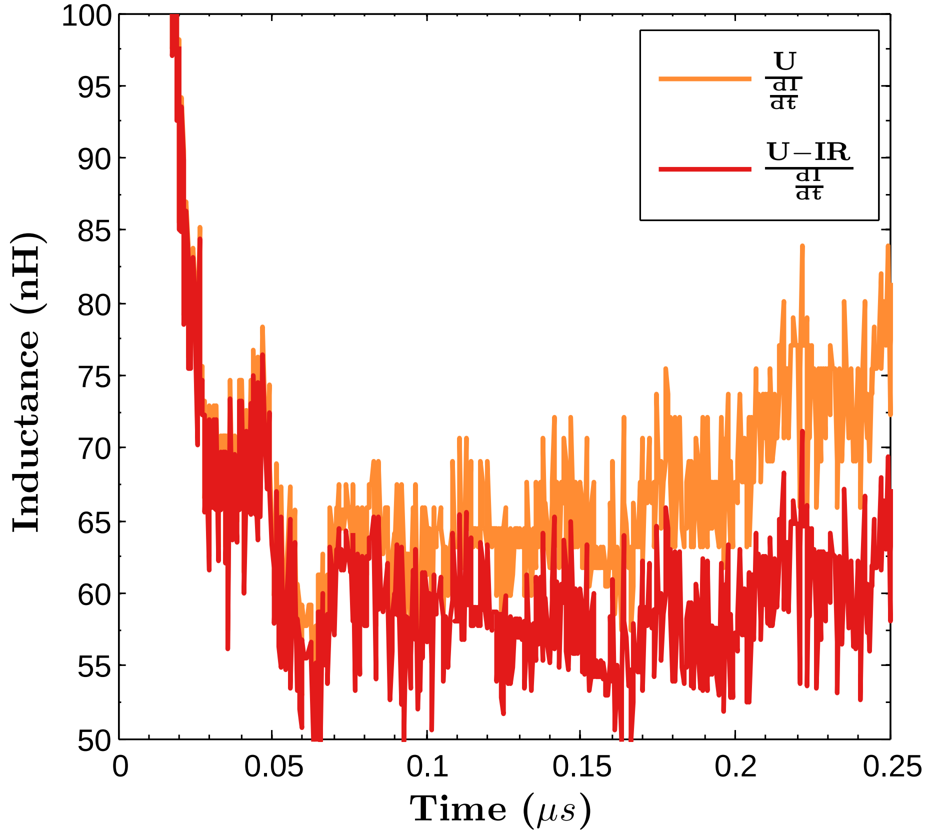

Figure 2.9: $\frac{U}{\frac{dI}{dt}}$ and $\frac{U-IR}{\frac{dI}{dt}}$ for the first 250 ns of a Cu wire discharge at 8 kV

2.6 ICCD

The ICCD used for these experiments was a Princeton Instruments PI-MAX4 1024i fast gated camera. The PI-MAX 4 used had a fast gated, gen III, high blue intensifier which allowed for short gate times as low as 2.9 ns, as well as a Quantum efficiency around 30-50% in the visible range. The phosphor used in the camera was a P46, however to avoid even lesser "ghosting" only one frame per explosion was recorded.

The calibration for the ICCD was made by illuminating a glass capillary with a 1 mm outer diameter. Several pictures were then taken of the capillary, and four good calibration photos were used to determine the pixel calibration (shown in figure 2.10). The pixel width of the capillary was determined for each calibration photo, and the average pixel diameter was found to be $52 \pm 2.11 \frac{pixel}{mm}$.

The trigger for the camera was a TTL pulse sent from the same generator that triggers the PT55. The Lightfield software for the camera allows the user to adjust the trigger delay of the camera as well as the gate width. The gate width was always set to 50 ns, and the camera trigger delay was adjusted for each discharge in order to "strobe" through the evolution of the wire explosion. The delay for each discharge also accounted for the cable delay in both the camera trigger cable as well as the voltage probe and Rogowski cables. The gain across the intensifier in the ICCD was adjusted for each discharge in order to maximize the signal to noise ratio. Neutral density filters were used for brighter images to avoid saturation.

The PI-MAX4 and Lightfield software allow for one to take a dark background image. This dark background image is taken by recording the CCD values with the intensifier in the negative voltage bias (off). In order to ensure this was a true dark background, it was taken with the lens cap attached.

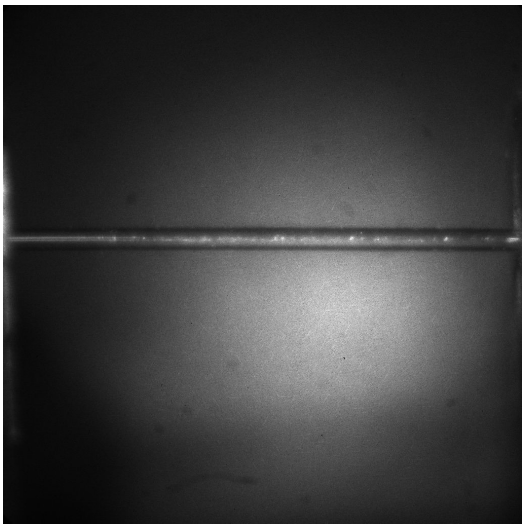

(a) Calibration 1

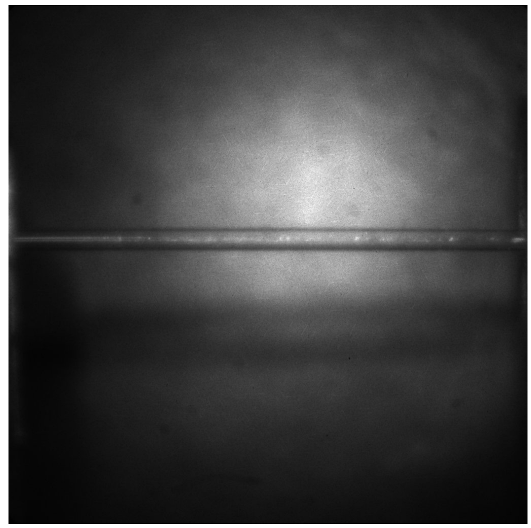

(b) Calibration 2

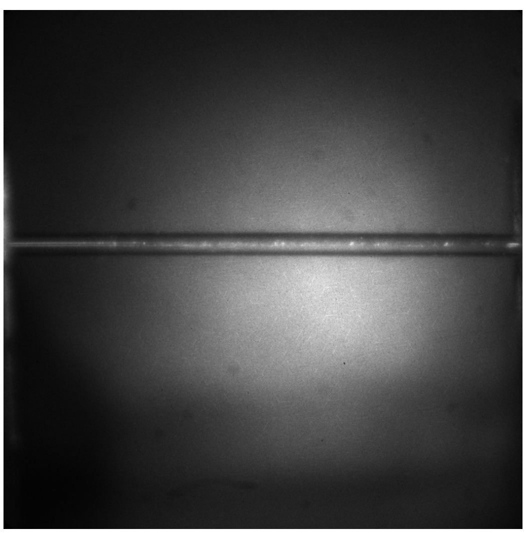

(c) Calibration 3

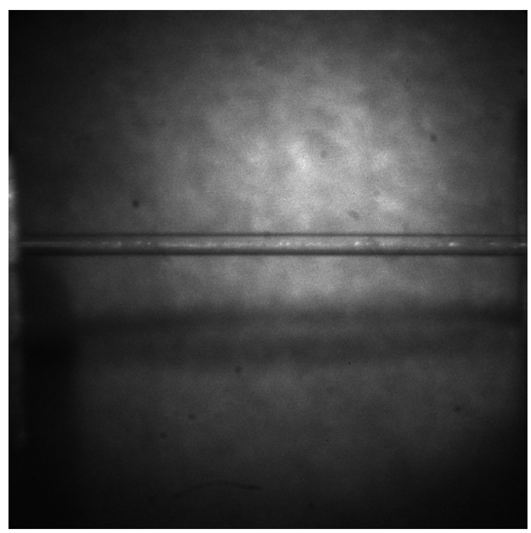

(d) Calibration 4

Figure 2.10: ICCD calibration images

Chapter 3

Data Analysis

3.1 Radius Analysis

Each radius measurement was estimated by taking eight different vertical cross sections of the ICCD image. For each of these cross sections a window was chosen, and the normalized second moment of the data in this window was calculated. 3.1 shows a sample of cross section data. The normalized second moment gives σ^2 for that measurement, and then the diameter of the wire can be calculating from $D = 4\sigma$. After all eight cross section measurements are found they are averaged to get a mean wire diameter value in pixels for each image, as well as a standard deviation to find the variance. This diameter is then divided by two in order to find the radius in pixels. The radius in pixels is then divided by the ICCD calibration of $52 \pm 2.11 \frac{pixel}{mm}$ in order to give the radius in mm. In order to account for propagation of uncertainty the uncertainty in the radius is calculated by $\sigma_r = |\frac{r_p}{c}|\sqrt{(\frac{\sigma_{rp}}{r_p})^2 + (\frac{\sigma_c}{c})^2}$ where σ_r is the variance of the radius in mm, r_p is the radius in pixels, σ_{r_p} is the variance of the radius in pixels, c is the calibration factor, and σ_c is the variance in

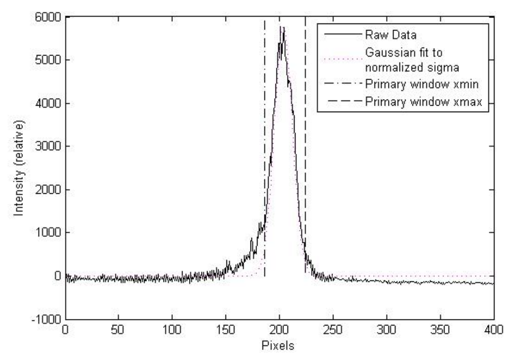

Figure 3.1: Sample of image cross section data.

the calibration factor.

3.2 Noise Filtering

Due to the bandwidth of the scope, there is a significant amount of inherent noise. In order to reduce the amount of noise in the traces a moving average filter was used [36]. The span was adjusted to allow for the best noise reduction while still maintaining the shape of the peak. For the 2.3 kV data a span of 101 data points was used for both the voltage probe and the Rogowski coil data. For the 7 kV data a span of 101 data points was used for the voltage probe data, and a span of 151 data points was used for the Rogowski coil data. Figures 3.2 and 3.3 show the raw data compared to the filtered data around the peaks.

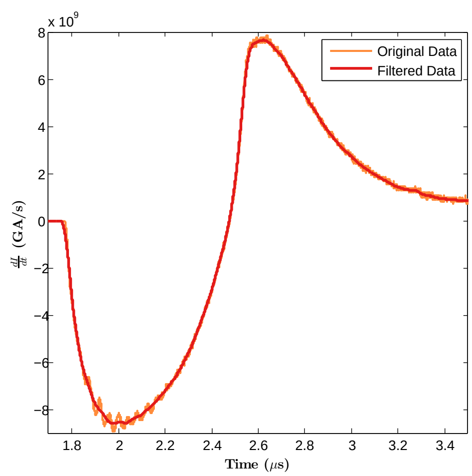

(a) Raw and filtered Rogowski Coil data.

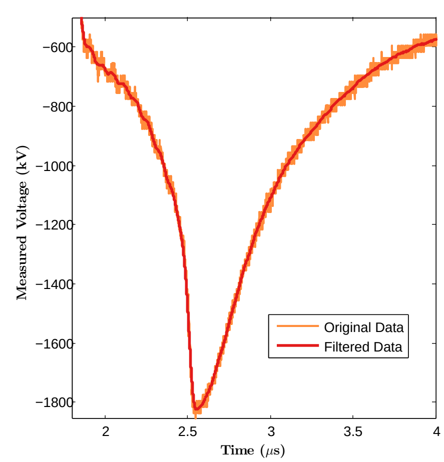

(b) Raw and filtered voltage probe data.

Figure 3.2: 2.3 kV raw data and filtered data.

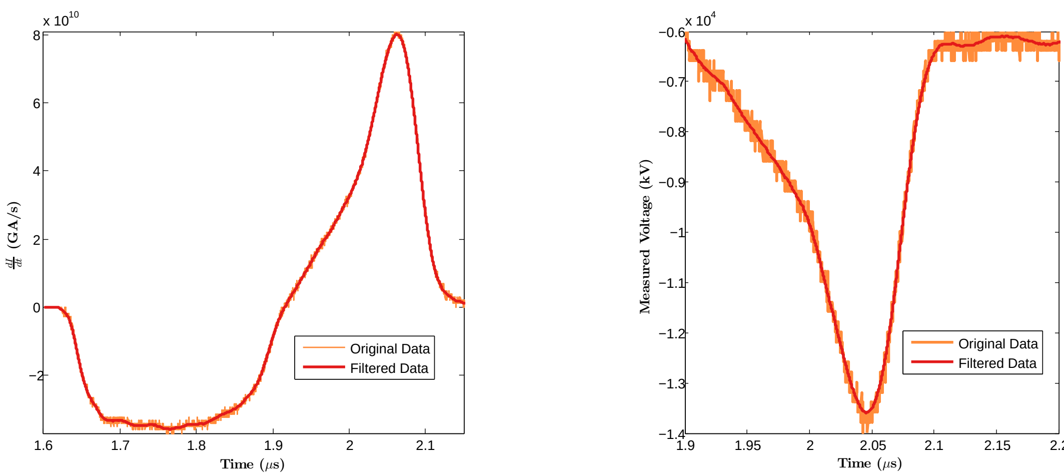

(a) Raw and filtered Rogowski Coil data. (b) Raw and filtered voltage probe data.

Figure 3.3: 7 kV raw data and filtered data.

3.3 Resistive Voltage and Current

In order to obtain the Current data, the data from the Rogowski Coil needed to be multiplied by the calibration constant of $4.76 \times 10^{1}1\frac{A}{Vs}$ and integrated over time.

Because voltage consists of three terms, the measured voltage must be corrected in order to obtain the resistive voltage. The $I\frac{dL}{dt}$ term is assumed negligible, and not accounted for in the resistive voltage correction. In order to account for the $L\frac{dI}{dt}$ term the relation $V = U - L\frac{dI}{dt}$ where V is the resistive voltage, U is the measured voltage, L is the stray system inductance with a value of 67.5 nF, and $\frac{dI}{dt}$ is obtained from the Rogowski Coil.

3.4 Resistance and Resistivity

3.4.1 Resistance

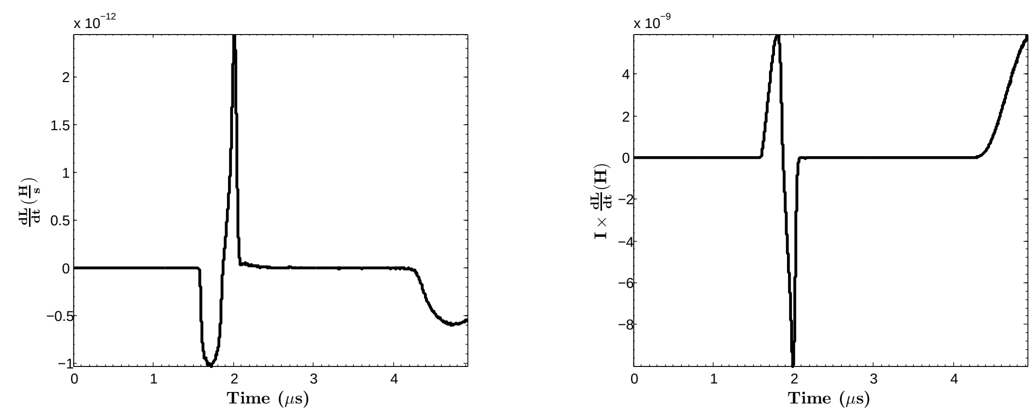

(a) $\frac{dL}{dt}$ (b) I $\times\frac{dL}{dt}$

Figure 3.4: $\frac{dL}{dt}$ (a) and $I \times \frac{dL}{dt}$ (b) for a 7kV discharge.

Resistance is found by using the total voltage and solving for the resistance term: $R(t) = \frac{U - L(\frac{dI}{dt}) - I(t)\frac{dL}{dt}}{I(t)}$ where U is the measured voltage, L is the stray inductance of the system estimated to be 67.5 nH, $I(t)$ is the integrated current from the Rogowski data, and $\frac{dI}{dt}$ is measured from the Rogowski coil. $\frac{dL}{dt}$ is determined by using the change in radius of the wire such that $\frac{dL}{dt} = \frac{\mu_0}{2\pi} l \frac{d}{dt}(I(t)(ln(\frac{r_p(t)}{r_s} + 0.5)))$ where l is the length of the plasma column, $r_p(t)$ is the radius of the plasma as a function of time, and r_s is the initial wire radius [28]. Because the change in inductance is dependent on the change in radius of the plasma column, if the radius is constant the $\frac{dL}{dt}$ term goes to zero, as is the case with the 2.3 kV data. In the case of the 7kV data, $\frac{dL}{dt}$ is on the order of 10^{-12} and $I \times \frac{dL}{dt}$ is on the order of 10^{-8} as can be seen in figures 3.4a and 3.4b. It can therefore be concluded that the $I \times \frac{dL}{dt}$ term is negligible and can be ignored when performing Resistance calculations.

3.4.2 Resistivity

Resistivity is defined as $\rho = R\frac{A}{l}$ where R is the resistance, A is the cross sectional area of the wire, and l is the length of the wire. The cross sectional area of the wire was calculated with $A = \pi r^2$ using the radius found in section 3.1. Uncertainty propagation for the area was found by calculating $\sigma_A = 2\pi r \sigma_r$. This area was then used to calculate the resistance $\rho = R\frac{A}{l}$ by using the resistance at the time of the image, the area calculated using this radius, and the length of the wire as discussed in section 2.2. Uncertainty was calculated using $\sigma_\rho = R\frac{A}{l}\sqrt{(\frac{\sigma_A}{A})^2 + (\frac{\sigma_l}{l})^2}$.

3.5 Energy Deposition

Energy deposition is calculated by integrating the power $P = IV$ over time. This integration requires resistive voltage and should then be calculated as $E = \int Pdt = \int I(t)(U(t) - L\frac{dI}{dt})dt$ where $I(t)$ is the integrated current, $U(t)$ is the measured voltage, L is the stray inductance of the system estimated to be 67.5 nF, and $\frac{dI}{dt}$ is obtained from the Rogowski coil.

Chapter 4

Results and Conclusions

4.1 Jitter and Timing

Due to electronic jitter in the trigger the Δt between the trigger pulse and the actual discharge varied. In order to account for changes in this Δt, t was set to zero at a threshold current for the radius and resistivity measurements. This threshold current was chosen to be just above pre-discharge noise and oscillations. For the 2.3 kV discharges a threshold current of -230 A was chosen, and for the 7 kV discharges a threshold current of -80 A was chosen.

4.2 2.3 kV Discharge

4.2.1 Radius

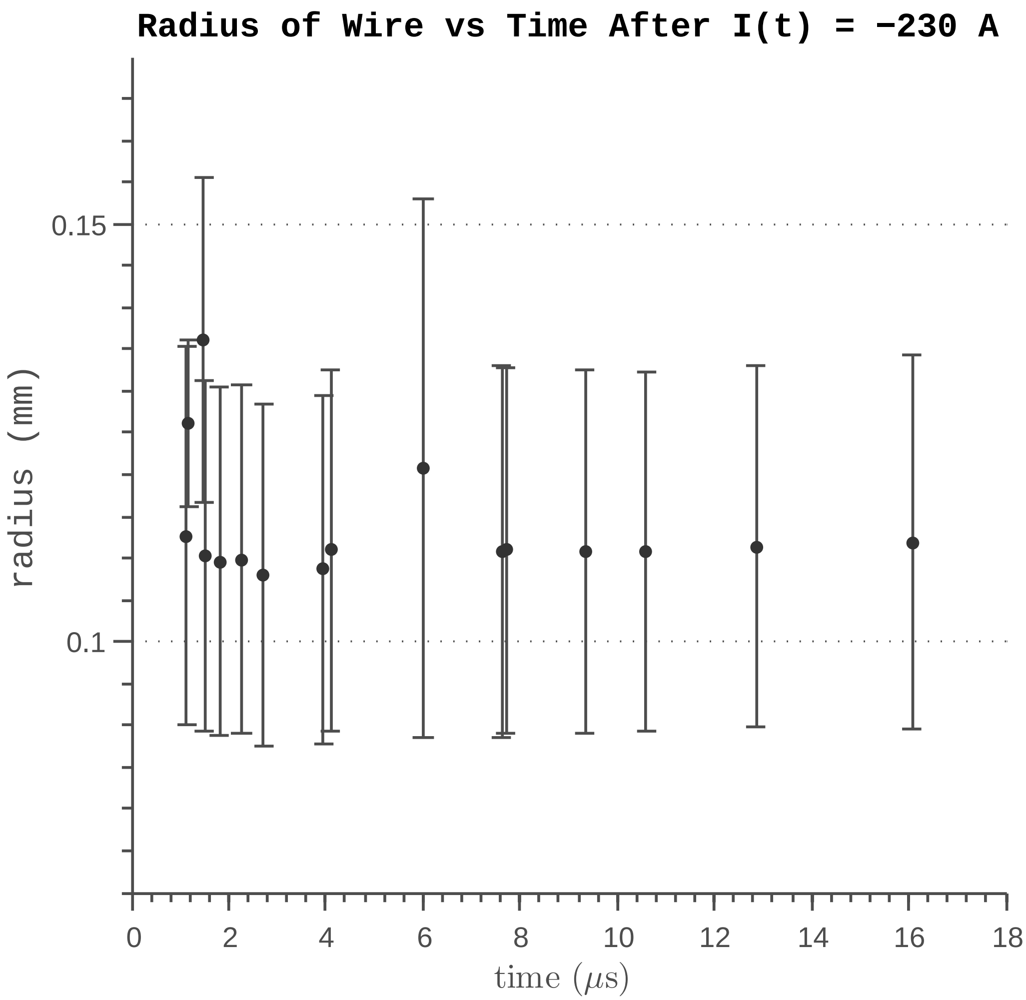

Figure 4.1: Radius vs. Time Taken From All 2.3 kV Discharges

4.2.2 Resistivity

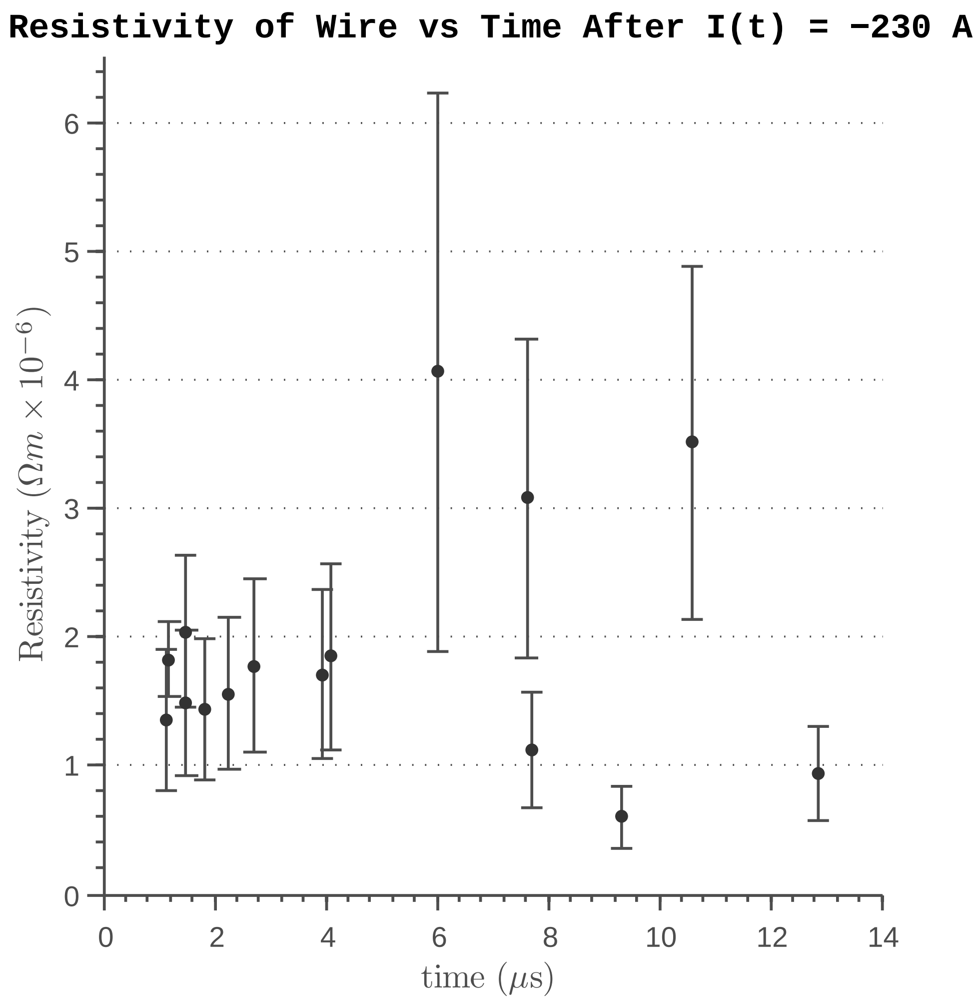

Figure 4.2: Resistivity measurements for 2.3 kV discharges

4.2.3 Discharge Images

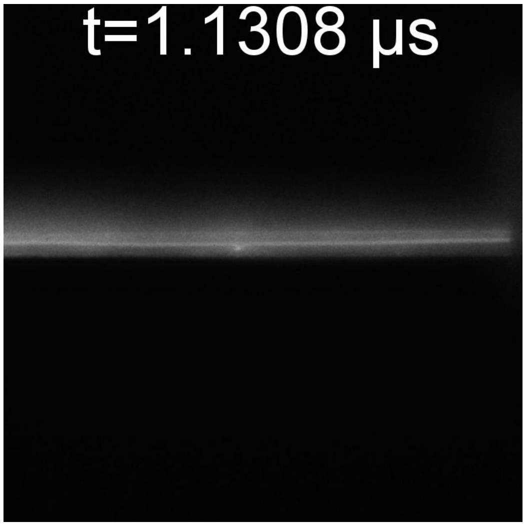

(a) Discharge 1

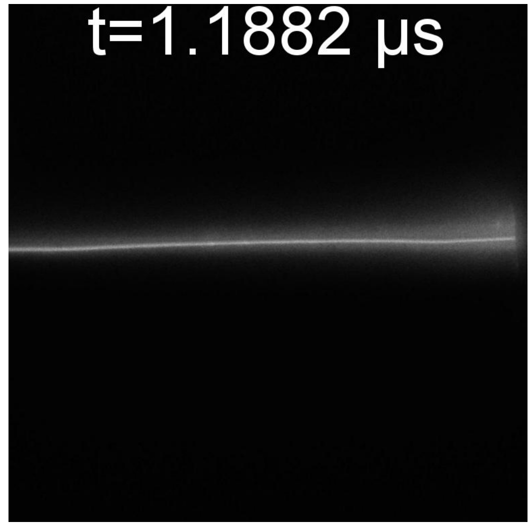

(b) Discharge 2

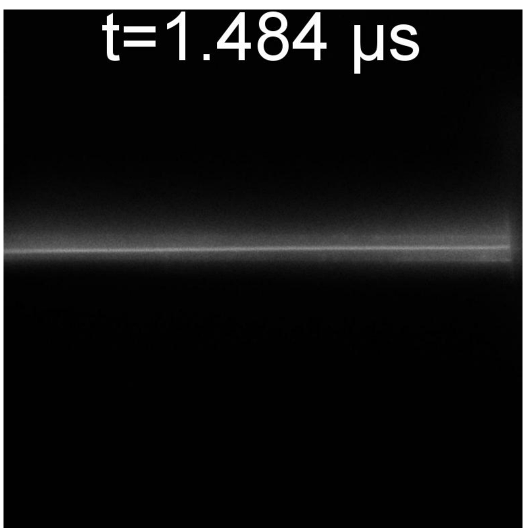

(c) Discharge 3

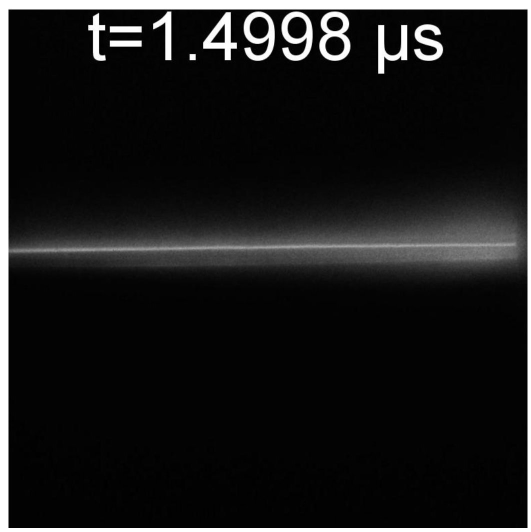

(d) Discharge 4

Figure 4.3: ICCD images of 2.3 kV discharges 1-4

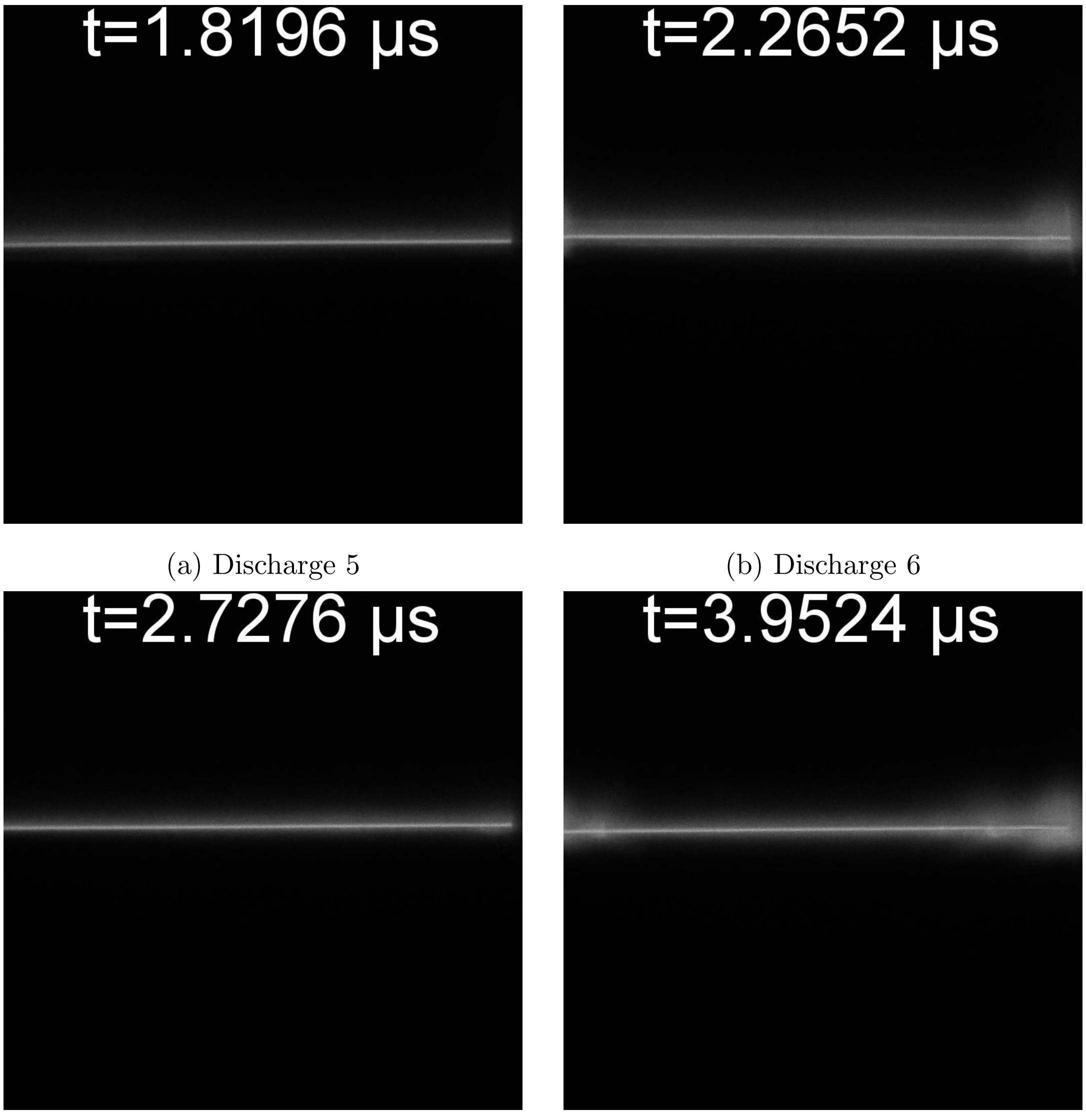

(a) Discharge 5 (b) Discharge 6

(c) Discharge 7 (d) Discharge 8

Figure 4.4: ICCD images of 2.3 kV discharges 5-8

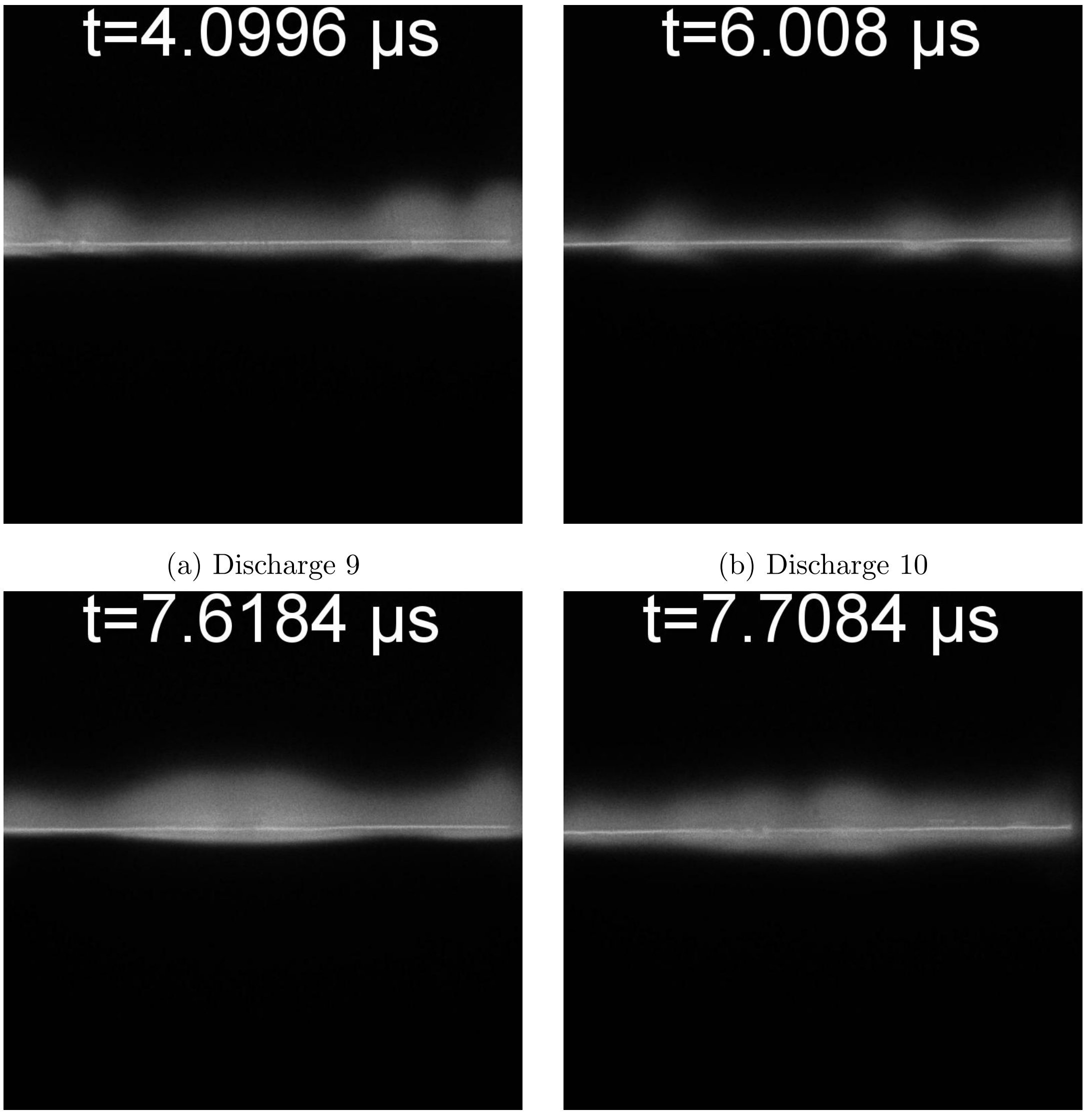

(a) Discharge 9

(b) Discharge 10

(c) Discharge 11

(d) Discharge 12

Figure 4.5: ICCD images of 2.3 kV discharges 9-12

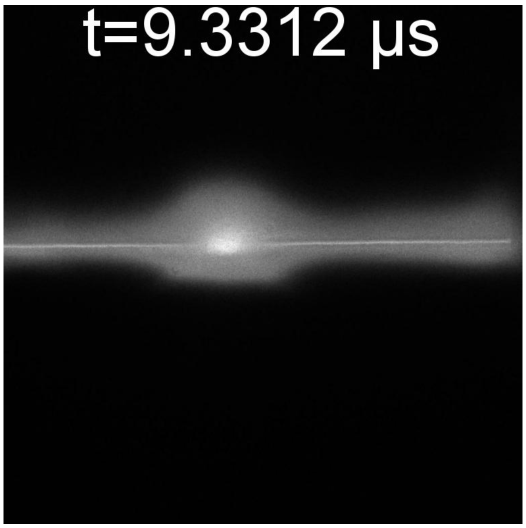

(a) Discharge 13

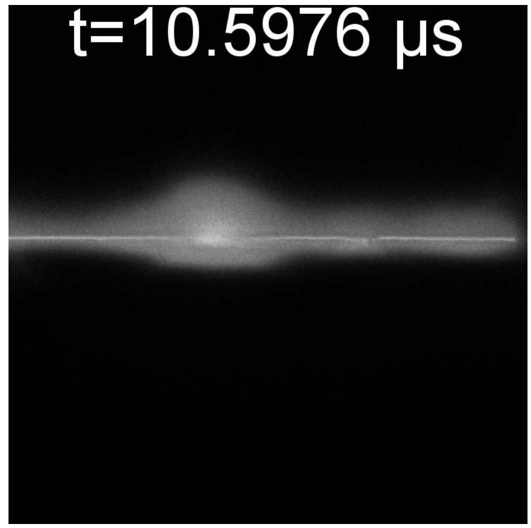

(b) Discharge 14

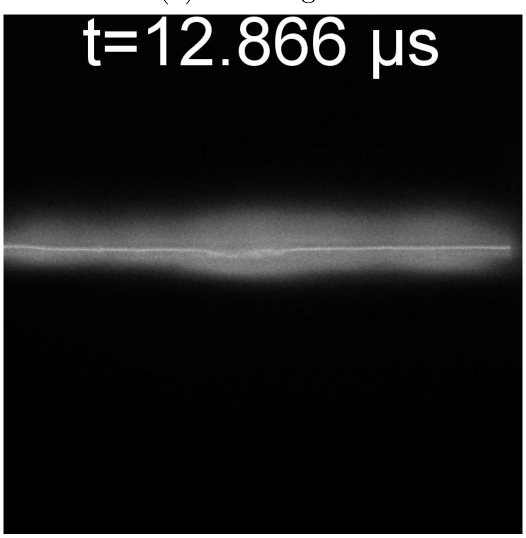

(c) Discharge 15

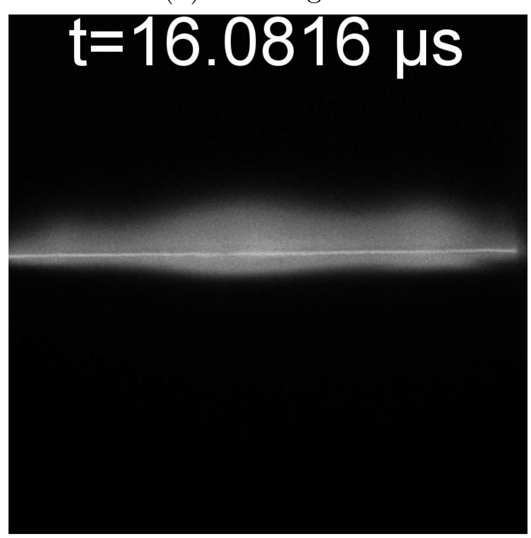

(d) Discharge 16

Figure 4.6: ICCD images of 2.3 kV discharges 13-16

4.2.4 Current, Voltage, Energy, and Resistance

While the camera trigger time may be the same for multiple discharges, it represents a different time in the explosion. This is due to the jitter from the electronics causing a different delay of each discharge.

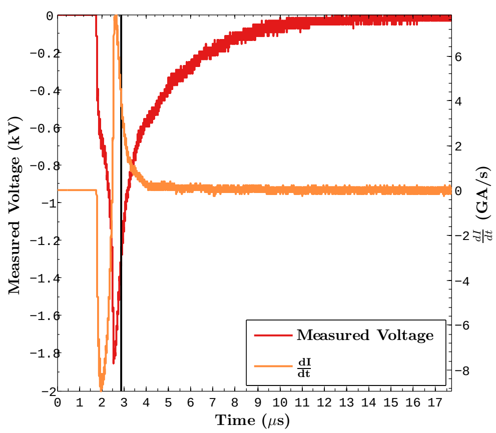

(a) Measured voltage and $\frac{dI}{dt}$ for discharge 1 (the vertical line marks the camera trigger)

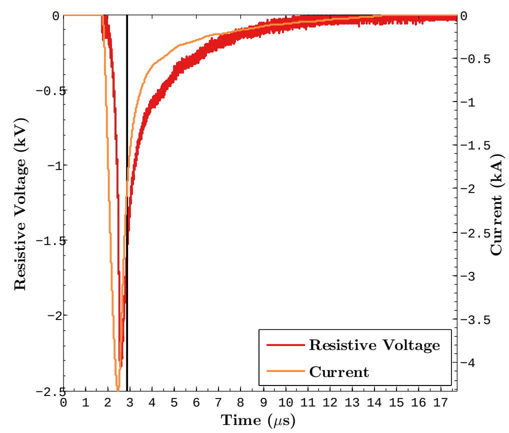

(b) Resistive voltage and current for discharge 1 (the vertical line marks the camera trigger)

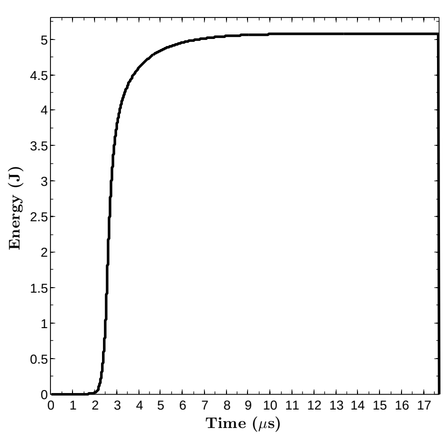

(c) Energy for discharge 1

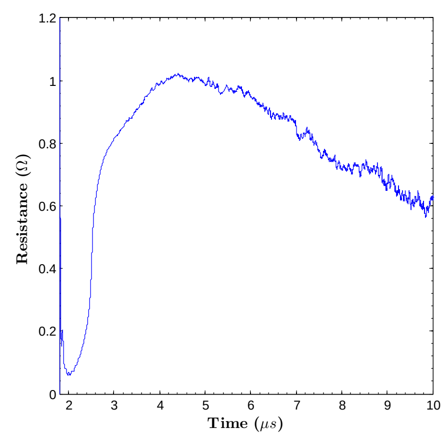

(d) Resistance for discharge 1

Figure 4.7: Measured voltage and $\frac{dI}{dt}$ (a), resistive voltage and current (b), energy (c), and resistance (d) for 2.3 kV discharge 1.

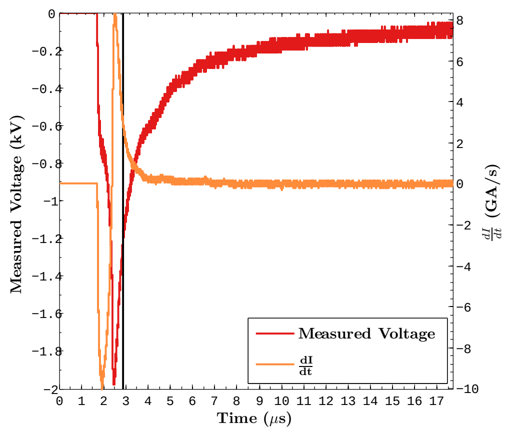

(a) Measured voltage and $\frac{dI}{dt}$ for discharge 2 (the vertical line marks the camera trigger)

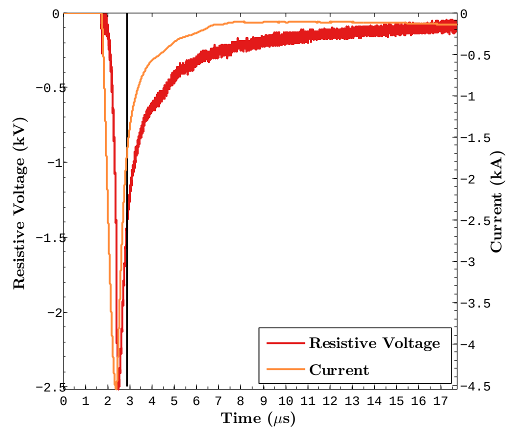

(b) Resistive voltage and current for discharge 2 (the vertical line marks the camera trigger)

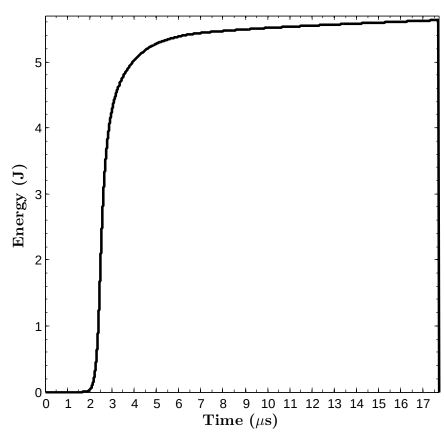

(c) Energy for discharge 2

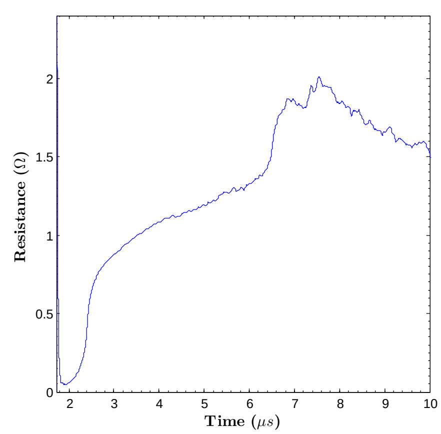

(d) Resistance for discharge 2

Figure 4.8: Measured voltage and $\frac{dI}{dt}$(a), resistive voltage and current (b), energy (c), and resistance (d) for 2.3 kV discharge 2.

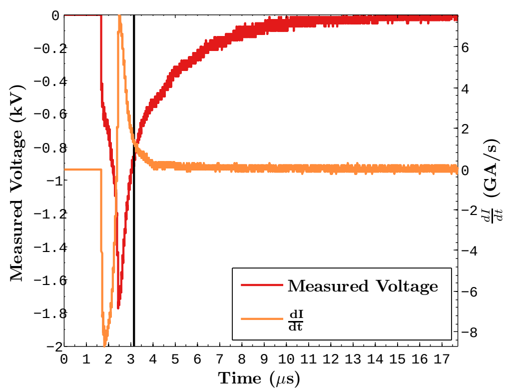

(a) Measured voltage and $\frac{dI}{dt}$ for discharge 3 (the vertical line marks the camera trigger)

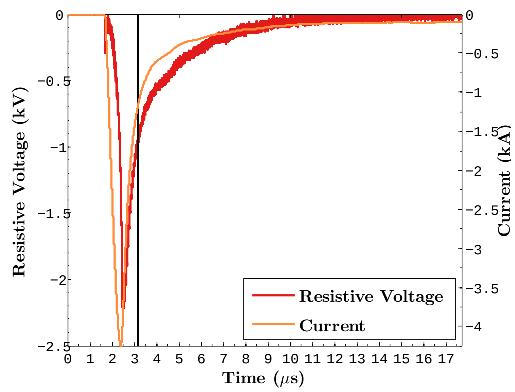

(b) Resistive voltage and current for discharge 3 (the vertical line marks the camera trigger)

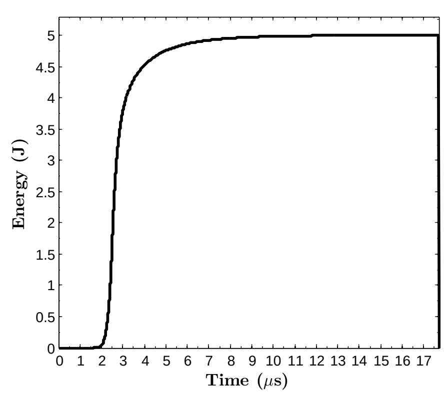

(c) Energy for discharge 3

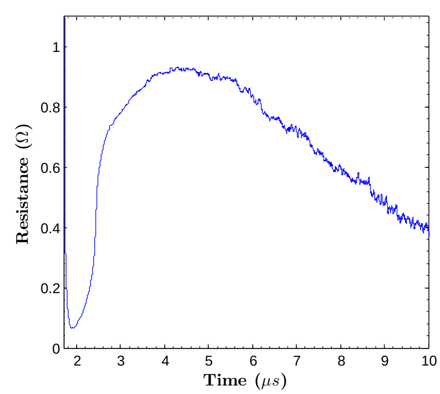

(d) Resistance for discharge 3

Figure 4.9: Measured voltage and $\frac{dI}{dt}$(a), resistive voltage and current (b), energy (c), and resistance (d) for 2.3 kV discharge 3.

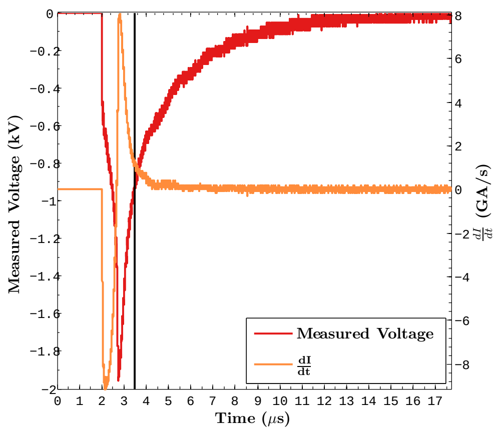

(a) Measured voltage and $\frac{dI}{dt}$ for discharge 4 (the vertical line marks the camera trigger)

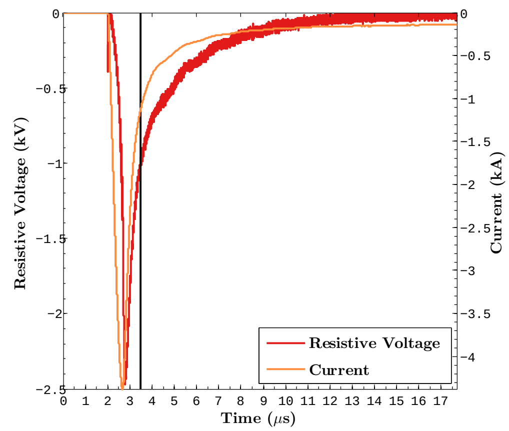

(b) Resistive voltage and current for discharge 4 (the vertical line marks the camera trigger)

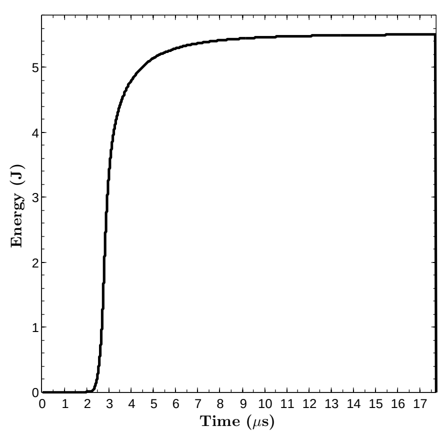

(c) Energy for discharge 4

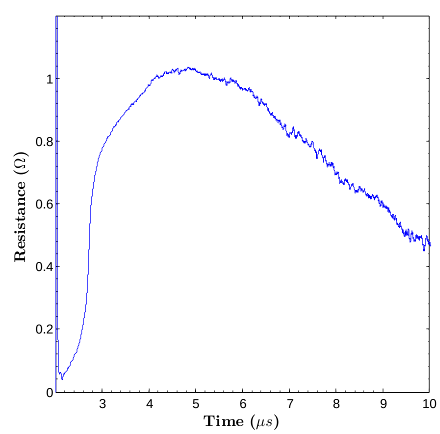

(d) Resistance for discharge 4

Figure 4.10: Measured voltage and $\frac{dI}{dt}$(a), resistive voltage and current (b), energy (c), and resistance (d) for 2.3 kV discharge 4.

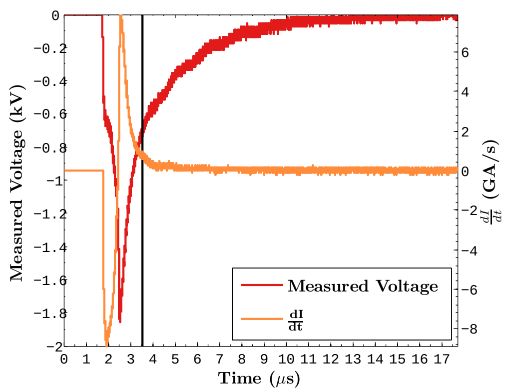

(a) Measured voltage and $\frac{dI}{dt}$ for discharge 5 (the vertical line marks the camera trigger)

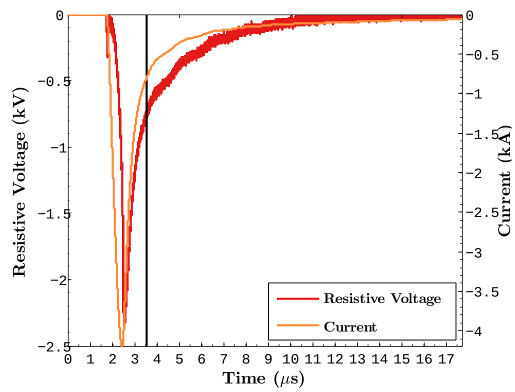

(b) Resistive voltage and current for discharge 5 (the vertical line marks the camera trigger)

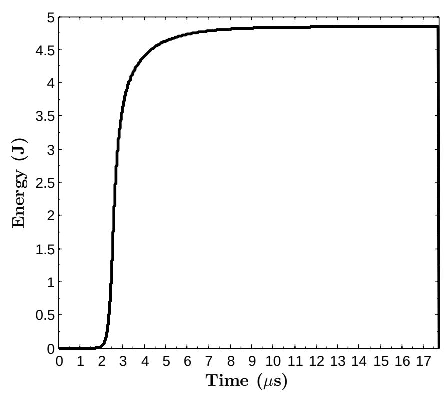

(c) Energy for discharge 5

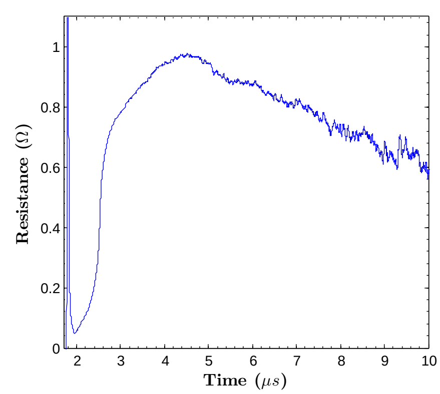

(d) Resistance for discharge 5

Figure 4.11: Measured voltage and $\frac{dI}{dt}$(a), resistive voltage and current (b), energy (c), and resistance (d) for 2.3 kV discharge 5.

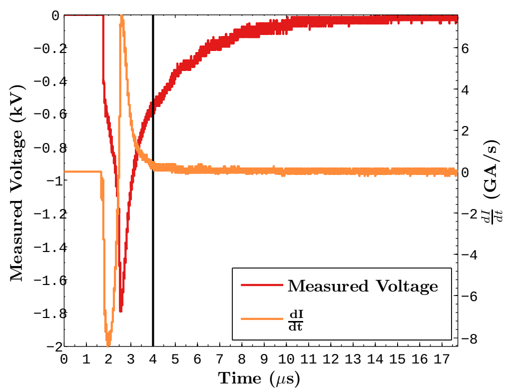

(a) Measured voltage and $\frac{dI}{dt}$ for discharge 6 (the vertical line marks the camera trigger)

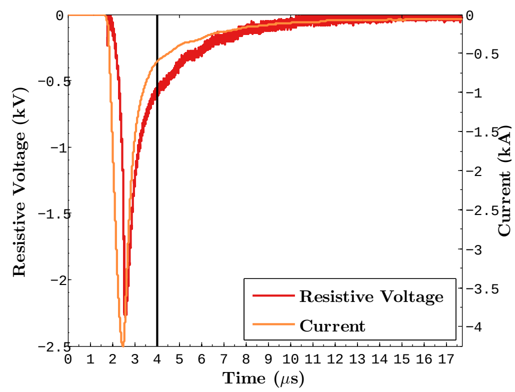

(b) Resistive voltage and current for discharge 6 (the vertical line marks the camera trigger)

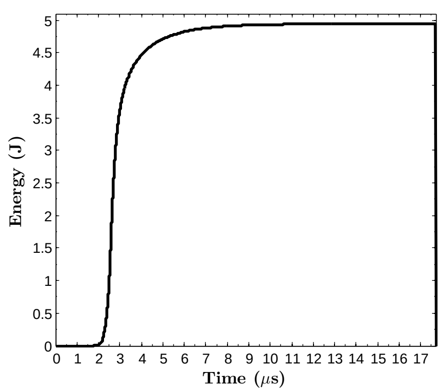

(c) Energy for discharge 6

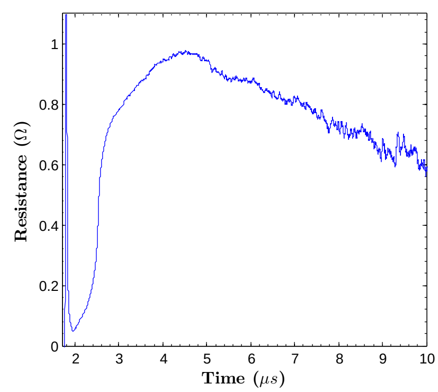

(d) Resistance for discharge 6

Figure 4.12: Measured voltage and $\frac{dI}{dt}$(a), resistive voltage and current (b), energy (c), and resistance (d) for 2.3 kV discharge 6.

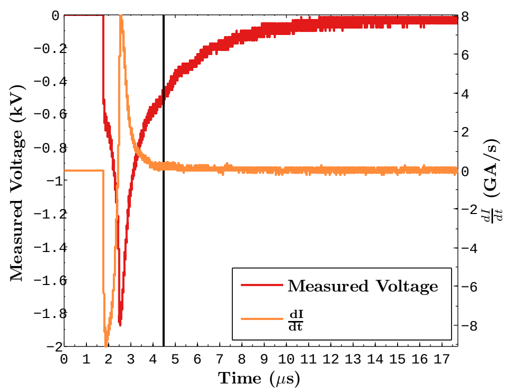

(a) Measured voltage and $\frac{dI}{dt}$ for discharge 7 (the vertical line marks the camera trigger)

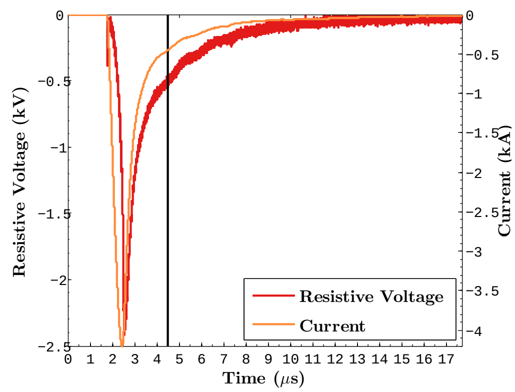

(b) Resistive voltage and current for discharge 7 (the vertical line marks the camera trigger)

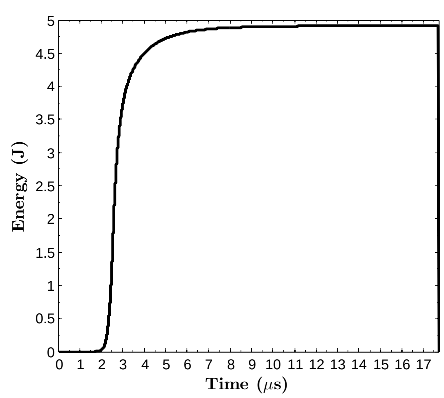

(c) Energy for discharge 7

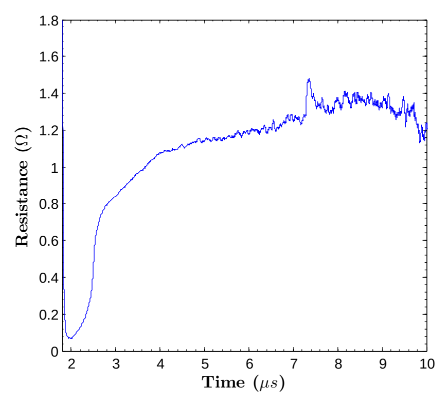

(d) Resistance for discharge 7

Figure 4.13: Measured voltage and $\frac{dI}{dt}$(a), resistive voltage and current (b), energy (c), and resistance (d) for 2.3 kV discharge 7.

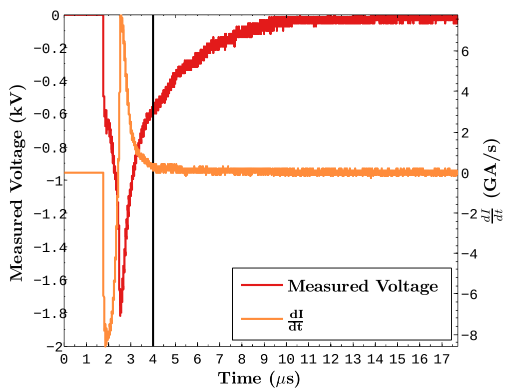

(a) Measured voltage and $\frac{dI}{dt}$ for discharge 8 (the vertical line marks the camera trigger)

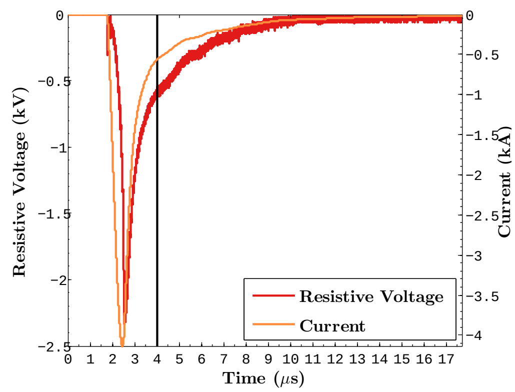

(b) Resistive voltage and current for discharge 8 (the vertical line marks the camera trigger)

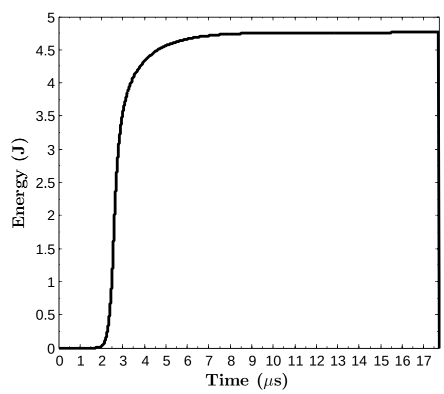

(c) Energy for discharge 8

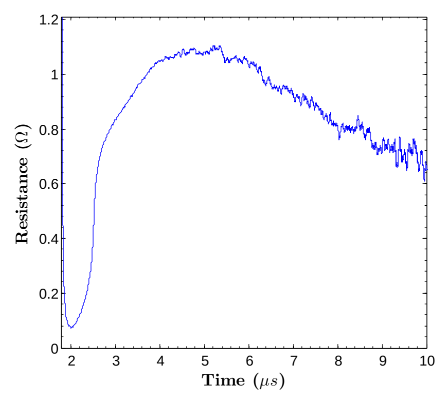

(d) Resistance for discharge 8

Figure 4.14: Measured voltage and $\frac{dI}{dt}$(a), resistive voltage and current (b), energy (c), and resistance (d) for 2.3 kV discharge 8.

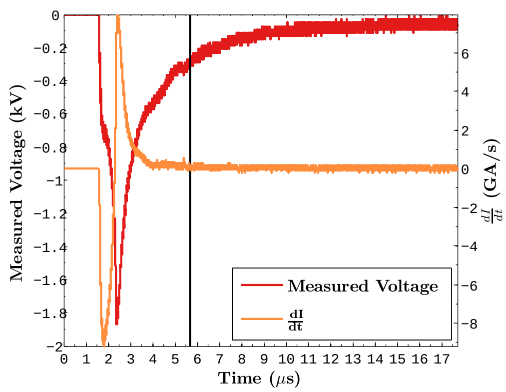

(a) Measured voltage and $\frac{dI}{dt}$ for discharge 9 (the vertical line marks the camera trigger)

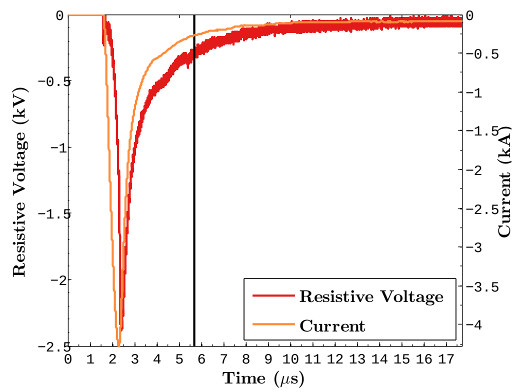

(b) Resistive voltage and current for discharge 9 (the vertical line marks the camera trigger)

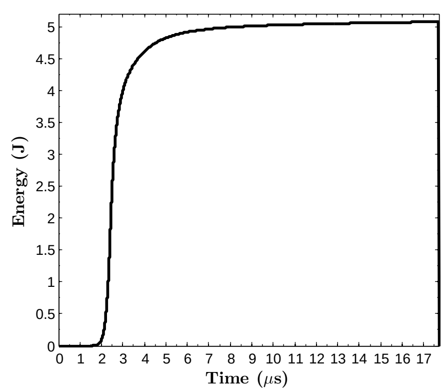

(c) Energy for discharge 9

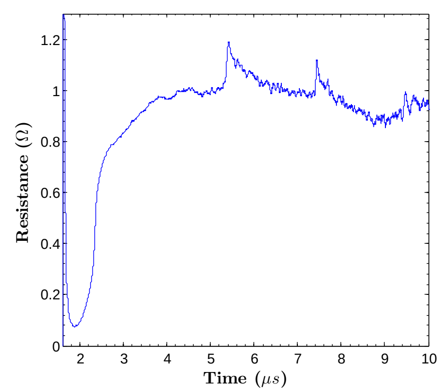

(d) Resistance for discharge 9

Figure 4.15: Measured voltage and $\frac{dI}{dt}$(a), resistive voltage and current (b), energy (c), and resistance (d) for 2.3 kV discharge 9.

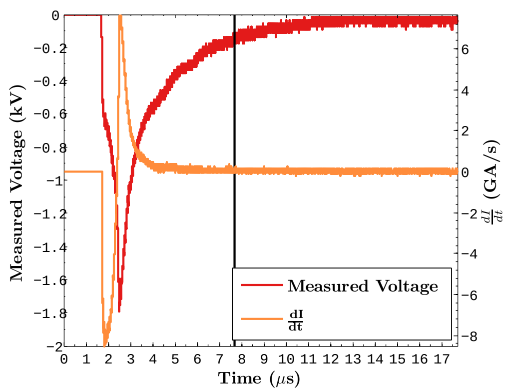

(a) Measured voltage and $\frac{dI}{dt}$ for discharge 10 (the vertical line marks the camera trigger)

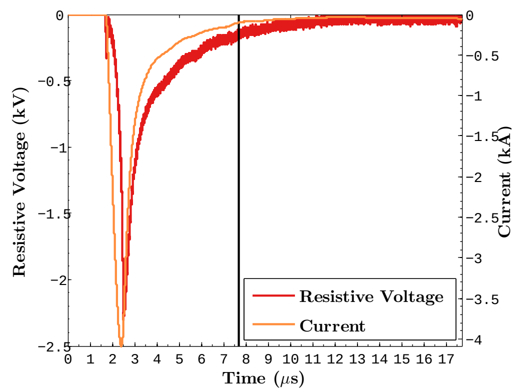

(b) Resistive voltage and current for discharge 10 (the vertical line marks the camera trigger)

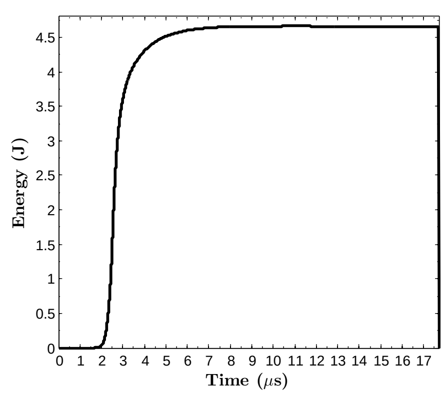

(c) Energy for discharge 10

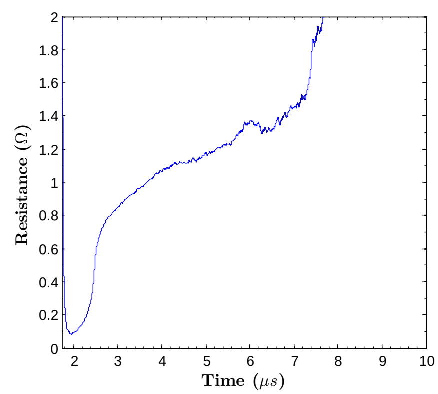

(d) Resistance for discharge 10

Figure 4.16: Measured voltage and $\frac{dI}{dt}$(a), resistive voltage and current (b), energy (c), and resistance (d) for 2.3 kV discharge 10.

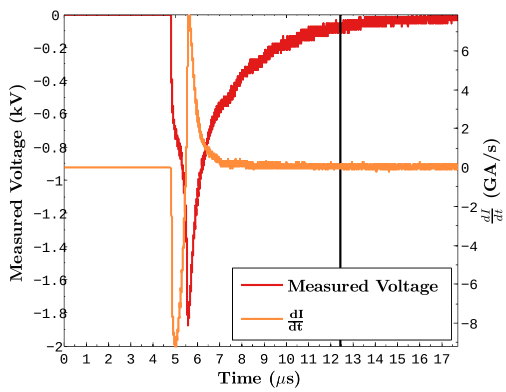

(a) Measured voltage and $\frac{dI}{dt}$ for discharge 11 (the vertical line marks the camera trigger)

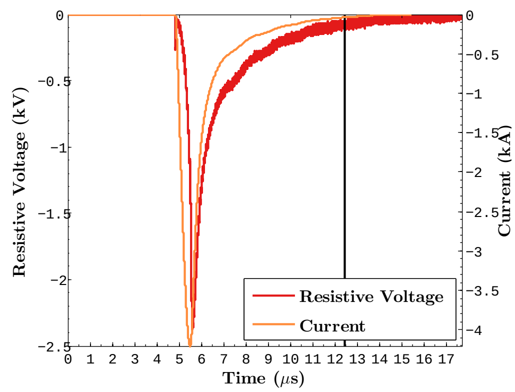

(b) Resistive voltage and current for discharge 11 (the vertical line marks the camera trigger)

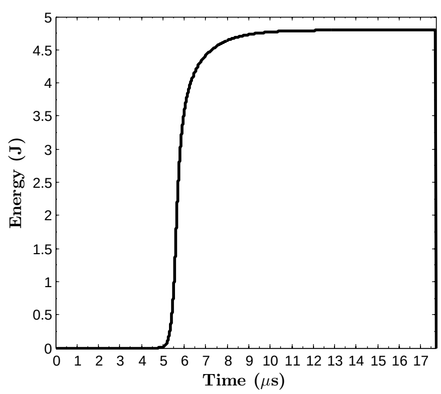

(c) Energy for discharge 11

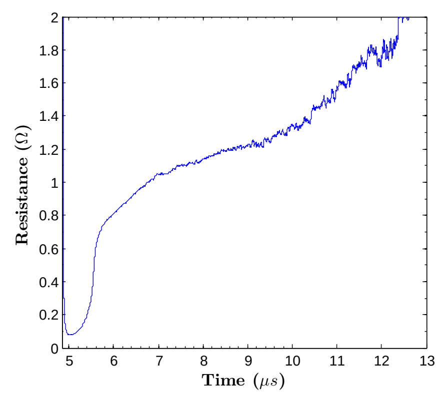

(d) Resistance for discharge 11

Figure 4.17: Measured voltage and $\frac{dI}{dt}$(a), resistive voltage and current (b), energy (c), and resistance (d) for 2.3 kV discharge 11.

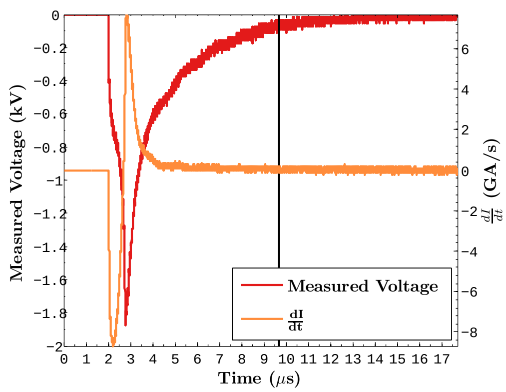

(a) Measured voltage and $\frac{dI}{dt}$ for discharge 12 (the vertical line marks the camera trigger)

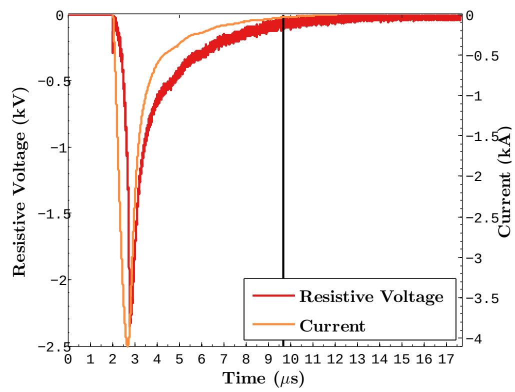

(b) Resistive voltage and current for discharge 12 (the vertical line marks the camera trigger)

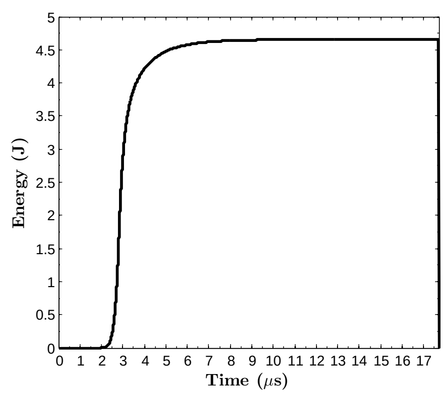

(c) Energy for discharge 12

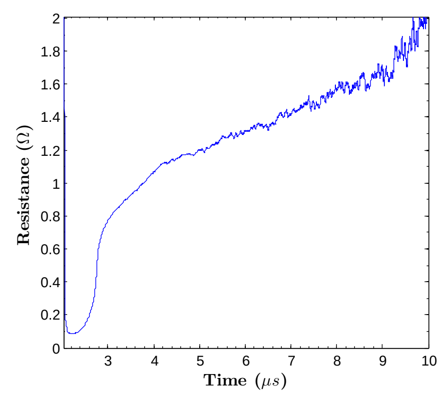

(d) Resistance for discharge 12

Figure 4.18: Measured voltage and $\frac{dI}{dt}$(a), resistive voltage and current (b), energy (c), and resistance (d) for 2.3 kV discharge 12.

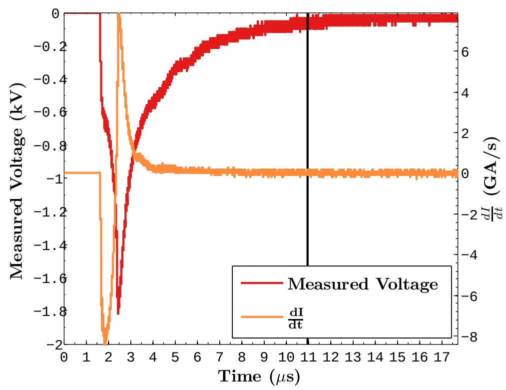

(a) Measured voltage and $\frac{dI}{dt}$ for discharge 13 (the vertical line marks the camera trigger)

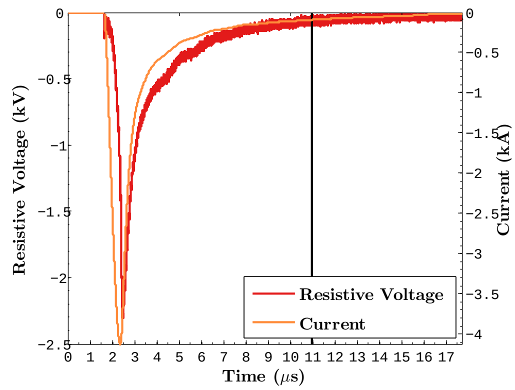

(b) Resistive voltage and current for discharge 13 (the vertical line marks the camera trigger)

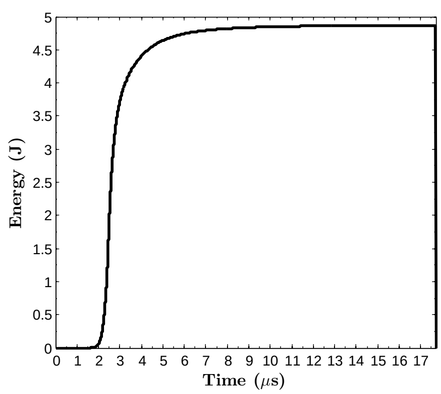

(c) Energy for discharge 13

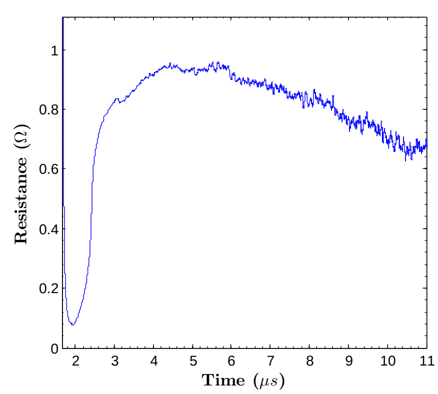

(d) Resistance for discharge 13

Figure 4.19: Measured voltage and $\frac{dI}{dt}$(a), resistive voltage and current (b), energy (c), and resistance (d) for 2.3 kV discharge 13.

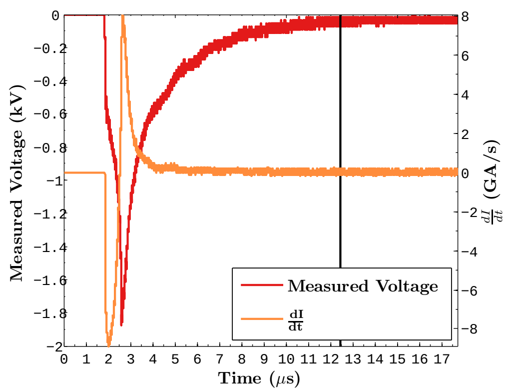

(a) Measured voltage and $\frac{dI}{dt}$ for discharge 14 (the vertical line marks the camera trigger)

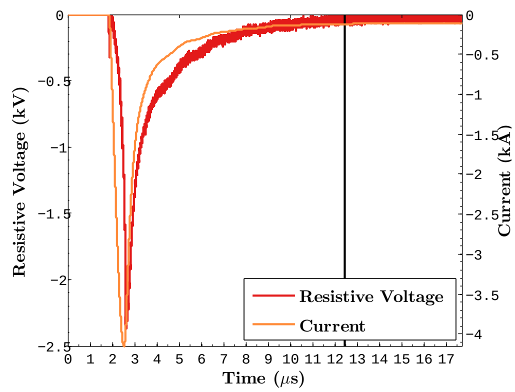

(b) Resistive voltage and current for discharge 14 (the vertical line marks the camera trigger)

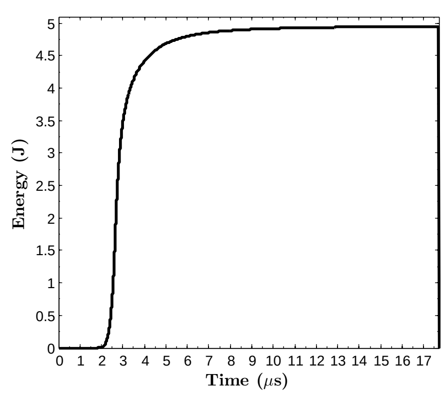

(c) Energy for discharge 14

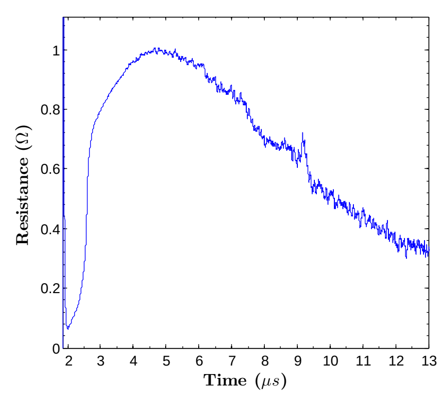

(d) Resistance for discharge 14

Figure 4.20: Measured voltage and $\frac{dI}{dt}$(a), resistive voltage and current (b), energy (c), and resistance (d) for 2.3 kV discharge 14.

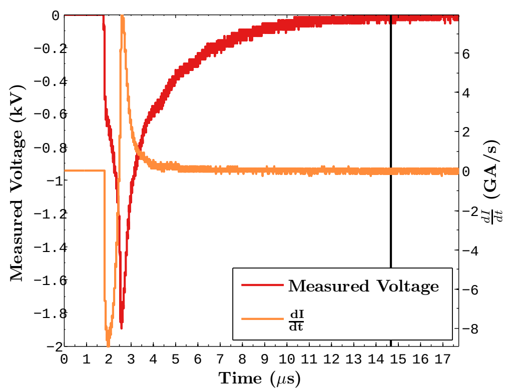

(a) Measured voltage and $\frac{dI}{dt}$ for discharge 15 (the vertical line marks the camera trigger)

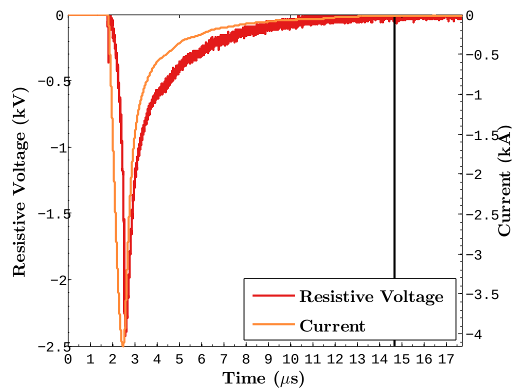

(b) Resistive voltage and current for discharge 15 (the vertical line marks the camera trigger)

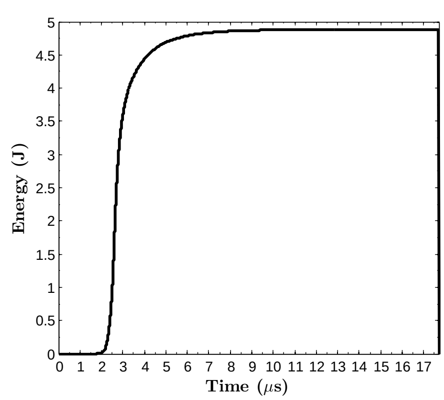

(c) Energy for discharge 15

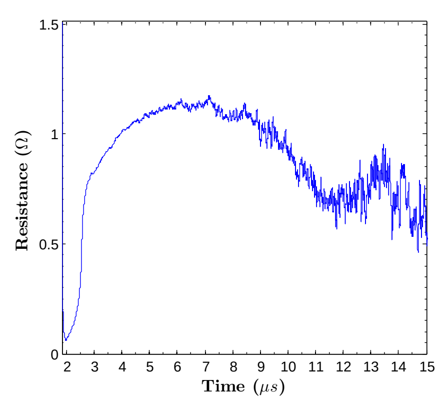

(d) Resistance for discharge 15

Figure 4.21: Measured voltage and $\frac{dI}{dt}$(a), resistive voltage and current (b), energy (c), and resistance (d) for 2.3 kV discharge 15.

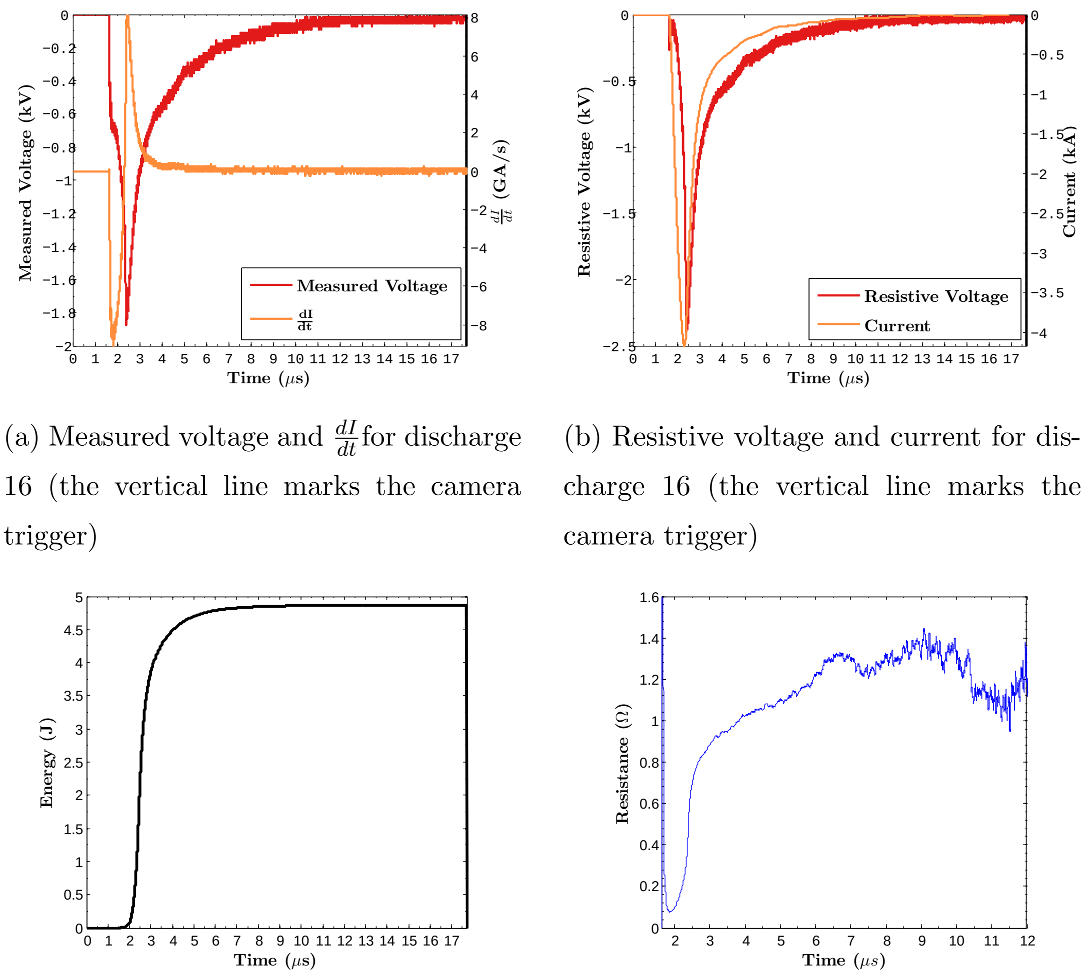

(a) Measured voltage and $\frac{dI}{dt}$ for discharge 16 (the vertical line marks the camera trigger)

(b) Resistive voltage and current for discharge 16 (the vertical line marks the camera trigger)

(c) Energy for discharge 16

(d) Resistance for discharge 16

Figure 4.22: Measured voltage and $\frac{dI}{dt}$(a), resistive voltage and current (b), energy (c), and resistance (d) for 2.3 kV discharge 16.

4.2.5 2.3kV Mechanism

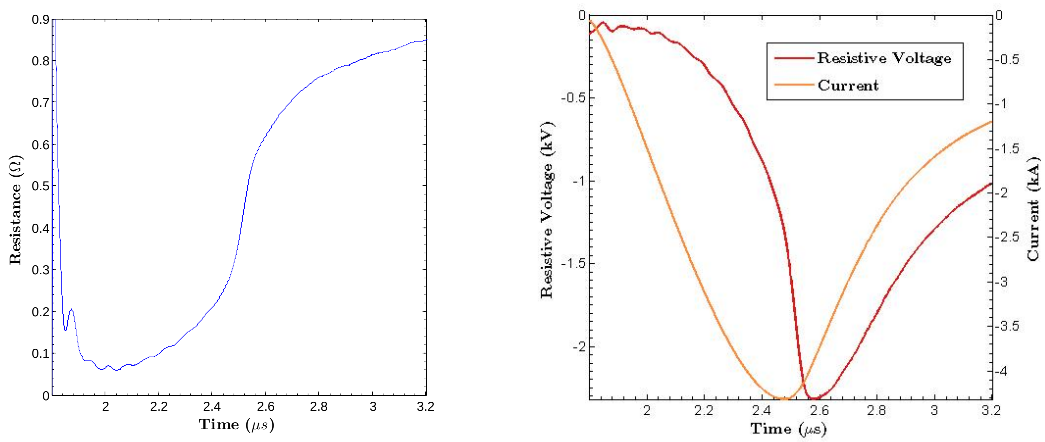

(a) Resistance (b) Voltage and current

Figure 4.23: Resistance (a), voltage, and current (b) around the peak current for the 2.3 kV discharge 1.

2.3 kV was specifically chosen due to this voltage being the threshold voltage at which there was no current pause observed. This was found by observing the difference between the charging voltage of the capacitor and the voltage during the dwell time of higher voltage discharges which closely matched approximately 2-3 kV. At this voltage the wire exhibited some unique behaviors. The lack of the current pause was due to the energy deposition-rate being low enough that the wire did not have a violent expansion. The wire remained approximately the same radius for the entire discharge (aside from some initial expansion to $2r_0$ before measurements were taken), and it would appear that the disintegration of the wire occurs after the capacitor has completely discharged. The lack of a current pause allowed the magnetic pressure to prevent further expansion after the initial heating. The energy deposition across the wire also appears to be mostly uniform. Additionally, the resistance remains very small (on the order of 1 Ω). The resistance does increase at the end of the trace for some of the explosions suggesting that the wire may start to disintegrate before complete discharge of the capacitor for some wires.

Figure 4.23 shows the resistance, voltage, and current during and around the current peak for discharge 1. It is of note that the change in resistance peaks at about the same time as the current peak. This would indicate that the high energy deposition is causing some kind of an expansion on a small level, possibly the initial expansion observed as all the images where taken after the current peak had occurred. This is most likely due to the high energy input from the sharp current rise before the peak due to extremely low resistance. The resistance plateau shortly after the current peak is most likely related to the fact that the expansion has stopped at this point in the explosion.

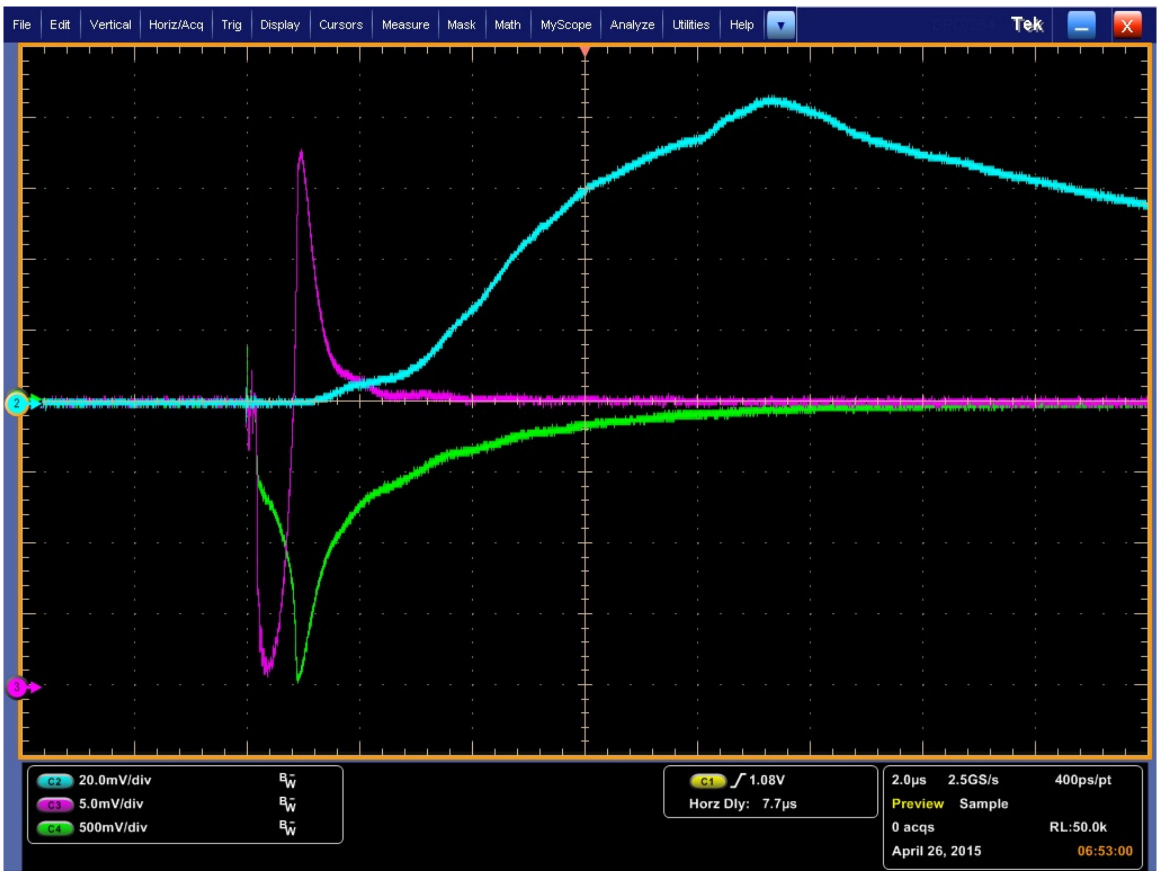

Figure 4.24: Voltage probe (green), rogowski coil (purple), and photodiode (blue) traces for a 2kV discharge

Traces recorded with a photo-diode are shown in figure 4.24. The intensity of light output has two peaks, one right after the current peak, and on well after the current peak and towards the end of the discharge. This suggests that the plasma most likely begins to form more fully towards the end of the discharge even though the majority of the energy deposition occurs early in the explosion.

Resistivity measurements show very small variations in the resistivity throughout the discharge. This is expected because the radius is assumed to remain constant, and the rise in resistance is too small to have a large impact.

Another observation made with the 2kV discharges is that the capillaries did not tend to explode. There were several that did shatter, but only partially and this is assumed to be from weak spots in the glass. This means that the shockwave from the plasma did not have enough energy to shatter the glass. A picture of an unshattered capillary from a 2kV discharge is shown in figure 4.25.

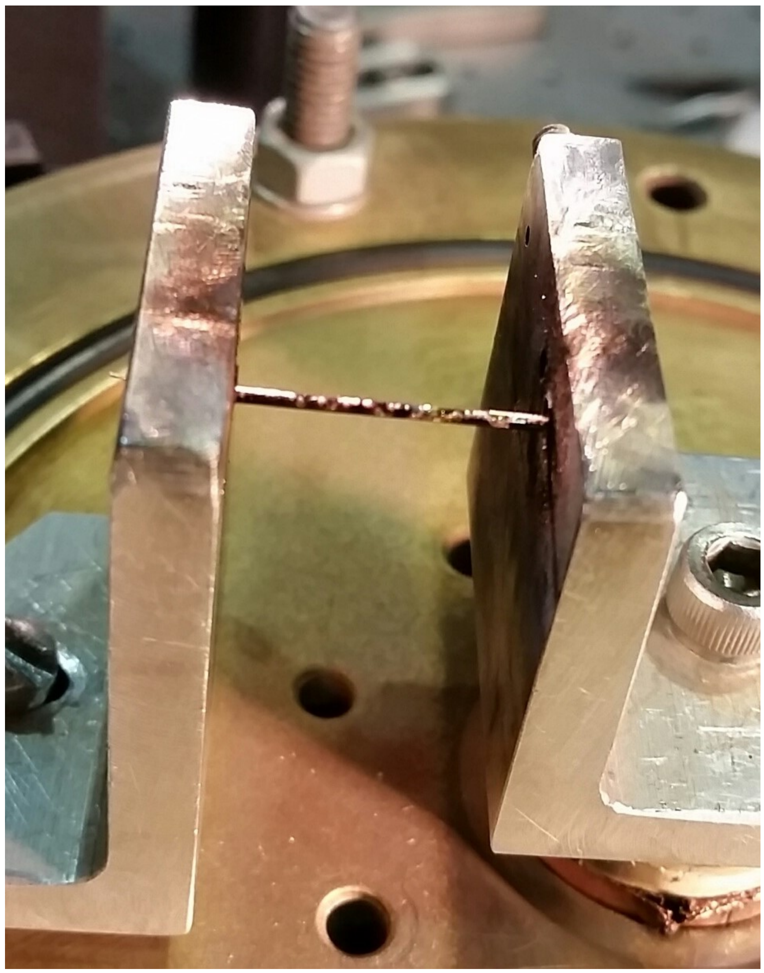

Figure 4.25: Unshattered capillary from a 2kV discharge. Note the aluminum coating on the inside of the capillary.

4.3 7 kV Discharge

4.3.1 Radius

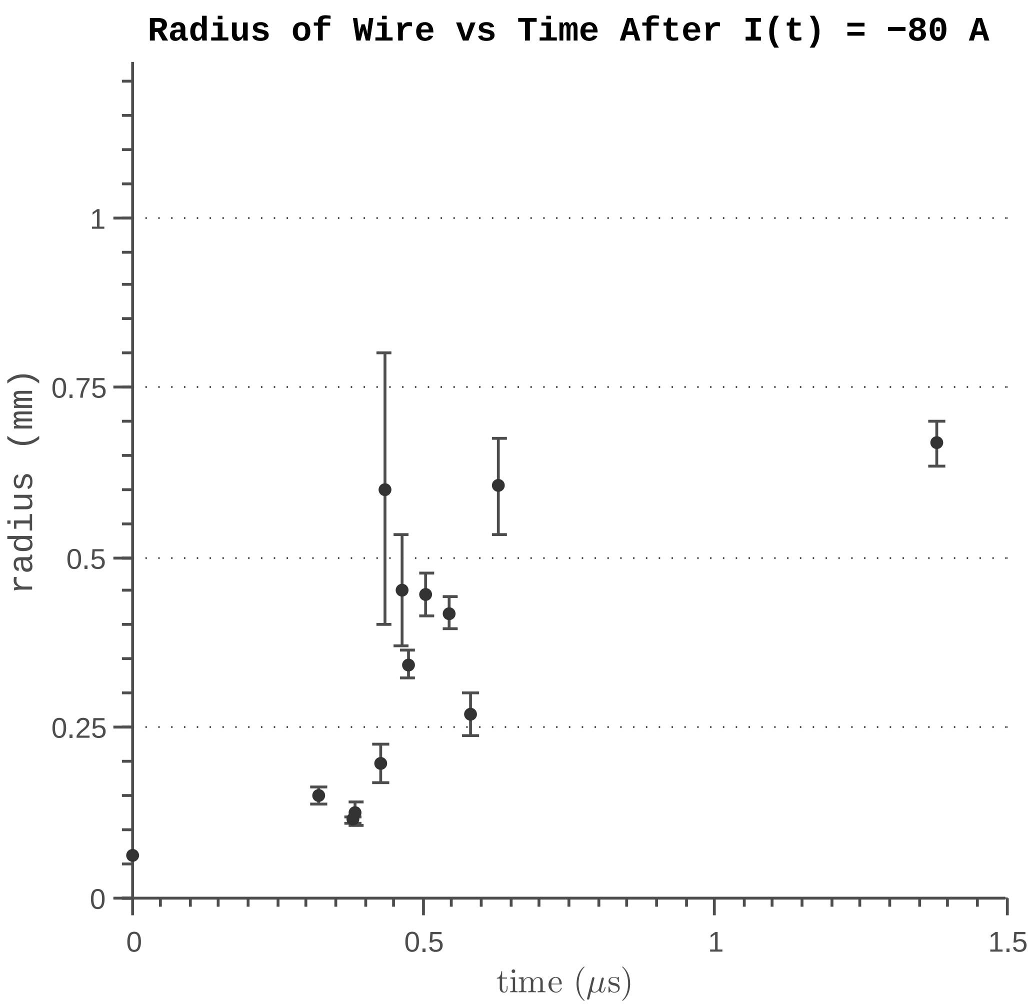

Figure 4.26: Radius vs. Time Taken From All 7 kV Discharges

4.3.2 Resistivity

Figure 4.27 shows the full data set, and figure 4.28 shows the data for the first 600ns of the discharge.

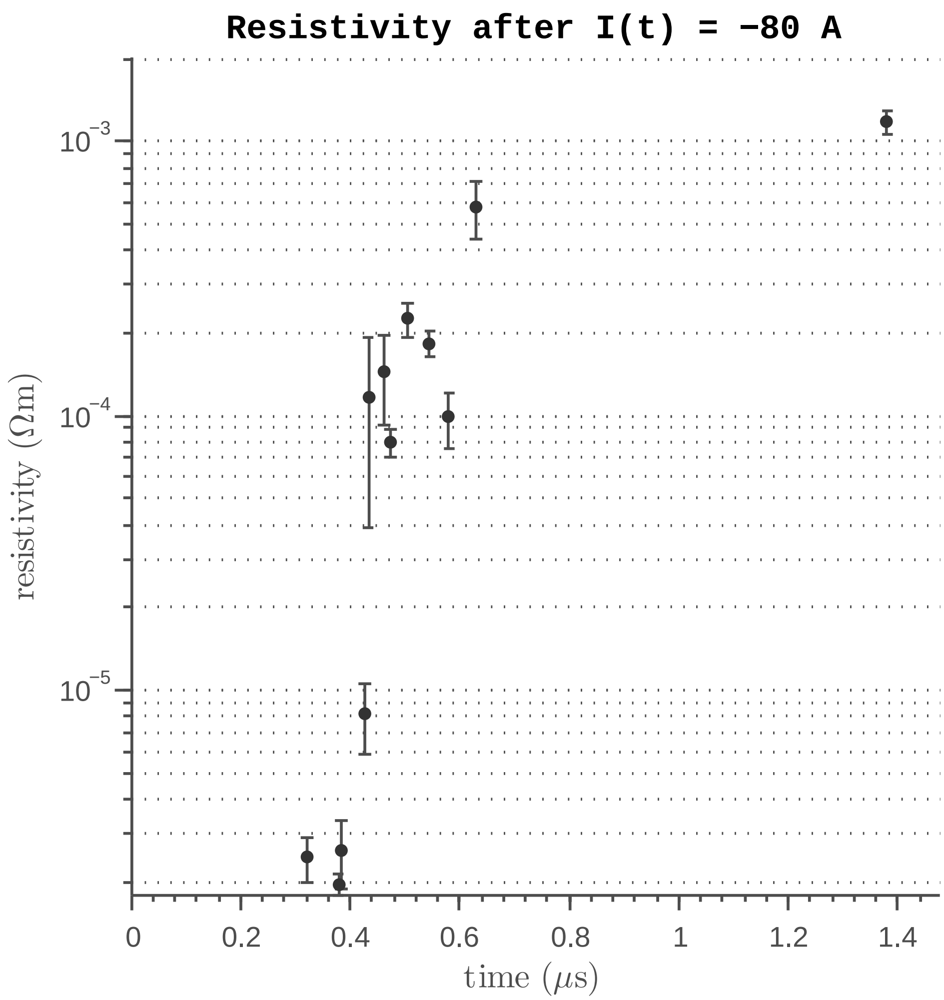

Figure 4.27: Plot of resistivity measurements for the full 7 kV discharges

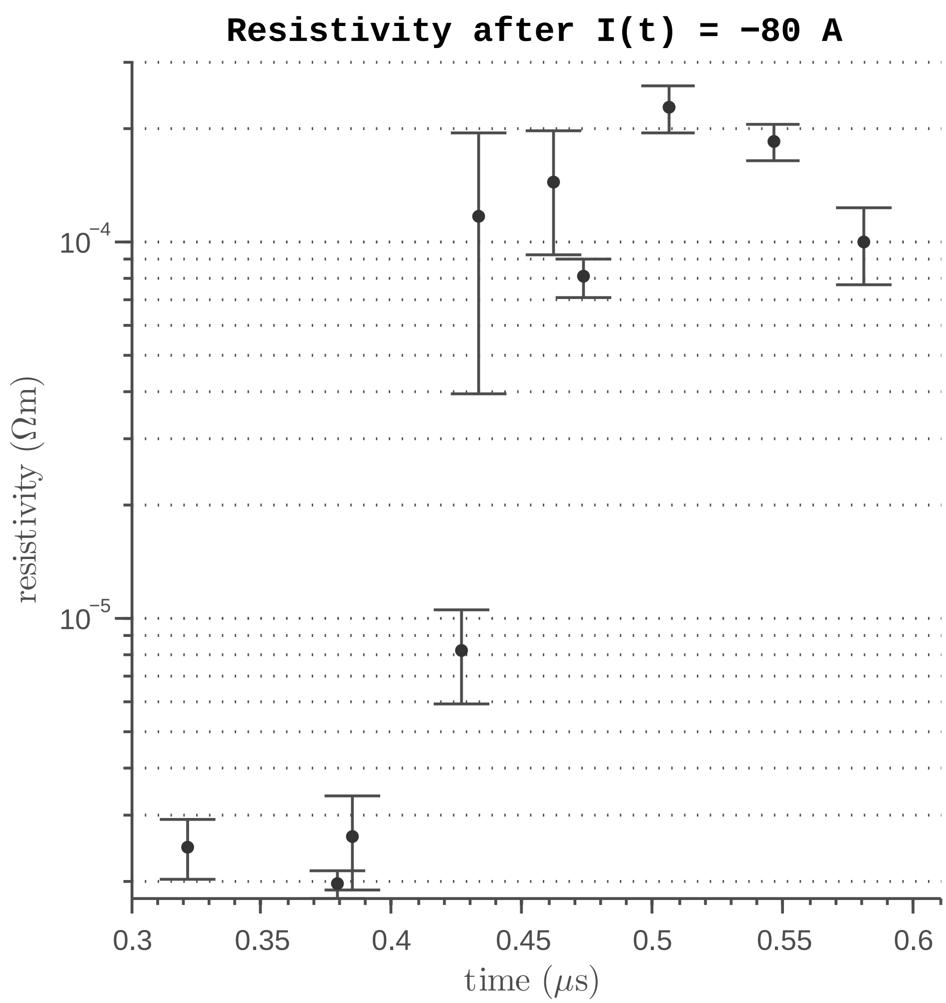

Figure 4.28: Resistivity measurements for the first 600 ns of the 7 kV discharge

4.3.3 Discharge Images

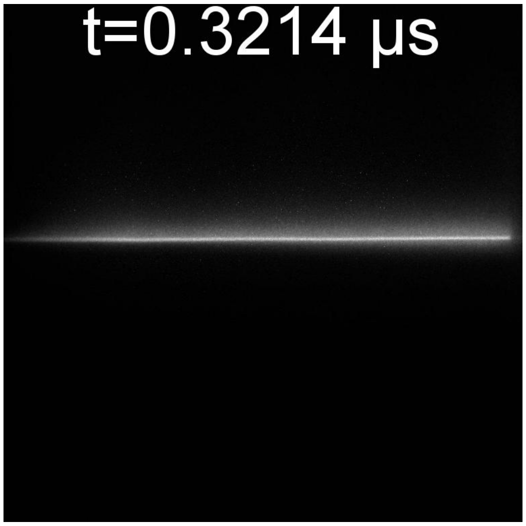

(a) Discharge 1

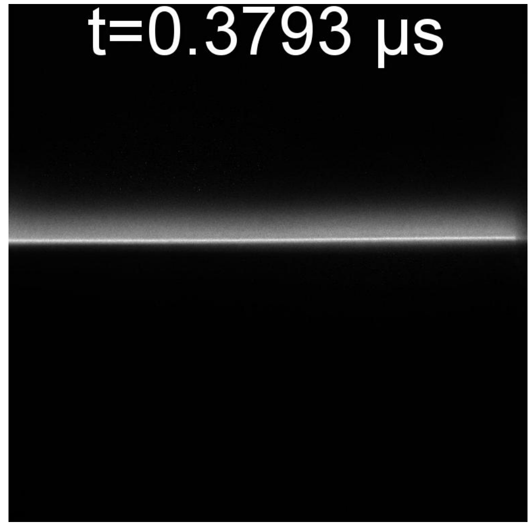

(b) Discharge 2

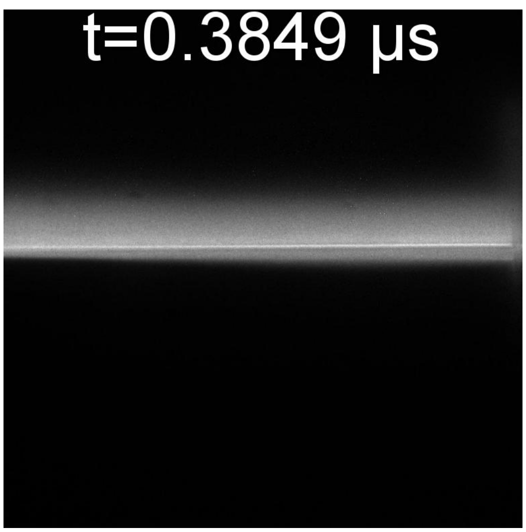

(c) Discharge 3

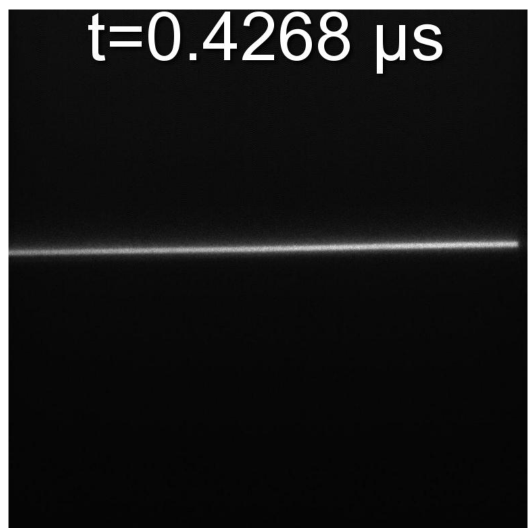

(d) Discharge 4

Figure 4.29: ICCD images of 7 kV discharges 1-4

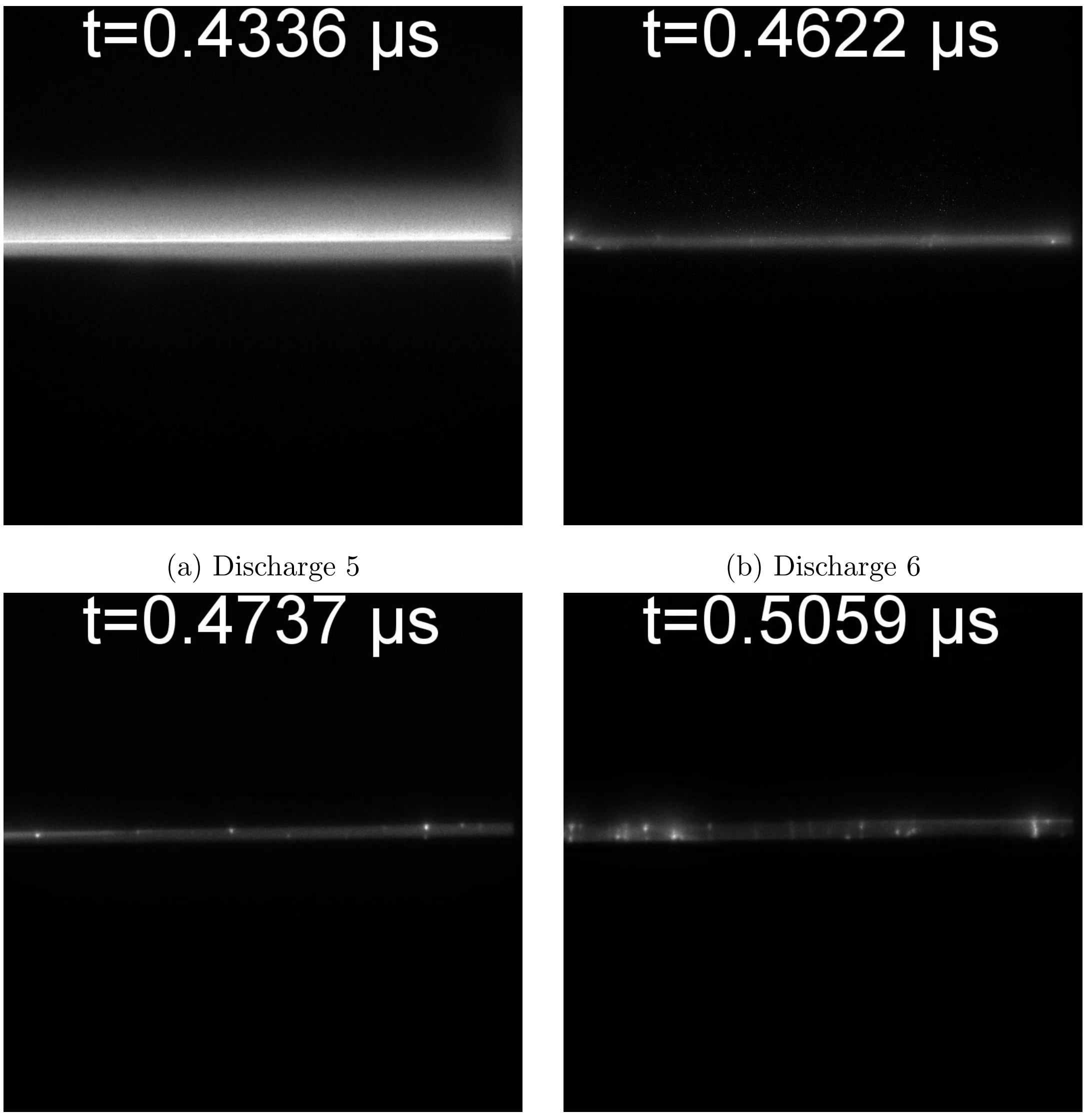

(a) Discharge 5

(b) Discharge 6

(c) Discharge 7

(d) Discharge 8

Figure 4.30: ICCD images of 7 kV discharges 5-8

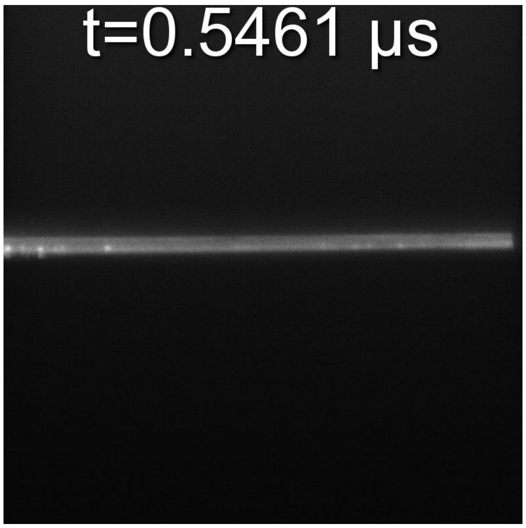

(a) Discharge 9

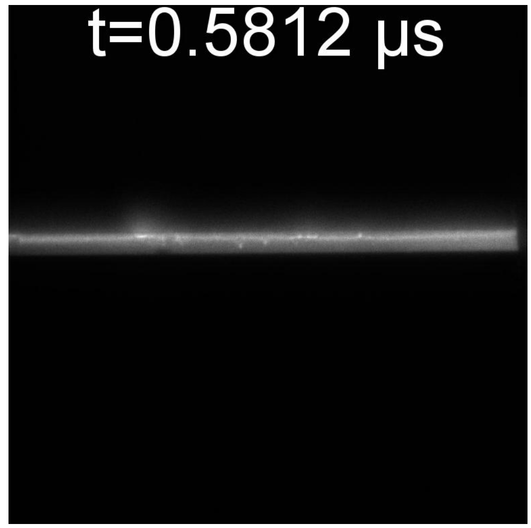

(b) Discharge 10

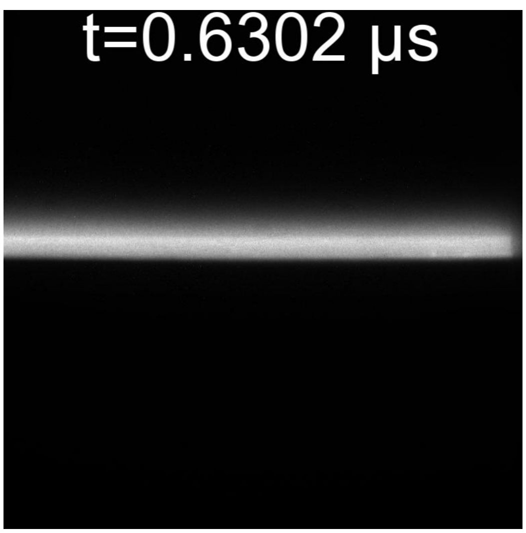

(c) Discharge 11

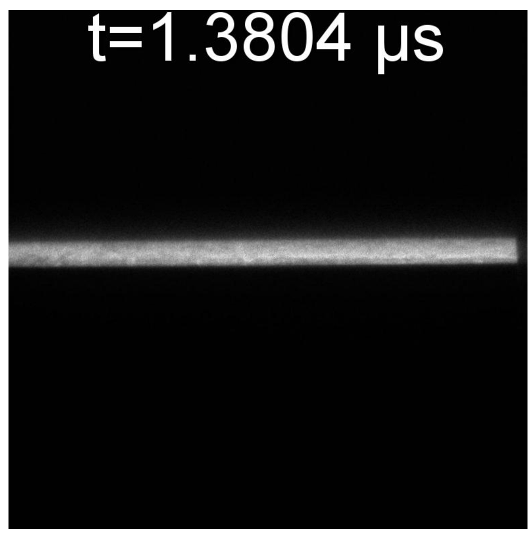

(d) Discharge 12

Figure 4.31: ICCD images of 7 kV discharges 9-12

4.3.4 Current, Voltage, Energy, and Resistance

While the camera trigger time may be the same for multiple discharges, it represents a different time in the explosion. This is due to the jitter from the electronics causing a different delay of each discharge.

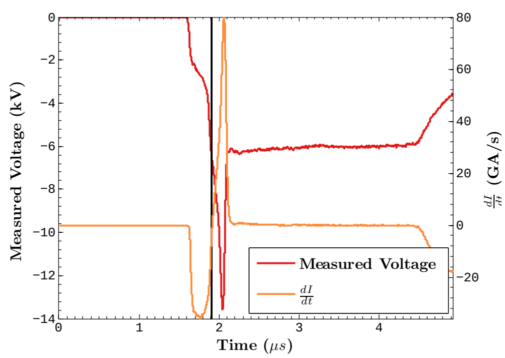

(a) Measured voltage and $\frac{dI}{dt}$for discharge 1 (the vertical line marks the camera trigger)

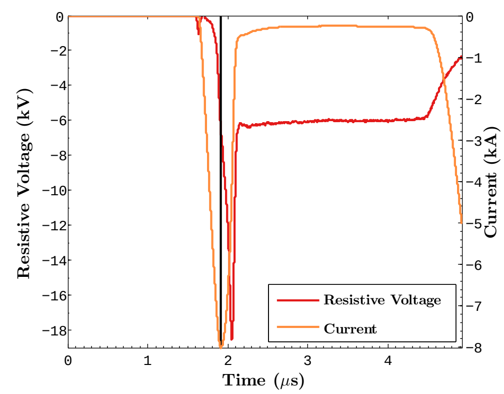

(b) Resistive voltage and current for discharge 1 (the vertical line marks the camera trigger)

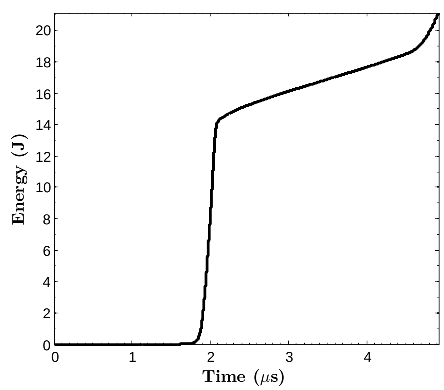

(c) Energy for discharge 1

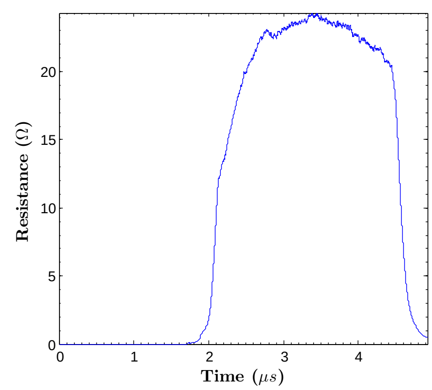

(d) Resistance for discharge 1

Figure 4.32: Measured voltage and $\frac{dI}{dt}$(a), resistive voltage and current (b), energy (c), and resistance (d) for 7 kV discharge 1.

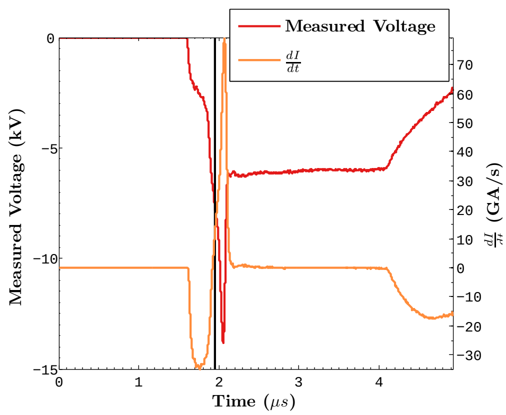

(a) Measured voltage and $\frac{dI}{dt}$ for discharge 2 (the vertical line marks the camera trigger)

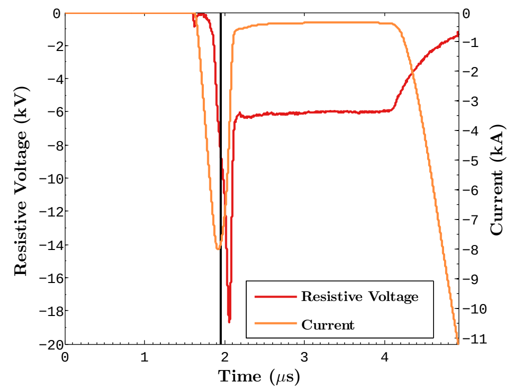

(b) Resistive voltage and current for discharge 2 (the vertical line marks the camera trigger)

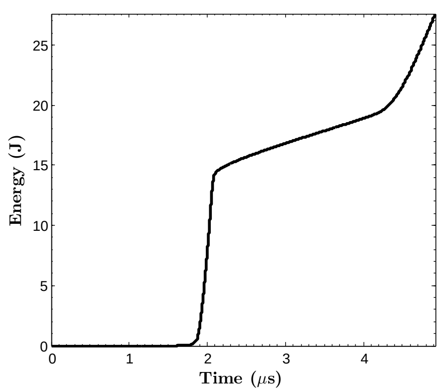

(c) Energy for discharge 2

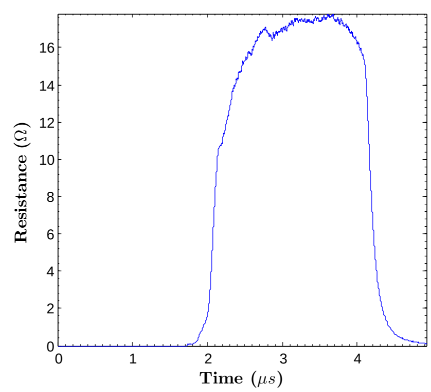

(d) Resistance for discharge 2

Figure 4.33: Measured voltage and $\frac{dI}{dt}$(a), resistive voltage and current (b), energy (c), and resistance (d) for 7 kV discharge 2.

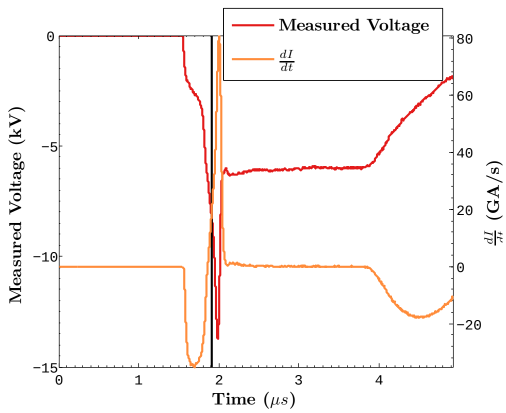

(a) Measured voltage and $\frac{dI}{dt}$ for discharge 3 (the vertical line marks the camera trigger)

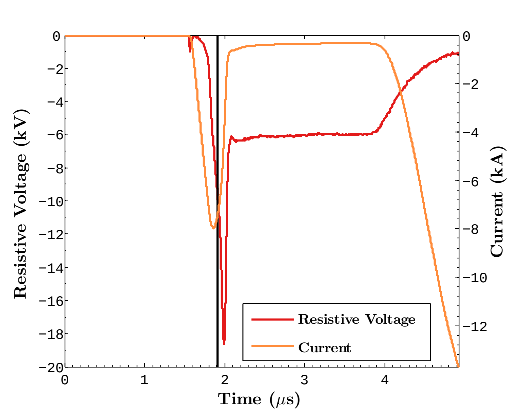

(b) Resistive voltage and current for discharge 3 (the vertical line marks the camera trigger)

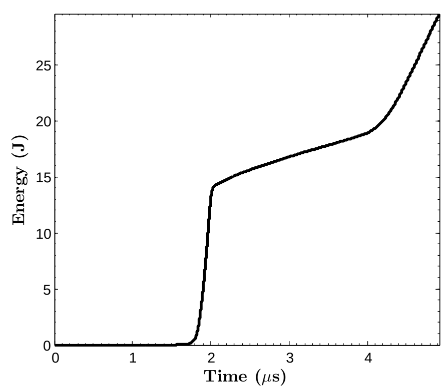

(c) Energy for discharge 3

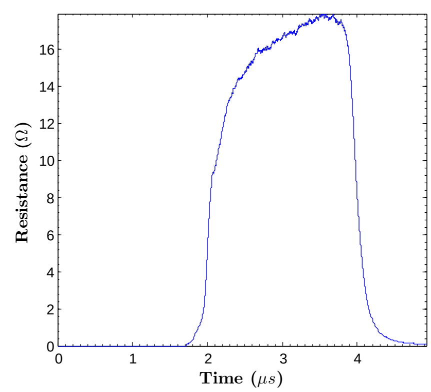

(d) Resistance for discharge 3

Figure 4.34: Measured voltage and $\frac{dI}{dt}$(a), resistive voltage and current (b), energy (c), and resistance (d) for 7 kV discharge 3.

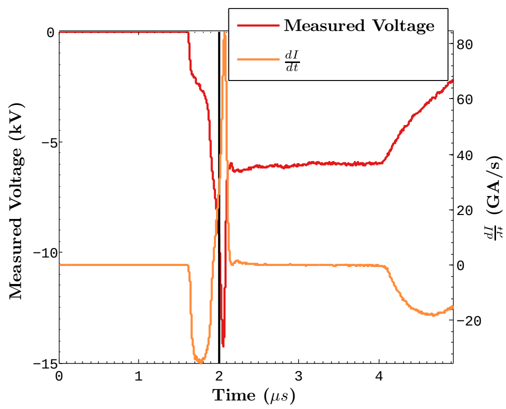

(a) Measured voltage and $\frac{dI}{dt}$ for discharge 4 (the vertical line marks the camera trigger)

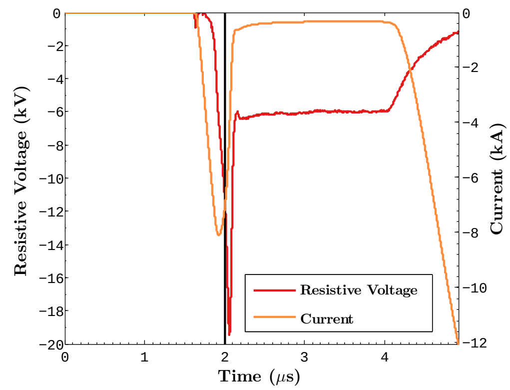

(b) Resistive voltage and current for discharge 4 (the vertical line marks the camera trigger)

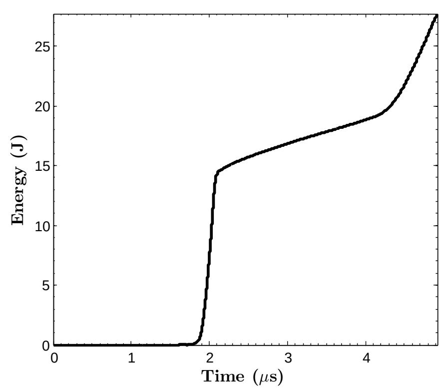

(c) Energy for discharge 4

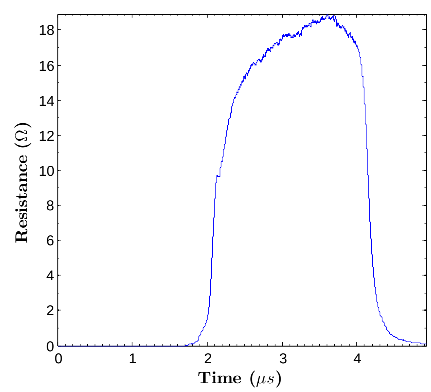

(d) Resistance for discharge 4

Figure 4.35: Measured voltage and $\frac{dI}{dt}$(a), resistive voltage and current (b), energy (c), and resistance (d) for 7 kV discharge 4.

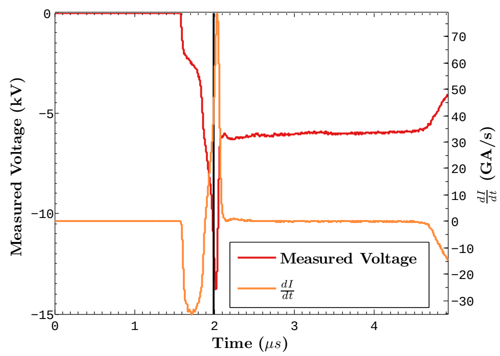

(a) Measured voltage and $\frac{dI}{dt}$ for discharge 5 (the vertical line marks the camera trigger)

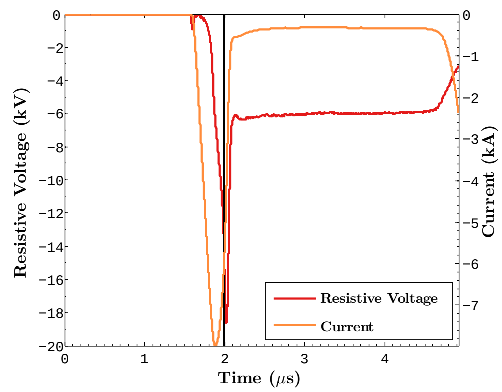

(b) Resistive voltage and current for discharge 5 (the vertical line marks the camera trigger)

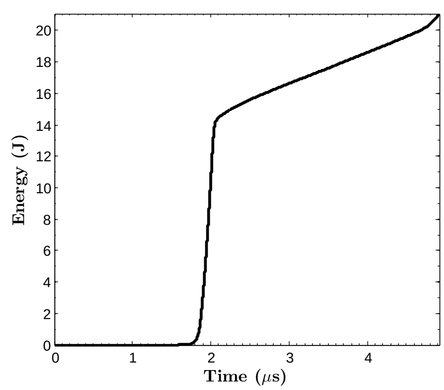

(c) Energy for discharge 5

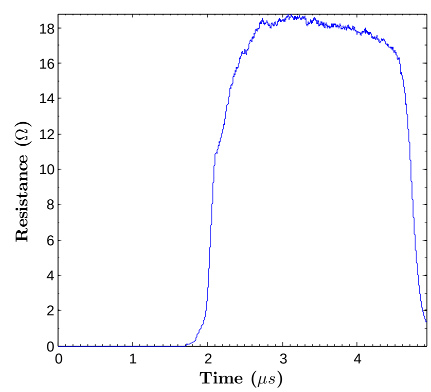

(d) Resistance for discharge 5

Figure 4.36: Measured voltage and $\frac{dI}{dt}$(a), resistive voltage and current (b), energy (c), and resistance (d) for 7 kV discharge 5.

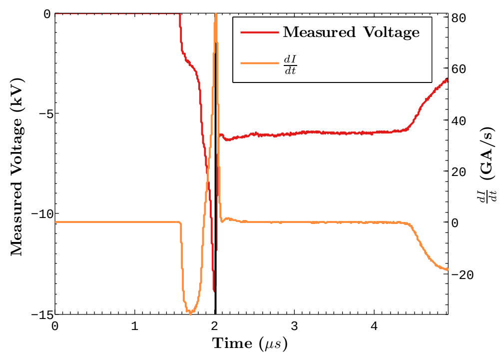

(a) Measured voltage and $\frac{dI}{dt}$ for discharge 6 (the vertical line marks the camera trigger)

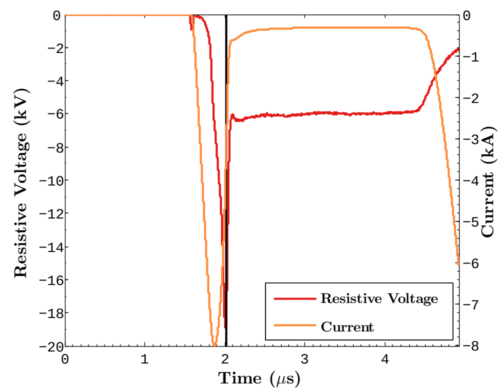

(b) Resistive voltage and current for discharge 6 (the vertical line marks the camera trigger)

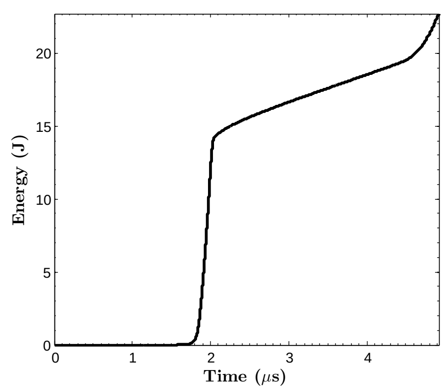

(c) Energy for discharge 6

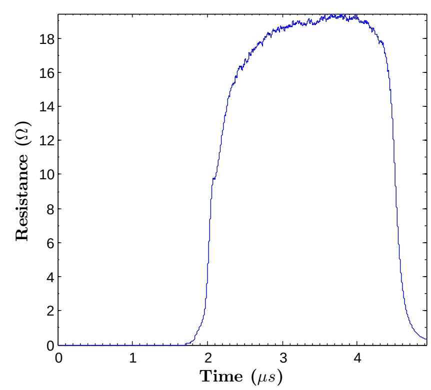

(d) Resistance for discharge 6

Figure 4.37: Measured voltage and $\frac{dI}{dt}$(a), resistive voltage and current (b), energy (c), and resistance (d) for 7 kV discharge 6.

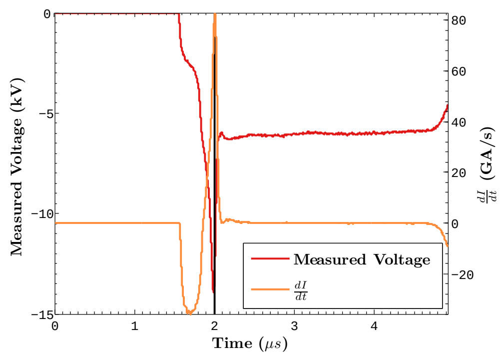

(a) Measured voltage and $\frac{dI}{dt}$ for discharge 7 (the vertical line marks the camera trigger)

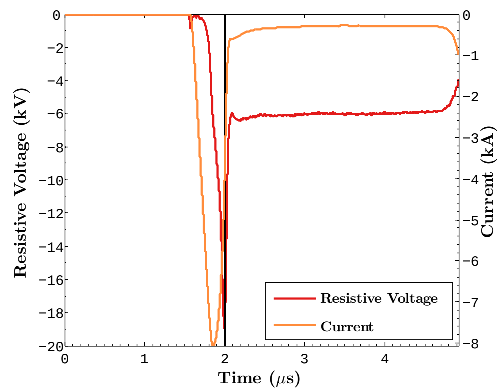

(b) Resistive voltage and current for discharge 7 (the vertical line marks the camera trigger)

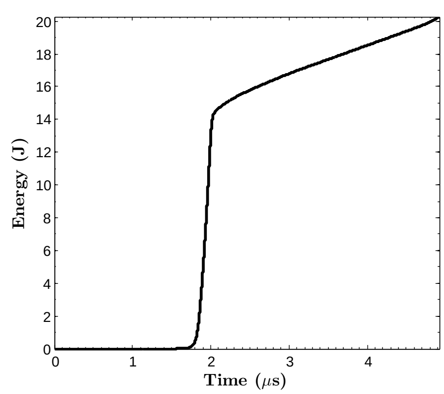

(c) Energy for discharge 7

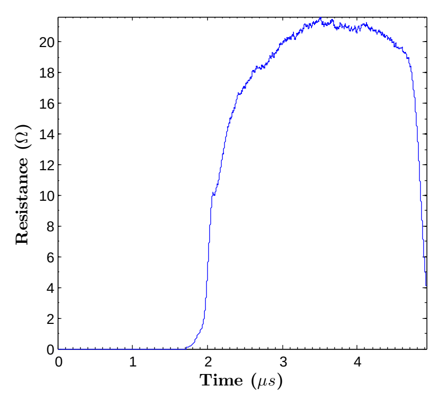

(d) Resistance for discharge 7

Figure 4.38: Measured voltage and $\frac{dI}{dt}$(a), resistive voltage and current (b), energy (c), and resistance (d) for 7 kV discharge 7.

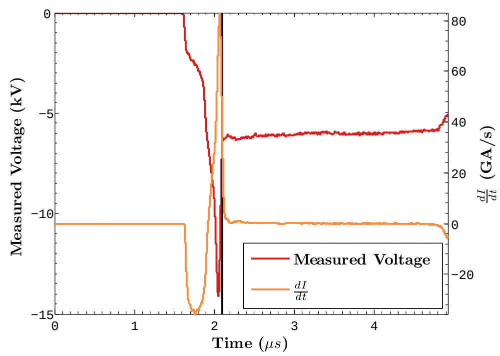

(a) Measured voltage and $\frac{dI}{dt}$ for discharge 8 (the vertical line marks the camera trigger)

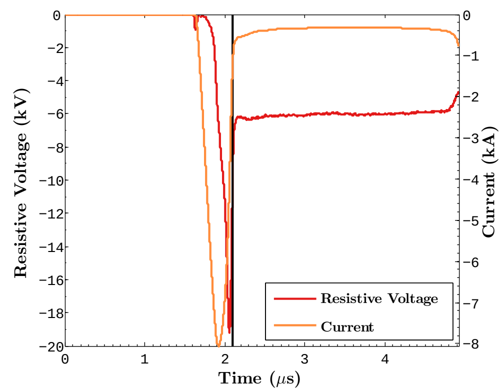

(b) Resistive voltage and current for discharge 8 (the vertical line marks the camera trigger)

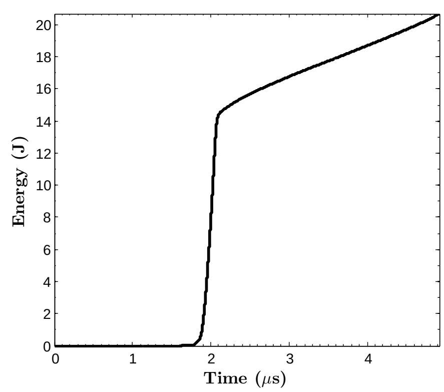

(c) Energy for discharge 8

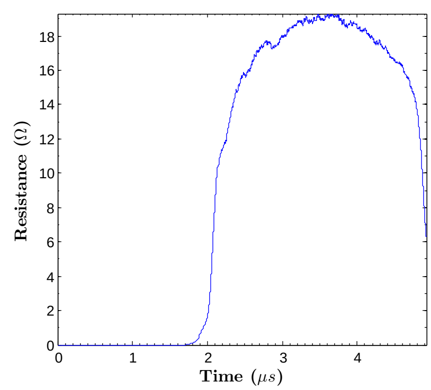

(d) Resistance for discharge 8

Figure 4.39: Measured voltage and $\frac{dI}{dt}$(a), resistive voltage and current (b), energy (c), and resistance (d) for 7 kV discharge 8.

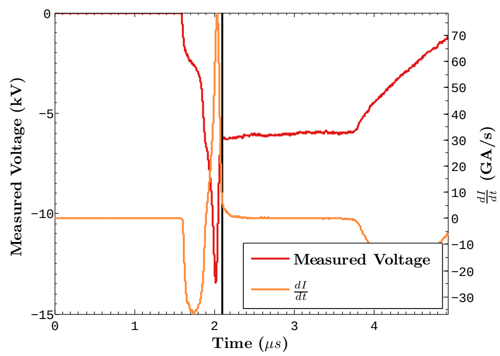

(a) Measured voltage and $\frac{dI}{dt}$ for discharge 9 (the vertical line marks the camera trigger)

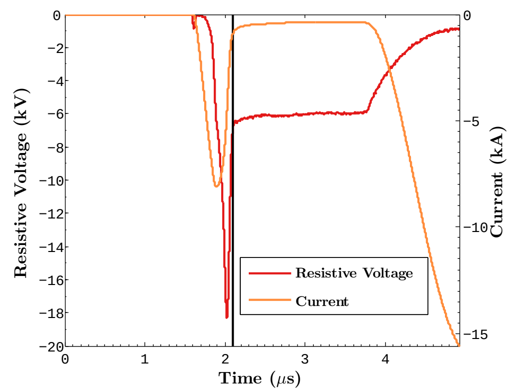

(b) Resistive voltage and current for discharge 9 (the vertical line marks the camera trigger)

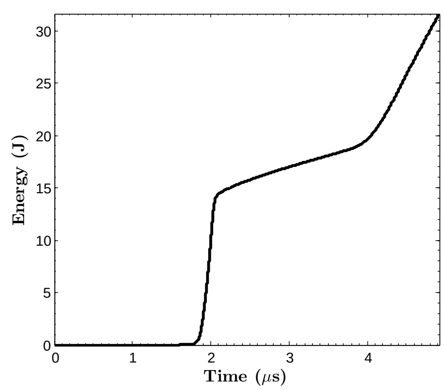

(c) Energy for discharge 9

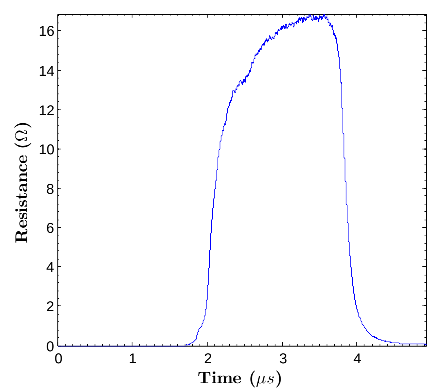

(d) Resistance for discharge 9

Figure 4.40: Measured voltage and $\frac{dI}{dt}$(a), resistive voltage and current (b), energy (c), and resistance (d) for 7 kV discharge 9.

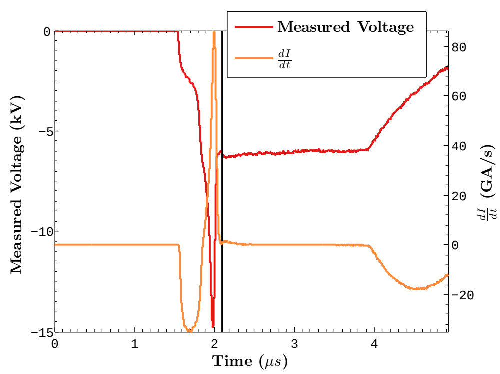

(a) Measured voltage and $\frac{dI}{dt}$ for discharge 10 (the vertical line marks the camera trigger)

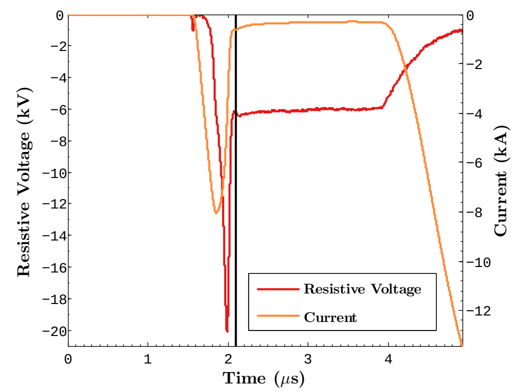

(b) Resistive voltage and current for discharge 10 (the vertical line marks the camera trigger)

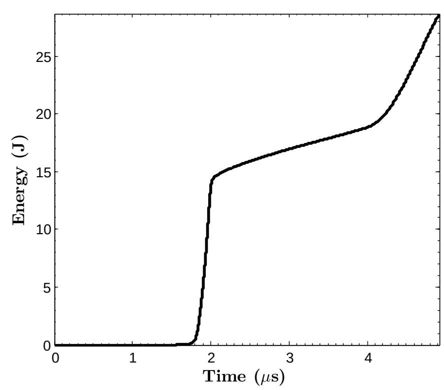

(c) Energy for discharge 10

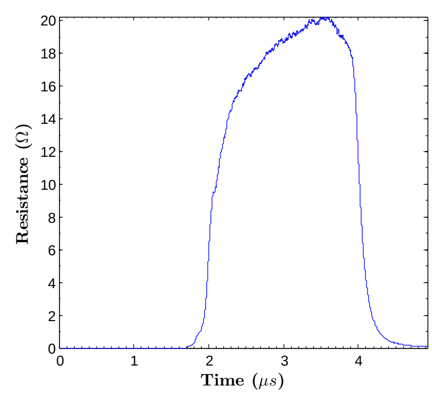

(d) Resistance for discharge 10

Figure 4.41: Measured voltage and $\frac{dI}{dt}$(a), resistive voltage and current (b), energy (c), and resistance (d) for 7 kV discharge 10.

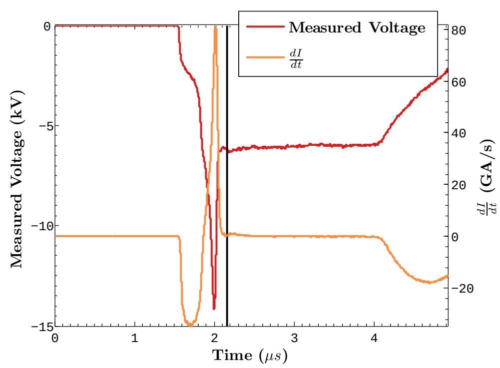

(a) Measured voltage and $\frac{dI}{dt}$ for discharge 11 (the vertical line marks the camera trigger)

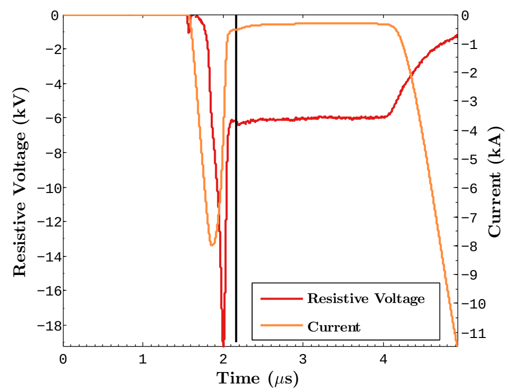

(b) Resistive voltage and current for discharge 11 (the vertical line marks the camera trigger)

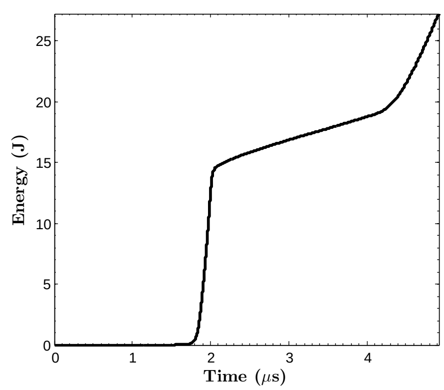

(c) Energy for discharge 11

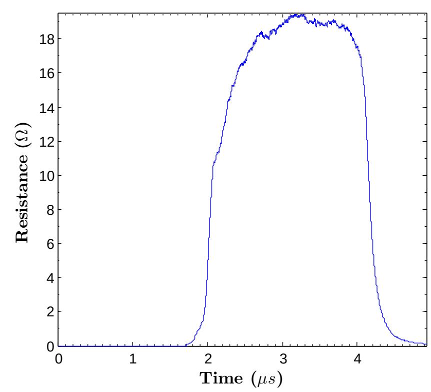

(d) Resistance for discharge 11

Figure 4.42: Measured voltage and $\frac{dI}{dt}$(a), resistive voltage and current (b), energy (c), and resistance (d) for 7 kV discharge 11.

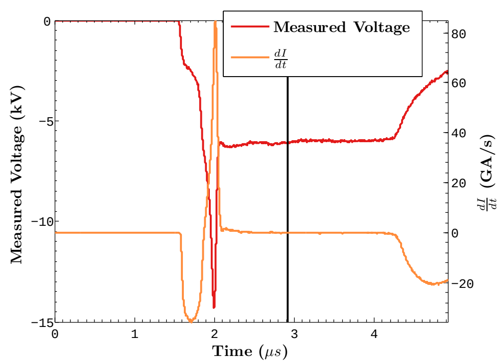

(a) Measured voltage and $\frac{dI}{dt}$ for discharge 12 (the vertical line marks the camera trigger)

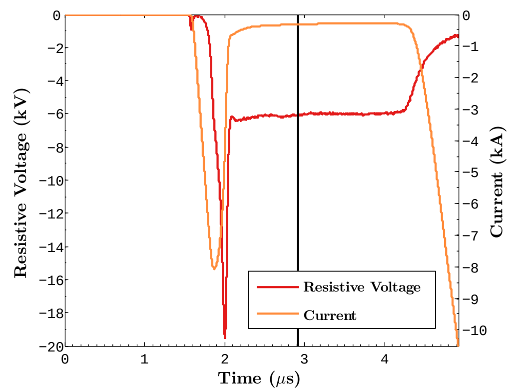

(b) Resistive voltage and current for discharge 12 (the vertical line marks the camera trigger)

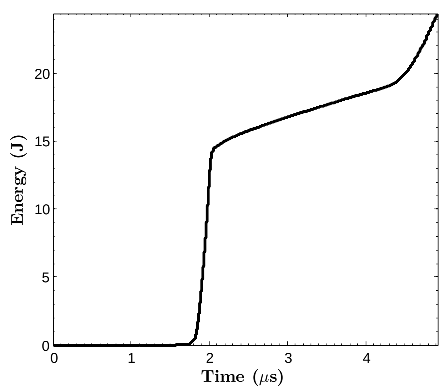

(c) Energy for discharge 12

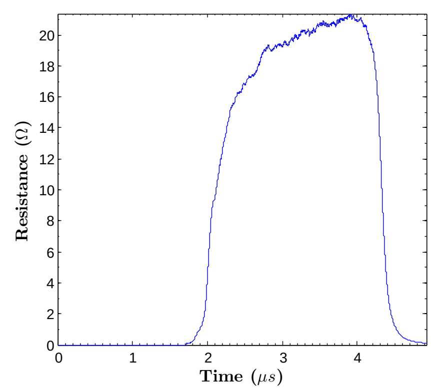

(d) Resistance for discharge 12

Figure 4.43: Measured voltage and $\frac{dI}{dt}$(a), resistive voltage and current (b), energy (c), and resistance (d) for 7 kV discharge 12.

4.3.5 7 kV Mechanism

Initial Heating

As expected, the behavior at 7kV is much different from that at 2kV due to the larger current peaks and faster energy-input rate. The resistance, however, has a very distinct behavior around the peak of the current. Figure 4.44a is zoomed in on the time around the peak. There are three distinct regions in the resistance. The first is about 10ns before the current peak which is a small rise, and then a quasi-linear increase until about 100ns after the peak current which then rises sharply. The final region is the a plateau feature of the resistance when the wire has formed an insulator indicating the beginning of the dwell time.

Associated with this resistance behavior is a similar trend seen in the voltage (4.44b). There is a sharp rise in voltage about 10ns before the current peak, then a quasi-linear increase until about 100ns after the peak where the voltage rises sharply and peaks leading into the current pause.

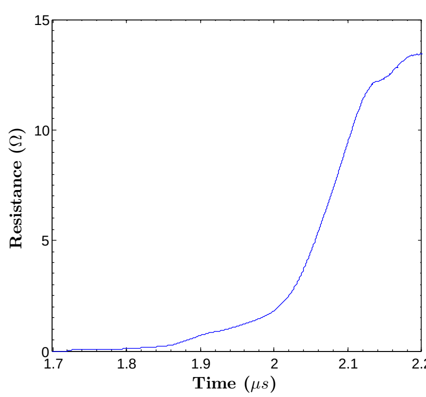

(a) Resistance

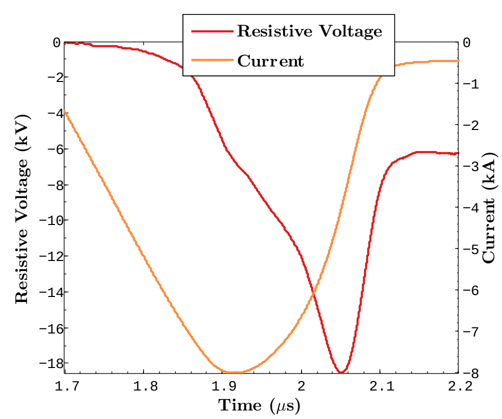

(b) Voltage and current

Figure 4.44: Resistance (a), voltage, and current (b) around the peak current for the 7kV discharge 1.

While an initial guess for this behavior was the possible timing of when the capillary burst, the same behavior is seen in other tests without a capillary. A good assumption would be the behavior changes indicate a change of state, the first "sharp" rise being a solid to liquid phase change about 10ns before the current peak. The second sharp rise would indicate a change of state from liquid to vapor, which is why the current pause occurs shortly after as the vapor expands and becomes an insulator similar to what is seen by Taylor [38] and Sasaki [29]. It should be noted however that their wire had smaller diameter, shorter length, and their containment medium was a strong plastic capillary and water respectively. Although similar trends can be seen, we would not expect to see the same behavior between these two systems and our system.

The radial expansion of this system has a sharp rise about 400 ns into the initial discharge. This is just after the current peak and occurs right around the phase transition into a vapor. The radius appears to peak shortly after, and even decrease as it reaches the current pause stage. This may be due to pressure from the capillary after rapid expansion. The last two data points for images 11 and 12 do not appear to follow the trend of earlier data, but there is not sufficient data in that time range to make any conclusions.

The resistivity behavior matches both that of the resistance and the radius. A sharp increase is observed around 400 ns after the start of the discharge. The same plateau around 500 ns and preceding decrease is seen in the resistivity as was seen in the radius. At this same time the resistance begins to plateau as well. While this decrease in resistivity and radius is seen right around the beginning of the current pause, there may be significant expansion later in the dwell time. More data needs to be collected to understand the behavior of the system during this time.

Something to note is that the maximum voltage across the electrodes at the start of the capacitor discharge was higher than the charging voltage. However, identical peak voltage values and traces across the electrodes were also recorded with a high voltage probe and were in agreement with the traces recorded with the capacitive voltage divider. It is well known that when charging a capacitor with an inductor is series, the voltage stored in the capacitor can be higher than the supply voltage. This is due to the fact that a series inductor limits the current drawn from the supply and causes the capacitor to charge to almost twice the supply voltage. Tests performed with the 0.001 Ω shunt resistor show as expected voltage values lower than the charging voltage. In addition, direct measurements of various charging voltages after disconnecting the power supply show identical voltages as those delivered by the power supply. We are still investigating this unexpected phenomenon but we are confident from the current, voltage and dI/dt traces that this effect is related to the inductive component of the wire at the beginning of the discharge.

Dwell Time

The dwell time or current pause occurs approximately 200ns after the current peak has been reached, and approximately 500ns after the discharge occurs. At this point the wire has changed to a vapor state, and expanded enough to become an insulator. As can be seen from figure 4.26 the majority of the expansion happens just before and at the start of the current pause. While it would be expected that a further expansion would occur during the dwell time, the capillary most likely contains the plasma if it does not shatter before this time. From the images, it appears the the capillary may still be intact at this point in the explosion, and continuing to contain the plasma pressure.

The dwell time also should not be mistaken for an actual zero current pause. Resistance in the wire does increase significantly to about 20 Ω, but a small amount of current (about -500A) does leak through during this time. This current leak allows for a small amount of magnetic field which may be the cause of the helical ion channels observed in figure 4.30d and studied by Vlastos [30]. Before the plasma begins to heat, one can observe in figures 4.30b, 4.30c, 4.30d, 4.31a, and 4.31b the small bright spots that appear. These may be an indication of the ion channels already starting to develop on the outer surface of the wire. The helical pattern observed may be a result of the wire being twisted, but it very well could also be the result of ions following the force field lines caused by the electric and magnetic fields.

The dwell times remained fairly consistent between discharges lasting approximately 2 μs. Differences in the dwell times are most likely affected by imperfections in the wire causing instabilities to develop at different times and places in the wire.

Restrike

This study did not investigate the restrike mechanism of the exploding wires, as it focused primarily on the first stages and phase changes in the wire. However as stated earlier, it seems that at this voltage the restrike occurs due to ion channels developing on the outside of the wire as discussed previously.

Capillary

The capillary had a significant effect on the mechanism of the exploding wire. It serves to contain the plasma and prevent pressure from dropping due to expansion of the outer layers of melted/vaporized wire. An image of the same aluminum wire discharged at 8kV without a capillary is seen in figure 4.45. The timing for this image taken is comparable to that of image 12. The difference is significant, and confirms the theory that capillaries can act to contain the plasma pressure during an explosion.

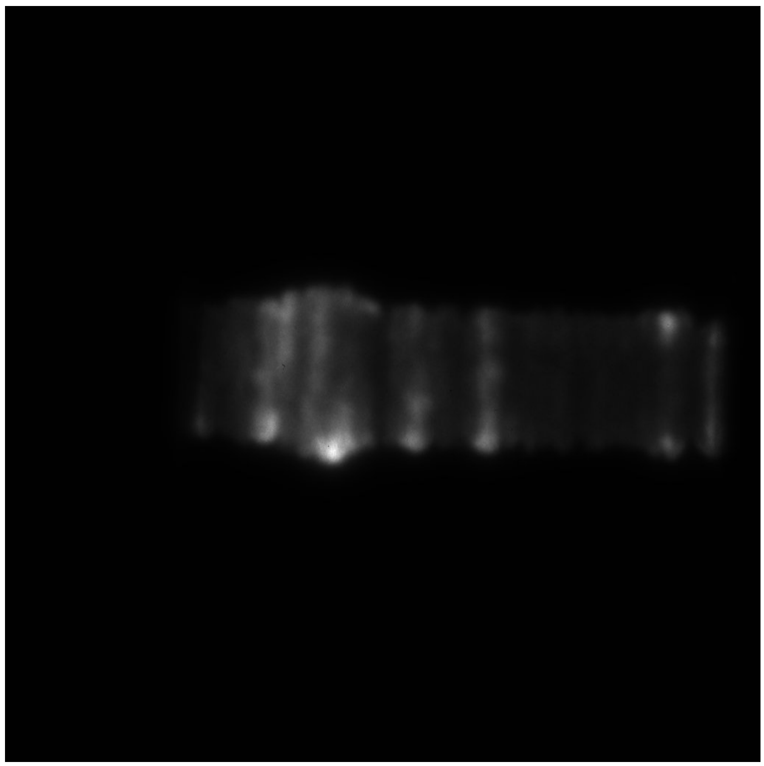

Figure 4.45: Image of Al wire exploded in air (no capillary) with a charging voltage of 8kV 1.5 μs after initial discharge.

4.4 Copper Wire Experiments

In addition to conducting experiments with aluminum, experiments were also conducted on 80 micron diameter copper wires. Just as was done with Aluminum, several voltages were tested until the voltage at which no dwell time occurs was found.

Images were also recorded of these explosions. Figure 4.46 shows a sample image of a copper wire explosion image as well as the current and voltage traces.

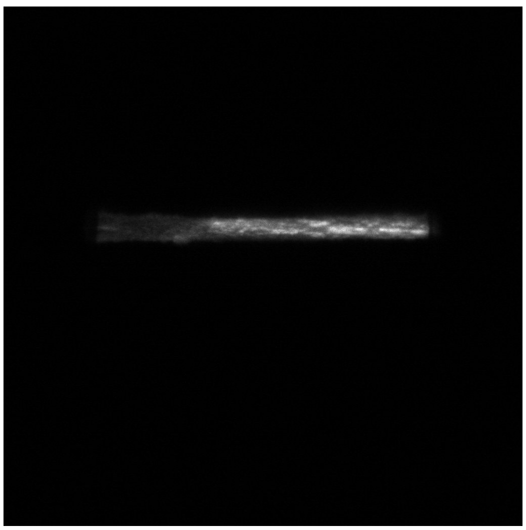

(a) Image of exploding copper wire

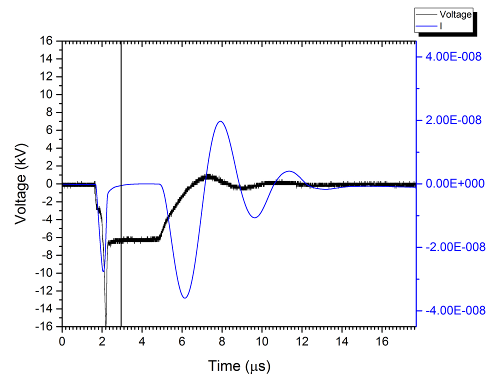

(b) Voltage and current traces of exploding Cu wire (vertical line indicates camera trigger).

Figure 4.46: Sample voltage and current traces with corresponding image of exploding Cu wire with a charging voltage of 8kV.

4.5 Laser Interferometry

A Mach-Zender interferometer was constructed for the purpose of obtaining the electron density of the plasma. The laser used had a 5 ns pulse width, which was aligned with the plasma plume. It was necessary to measure to plasma plume due the the presence of the capillary around the wire itself. A CCD was used to capture the image by integrating over the entire pulse width. Fringes in air of the interferometer are shown in figure 4.47. Because of the large pulse width of the laser, the resolution of the inteferometry measurements was poor. Figure 4.48 shows the signals recorded by a photodiode (blue trace) placed close to the capacitor as well as the resulting change in fringe patterns observed. The short spike in the photodiode trace shows the laser pulse, while the broader peaks are a result of the discharge emissions. In an attempt to gain better resolution, the ICCD was used with a gate width of 2 ns, but due to the jitter between the timing of the laser trigger and the camera trigger, no images were able to be obtained. It should be noted that even with this width of 2 ns, the resolution would most likely be poor.

Other exploding wire interferometry experiments have been conducted with a laser with a 150 ps pulse width [37]. While we have a laser with a pulse width of 200 ps, the laser was under maintenance and unable to be used at the time of the experiments.

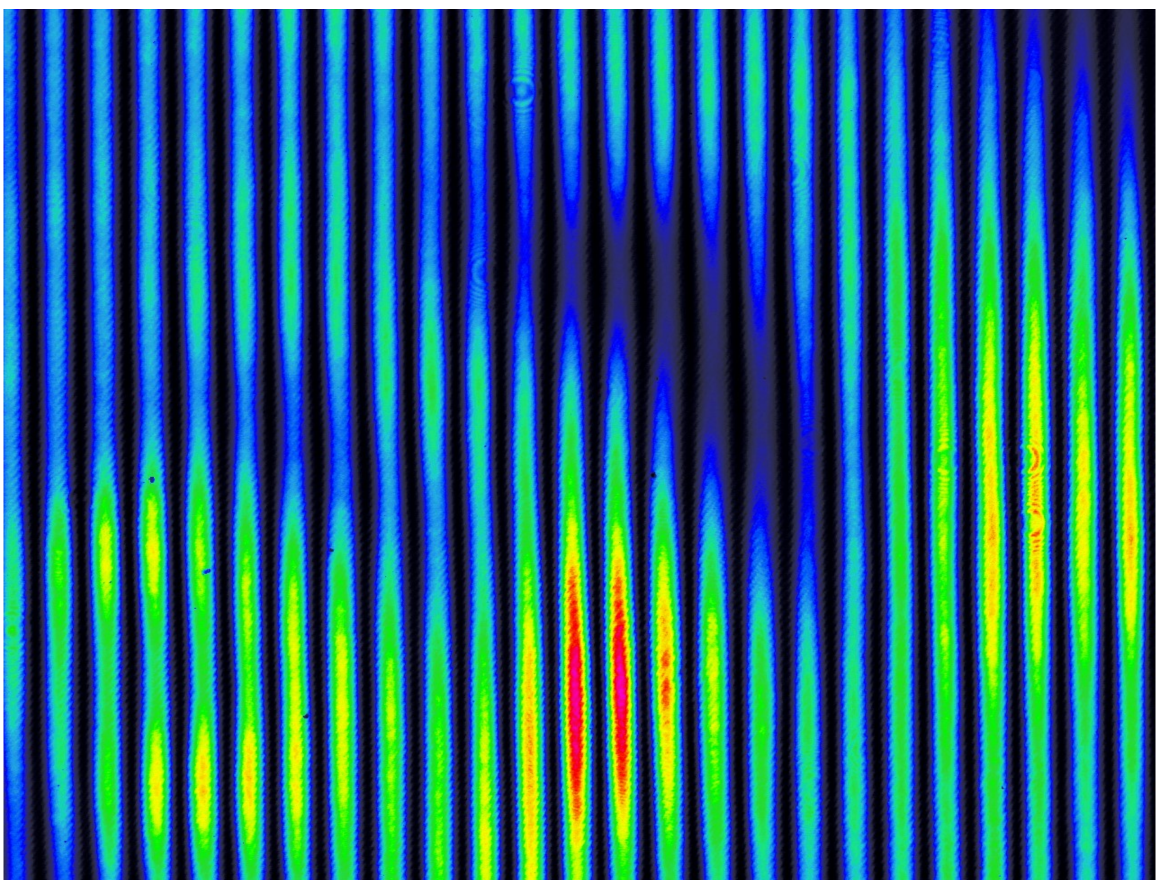

Figure 4.47: Interference fringes of the Mach-Zender interferometer in air.

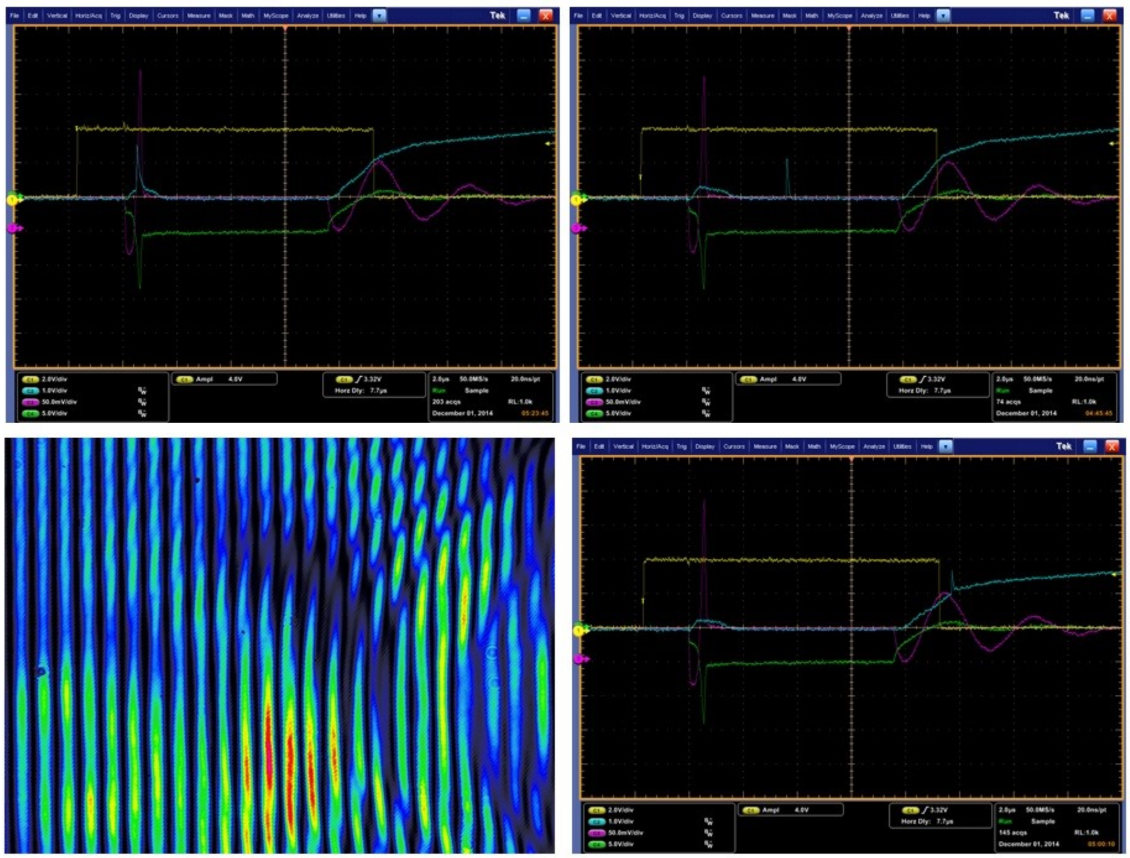

Figure 4.48: Signals recorded by a photodiode (blue trace) for various values of delay between laser beam and capacitive discharge, together with the change in fringes pattern caused by the plasma jet.

4.6 Spectrum Data

Spectrographic data was taken using a visible spectrum astronomy spectrometer. Aluminum has been shown to emit much less light than higher Z materials especially during the initial explosion [37]. While attempts were made at getting spectrum data from the early heating stages, the light was not intense enough for the spectrometer to capture a spectrum. This early stage spectrum is useful in approximating the temperature of the wire. We were able to obtain a spectrum after the restrike. At 7 kV many of the strong emission lines of aluminum were seen (see figure 4.49). The strong lines that can be observed from the Al discharge are at 281.6 nm (Al_{II}), 308.2 nm (Al_I), 309.27 nm (Al_I), 358.6 nm (Al_{II}), 394.4 nm (Al_I), and 396.1 nm (Al_I). The large peak around 589 nm is assumed to be sodium which has two high intensity emission lines at 588.9 nm and 589.5 nm, and the emission line around 500 nm is assumed to be ozone created by the discharge with a strong emission line at 500.7 nm. Figures 4.50 and 4.51 show the spectrum of both a 76 micron and 127 micron Cu wire discharged at 7kV. The predominant Cu Peaks are seen at 515.82 nm, and 521.82 nm. The Cu emission at 406.26 nm is much dimmer in the 76 micron wire than the 127 micron wire. The sodium peak around 589 nm can be seen in the Cu explosions as well, but is relatively dimmer than in the Al explosions.

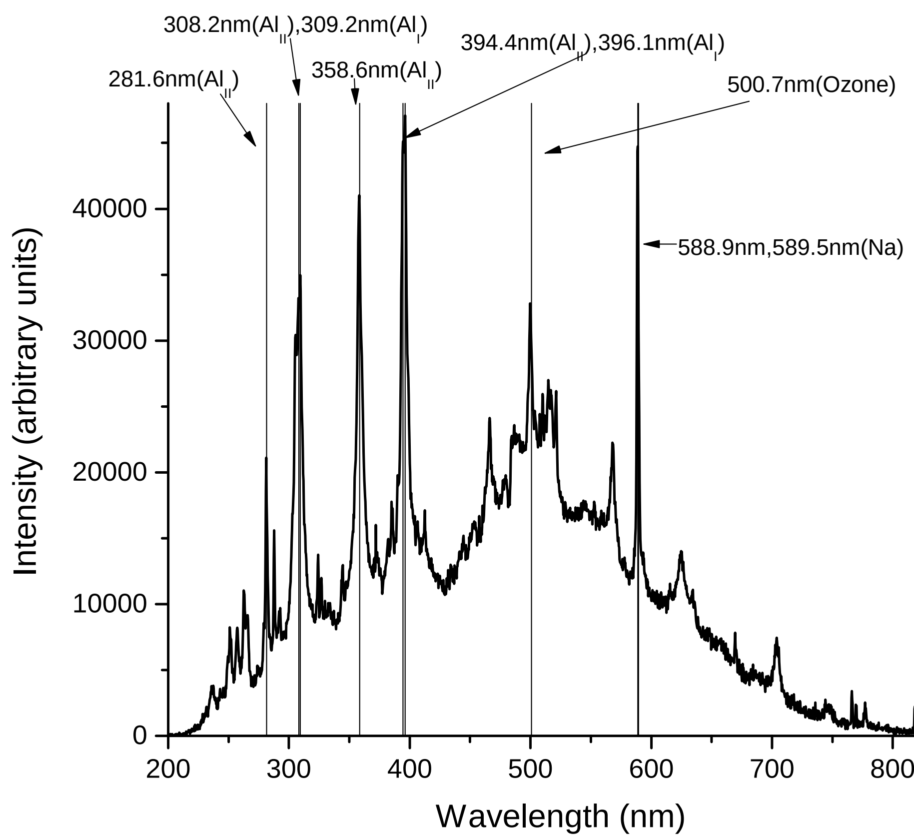

Figure 4.49: Spectral emissions from an Al wire discharge at 7 kV

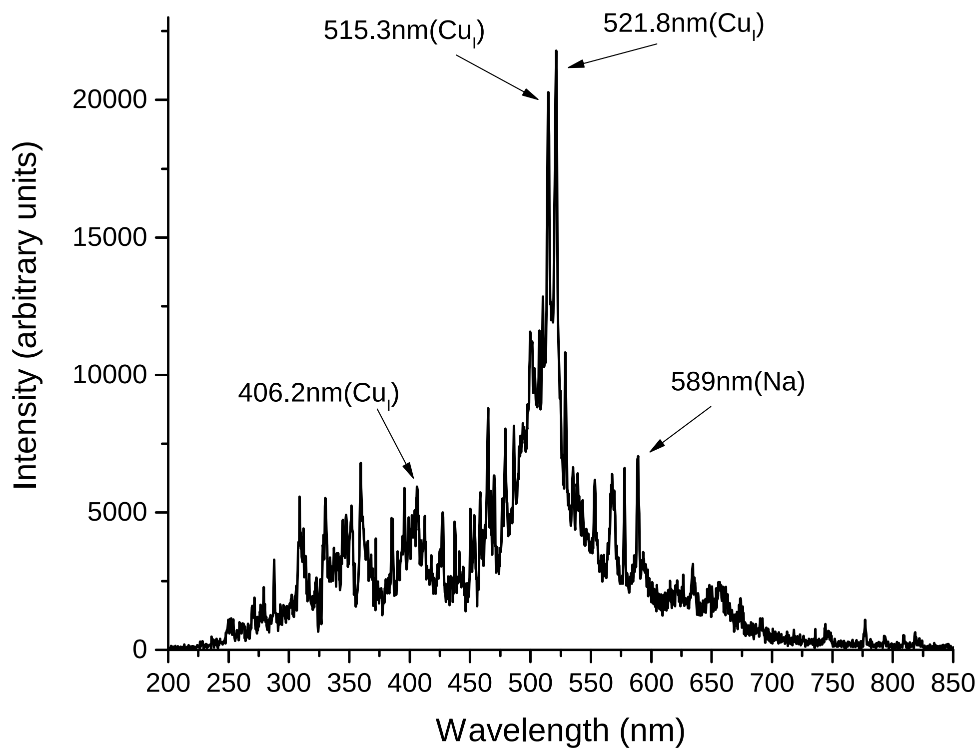

Figure 4.50: Spectral emissions from a 76 micron Cu wire discharge at 7 kV

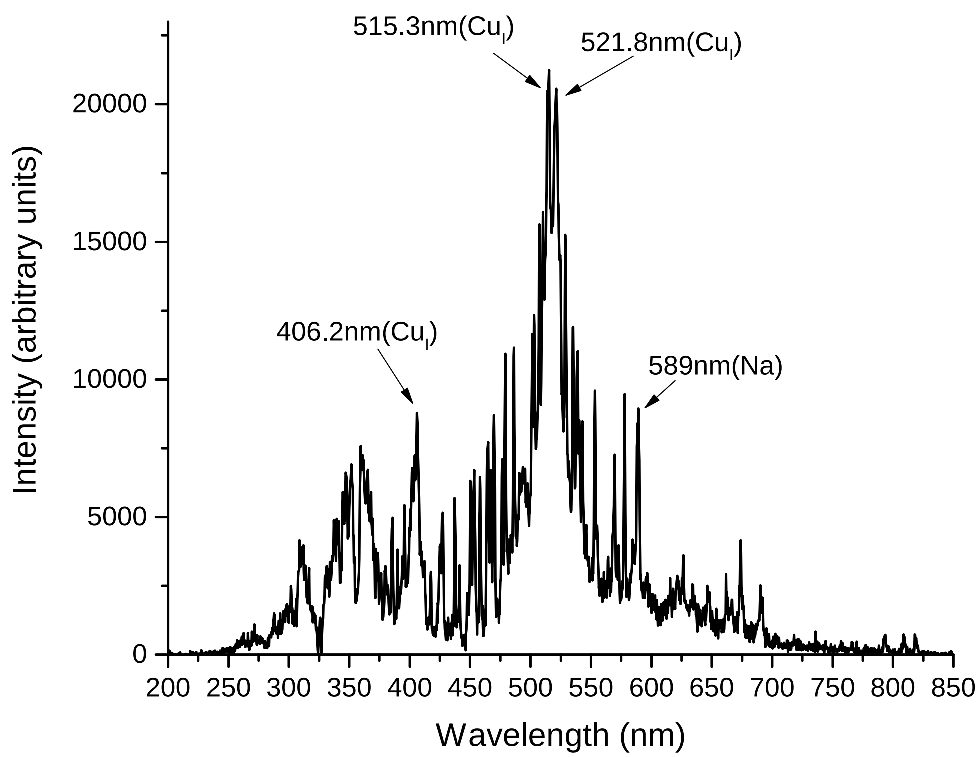

Figure 4.51: Spectral emissions from a 127 micron Cu wire discharge at 7 kV

4.7 Additional Comments and Difficulties

The largest difficulties with this project were the lack of equipment, manpower, and time to complete a thorough investigation. Previously a camera had been loaned to us from L-3 Instruments which was used to conduct earlier experiments on copper wires. This camera however had to be returned before the aluminum wire experiments were conducted. The camera used was borrowed camera from Princeton Instruments as a two week demo to test it in our experiments. The expense of such a camera made it impossible to purchase with current grant funding. Because of this all experiments had to be conducted in a short amount of time. Additionally, our work had to be conducted at night in order to have a dark room for imagining as we worked in a shared facility.

The radius data obtained does give an idea for the general trend of the expansion, but the reader should note that in order to make a more concrete conclusion much more data is needed. Exact reproducibilty is impossible between discharges due to differences in the wires, and jitter/noise from the electronics.

Additionally, we did not have access to any MHD codes which are extremely useful in confirming experimental data, and have been shown to be fairly accurate [28] [39]. Without a code in conjunction with current and voltage data it is difficult to make calculations on phase changes and plasma temperatures.

4.8 Future Work

4.8.1 Imaging

The limitation of an ICCD is the decay time of the phosphor. This forces a wait time between exposures of about 500 ns using the best phosphors available in the industry. The advantage of using ICCDs is in the short achievable gate times of up to 500 ps, and their high sensitivity. While streak cameras can provide time resolution of the exploding wire, they are limited in their one dimensional spatial resolution. Using a series of synchronized gated ICCDs and beam splitters one can achieve a higher time resolution by either taking spaced bursts 500 ns apart, or equally spaced images over the entire explosion. Although intensity is lost in the beam splitters, it can easily be recovered by increasing the gain across the intensifier. This would allow for a more in depth study of the mechanisms across the wire as a whole.

4.8.2 Laser Inteferometry

Laser interferometry has been used as a technique to measure electron densities in plasma for decades [40]. Interferometry uses the detection of a phase shift from a laser source in order to find the electron density. While our technique used to trigger the wire explosion and external equipment proved to be plausible, we were not able to use a laser source with a short enough pulse to take high resolution exposures of the interferometer as discussed in section 4.5. The solution to this would be either to use a better laser setup with less jitter between the camera and laser triggers (the laser we attempted to use had a jitter of up to 1 μs), or to use a longer exposure camera with a short pulsed laser. The short laser pulse is ideal due to the ability to compensate for any electronic jitter that may occur between the trigger and the laser. The 200 ps laser mentioned in section 4.5 will most likely be used to conduct future experiments.

4.8.3 X-Ray Imaging

X-ray sources are useful in exploding wire research because of their ability to back-light the plasma giving an idea as to the density of the matter being imaged [41]. While x-ray diffraction can be used to study the structure of strongly coupled plasmas [42], warm dense matter does not fall under the regime of strongly coupled plasma making x-ray diffraction useless in these experiments.

X-pinches are the source used in most exploding wire studies due to their short pules time (allowing for better time resolution) [41] [43]. We would like to have the capability of using an x-pinch being developed here at Idaho State University [11] as an x-ray image source for continued studies of exploding wires.

While the x-pinch provides a short burst unique x-ray source, another potential x-ray source could come from Laser Compton Scattering (LCS) such as the source being worked on by Dr. Chouffani [44]. The advantage of an LCS x-ray source would be the ability to take many images of the same explosion as the x-ray pulse frequency is only limited by the accelerator and laser used, as opposed to an x-pinch which only allows one image per explosion.

Bibliography

[1] Edward Nairne. Electrical experiments by mr. edward nairne, of london, mathematical instrument-maker, made with a machine of his own workmanship, a description of which is prefixed. *Philosophical Transactions (1683-1775)*, 64:79–89, 1774.

[2] Herbert W. Meyer. *A History of Electricity and Magnetism*. MIT Press, Cambridge, Mass, 1971.

[3] Michael A. Liberman, John S. De Groot, Arthur Toor, and Rick B. Spielman. *Physics of High-Density Z-Pinch Plasmas*. Springer, New York, New York, 1999.

[4] Michael Faraday. The bakerian lecture: Experimental relations of gold (and other metals) to light. *Philosophical Transactions of the Royal Society of London*, 147:145–181, 1857.

[5] Gerald L. Wendt and Clarence E. Irion. Experimental attempts to decompose tungsten at high temperatures. *Journal of the American Chemical Society*, 44(9):1887–1894, 1922.

[6] Henry Vincent Aird Briscoe, Percy Lucock Robinson, and George Edward Stephenson. Xli.-the electrical explosion of tungsten wires. *J. Chem. Soc., Trans.*, 127:240–247, 1925.

[7] Werner Kleen. ber den durchgang der elektrizitt durch metallische haardrhte. *Annalen der Physik*, 403(5):579–605, 1931.

[8] F.D. Bennett. Exploding wires. *Scientific American*, 1962.

[9] J.R. MCGrath and NAVAL RESEARCH LAB WASHINGTON D C. *EXPLODING WIRE RESEARCH 1774-1963*. Defense Technical Information Center, 1966.

[10] R.J. Leeper, T.E. Alberts, J.R. Asay, P.M. Baca, K.L. Baker, S.P. Breeze, G.A. Chandler, D.L. Cook, G.W. Cooper, C. Deeney, M.S. Derzon, M.R. Douglas, D.L. Fehl, T. Gilliland, D.E. Hebron, M.J. Hurst, D.O. Jobe, J.W. Kellogg, J.S. Lash, S.E. Lazier, M.K. Matzen, D.H. McDaniel, J.S. McGurn, T.A. Mehlhorn, A.R. Moats, R.C. Mock, D.J. Muron, T.J. Nash, R.E. Olson, J.L. Porter, J.P. Quintenz, P.V. Reyes, L.E. Ruggles, C.L. Ruiz, T.W.L. Sanford, F.A. Schmidlapp, J.F. Seamen, R.B. Spielman, M.A. Stark, K.W. Struve, W.A. Stygar, D.R. Tibbetts-Russell, J.A. Torres, M. Vargas, T.C. Wagoner, C. Wakefield, J.H. Hammer, D.D. Ryutov, M. Tabak, S.C. Wilks, R.L. Bowers, K.D. McLenithan, and D.L. Peterson. Z pinch driven inertial confinement fusion target physics research at sandia national laboratories. *Nuclear Fusion*, 39(9Y):1283, 1999.

[11] R.V. Shapovalov and R.B. Spielman. Short-circuit test data of a new 2-ltd-brick x-pinch driver at the idaho accelerator center. In *Pulsed Power Conference (PPC), 2015 IEEE*, pages 1–3, May 2015.

[12] S. A. Pikuz, T. A. Shelkovenko, D. B. Sinars, J. B. Greenly, Y. S. Dimant, and D. A. Hammer. Multiphase foamlike structure of exploding wire cores. *Phys. Rev. Lett.*, 83:4313–4316, Nov 1999.

[13] Zhiguo Mao, Xiaobing Zou, Xinxin Wang, and Weihua Jiang. Evolution of the electrically exploding wire observed with a machzehnder interferometer. *Applied Physics Letters*, 94(18), 2009.

[14] B. Militzer, W. B. Hubbard, J. Vorberger, I. Tamblyn, and S. A. Bonev. A massive core in jupiter predicted from first-principles simulations. *The Astrophysical Journal Letters*, 688(1):L45, 2008.

[15] Adam Burrows and James Liebert. The science of brown dwarfs. *Rev. Mod. Phys.*, 65:301–336, Apr 1993.

[16] S. H. Glenzer, O. L. Landen, P. Neumayer, R. W. Lee, K. Widmann, S. W. Pollaine, R. J. Wallace, G. Gregori, A. Höll, T. Bornath, R. Thiele, V. Schwarz, W.-D. Kraeft, and R. Redmer. Observations of plasmons in warm dense matter. *Phys. Rev. Lett.*, 98:065002, Feb 2007.

[17] M Koenig, A Benuzzi-Mounaix, A Ravasio, T Vinci, N Ozaki, S Lepape, D Batani, G Huser, T Hall, D Hicks, A MacKinnon, P Patel, H S Park, T Boehly, M Borghesi, S Kar, and L Romagnani. Progress in the study of warm dense matter. *Plasma Physics and Controlled Fusion*, 47(12B):B441, 2005.

[18] O. L. Landen, T. R. Boehly, D. K. Bradley, D. G. Braun, D. A. Callahan, P. M. Celliers, G. W. Collins, E. L. Dewald, L. Divol, S. H. Glenzer, A. Hamza, D. G. Hicks, N. Hoffman, N. Izumi, O. S. Jones, R. K. Kirkwood, G. A. Kyrala, P. Michel, J. Milovich, D. H. Munro, A. Nikroo, R. E. Olson, H. F. Robey, B. K. Spears, C. A. Thomas, S. V. Weber, D. C. Wilson, M. M. Marinak, L. J. Suter, B. A. Hammel, D. D. Meyerhofer, J. Atherton, J. Edwards, S. W. Haan, J. D. Lindl, B. J. MacGowan, and E. I. Moses. Capsule performance optimization in the national ignition campaigna). *Physics of Plasmas*, 17(5), 2010.

[19] Baifei Shen, Xiaomei Zhang, and M. Y. Yu. Laser-confined fusion. *Phys. Rev. E*, 71:015401, Jan 2005.

[20] R. Aymar, V.A. Chuyanov, M. Huguet, Y. Shimomura, ITER Joint Central Team, and ITER Home Teams. Overview of iter-feat - the future international burning plasma experiment. *Nuclear Fusion*, 41(10):1301, 2001.

[21] James H. Hammer, Max Tabak, Scott C. Wilks, John D. Lindl, David S. Bailey, Peter W. Rambo, Arthur Toor, George B. Zimmerman, and John L. Porter. High yield inertial confinement fusion target design for a z-pinch-driven hohlraum. *Physics of Plasmas*, 6(5):2129–2136, 1999.

[22] Alqudami Abdullah and S. Annapoorni. Fluorescent silver nanoparticles via exploding wire technique. *Pramana*, 65(5):815–819, 2005.

[23] Rashmita Das, Basantakumar Das, Rohit Shukla, T Prabaharan, and Anurag Shyam. Analysis of electrical explosion of wire systems for the production of nanopowder. *Sadhana*, 37(5):629–635, 2012.

[24] P. Sen, Joyee Ghosh, Alqudami Abdullah, Prashant Kumar, and Vandana. Preparation of cu, ag, fe and al nanoparticles by the exploding wire technique. *Journal of Chemical Sciences*, 115(5-6):499–508, 2003.

[25] Ron Varesh. Electric detonators: Ebw and efi. *Propellants, Explosives, Pyrotechnics*, 21(3):150–154, 1996.

[26] Antonios E. Vlasts. Thermodynamics of the first phase of exploded conductors. *Journal of Applied Physics*, 44(8):3593–3600, 1973.

[27] Antonios E. Vlasts. Current pause in explodingwire discharges. *Journal of Applied Physics*, 38(13):4993–4998, 1967.

[28] J. F. Benage, W. R. Shanahan, and M. S. Murillo. Electrical resistivity measurements of hot dense aluminum. *Phys. Rev. Lett.*, 83:2953–2956, Oct 1999.

[29] Toru Sasaki, Yuuri Yano, Mitsuo Nakajima, Tohru Kawamura, and Kazuhiko Horioka. Warm-dense-matter studies using pulse-power discharges in water. *Nuclear Instruments and Methods in Physics Research Section A: Accelerators, Spectrometers, Detectors and Associated Equipment*, 577(12):313 – 316, 2007. Proceedings of the 16th International Symposium on Heavy Ion Inertial FusionHIF 06.

[30] A. E. Vlastós. Restrike Mechanisms of Exploding Wire Discharges. *Journal of Applied Physics*, 39:3081–3087, June 1968.

[31] D. Tosic B. Perovic, editor. *Proceedings of the 7th International Conference on Ionization Phenomena in Gases*, Belgrade, Ygoslavia, 1966. Gradevinska Knjiga Pub. House, Beograd.

[32] Antonios E. Vlasts. Instabilities of electrically exploded wires. *Journal of Applied Physics*, 44(4):1616–1621, 1973.

[33] Andor Learning. Intensified ccd cameras, 2016. http://www.andor.com/learning-academy/intensified-ccd-cameras-the-technology-behind-iccds. License found at http://creativecommons.org/licenses/by-nc-nd/3.0/.

[34] Paul Hoess and Karlheinz Fleder. Response of very-fast-decay phosphors in image intensifier tubes for ccd readout devices. In Kazuyoshi Takayama, Tsutomo Saito, Harald Kleine, and Eugene V. Timofeev, editors, *24th International Congress on High-Speed Photography and Photonics*, volume 4183, pages 127–132, 2001.

[35] Alan W. DeSilva and H.-J. Kunze. Experimental study of the electrical conductivity of strongly coupled copper plasmas. *Phys. Rev. E*, 49:4448–4454, May 1994.

[36] Steven W. Smith. *The Scientist and Engineer's Guide to Digital Signal Processing*. California Technical Publishing, second edition edition, 1999.

[37] G. S. Sarkisov, P. V. Sasorov, K. W. Struve, and D. H. McDaniel. State of the metal core in nanosecond exploding wires and related phenomena. *Journal of Applied Physics*, 96(3):1674–1686, 2004.

[38] M. J. Taylor. Measurement of the properties of plasma from ETC capillary plasma generators. *IEEE Transactions on Magnetics*, 37:194–198, January 2001.

[39] T. Sasaki, M. Nakajima, T. Kawamura, and K. Horioka. Semi-Empirical Approach to Pulsed Wire Discharges in Water as a Method for Warm Dense Matter Studies. *Journal of Plasma and Fusion Research*, 81:965–966, 2005.

[40] D. E. T. F. Ashby and D. F. Jephcott. Measurement of plasma density using a gas laser as an infrared interferometer. *Applied Physics Letters*, 3(1):13–16, 1963.

[41] T. A. Shelkovenko, S. A. Pikuz, A. R. Mingaleev, and D. A. Hammer. Studies of plasma formation from exploding wires and multiwire arrays using x-ray backlighting. *Review of Scientific Instruments*, 70(1):667–670, 1999.

[42] D. Riley, N. C. Woolsey, D. McSherry, A. Djaoui I. Weaver, and E. Nardi. X-ray diffraction from a dense plasma. *Physical Review Letters*, 84(8):1704–1707, February 2000.

[43] S.A. Pikuz, T.A. Shelkovenko, P.F. Knapp, C.L. Hoyt, A.D. Cahill, and D.A. Hammer. X-ray absorption spectroscopy of exploding al wire plasmas using x-pinch radiation sources. In *Plasma Science (ICOPS), 2012 Abstracts IEEE International Conference on*, pages 2P–82–2P–82, July 2012.

[44] K. Chouffani and D. Wells and F. Harmon and G. Lancaster and J. Jones. Laser-compton scattering as a potential bright x-ray source. In *Advances in X-ray Analysis*, volume 46, pages 74–79. International Centre for Diffraction Data, 2003.